

Novel use of diamond in eye-safe lasers

PhD Thesis

Lukasz Dziechciarzyk

Institute of Photonics

Physics

University of Strathclyde, Glasgow

August 13, 2020

This thesis is the result of the author's original research. It has been composed by the author and has not been previously submitted for examination which has led to the award of a degree.

The copyright of this thesis belongs to the author under the terms of the United Kingdom Copyright Acts as qualified by University of Strathclyde Regulation 3.50. Due acknowledgement must always be made of the use of any material contained in, or derived from, this thesis.

Abstract

The phenomenon of stimulated Raman scattering is one of the ways of accessing a laser emission spectrum. This thesis focuses on converting a $1\mu m$ laser to the so called eye-safe $1.5\mu m$ wavelength useful in e.g. LIDAR applications. The novelty of this approach is that compared to ion based lasers e.g. Er:fiber, Raman lasers are mostly limited by the pump power, not by the thermal roll off, especially when using materials such as diamond with extremely high thermal conductivity. This is subjected to the absorption in the Raman crystal and other effects described more in detail in the introduction.

The work presents firstly a design of a proof of concept, low power and repetition rate pump source at $1\mu m$ based on Nd:YAG and a an external cavity Raman diamond laser. This laser was investigated to find the optimum operating conditions such as pump intensity, output coupling transmission and a laser cavity mode size.

These findings were then applied in high average power Diamond Raman laser. These experiments used an Yb based fiber master oscillator, power amplifier which acted as a pump source. These experiments concluded with obtaining over $10W$ of average power at $150kHz$ of laser emission above $1.5\mu m$ wavelength. This method of generating eye-safe wavelengths is a promising way to high power and repetition rate emission.

A novel approach of generating high average power especially with a narrow linewidth emission is also presented by using a Raman cavity in an amplifier configuration. A first diamond based, second Stokes Raman amplifier operating at eye-safe wavelengths regime is presented in Chapter 5.

Acknowledgements

I would like to thank Prof. Alan Kemp and Dr Vasili Savitski for their patience, care, support and absolute commitment in guiding me through this PhD. I will be forever grateful and indebted to you. I could not have asked for better people to work with.

Secondly I would like to thank Eli for making me do this and to all the incredible CDT DST friends who made this PhD experience unforgettable and rewarding. Great thanks to the entire IoP staff, especially Sharon and Lorraine for sending me places and putting up with me. I would also like to acknowledge amazing help I received from collaborators at the ORC at the Southampton University. Thanks to my friends for the climbing, hiking, excellent birthday parties and overall reasonably good times. To my family and Rachel for their well needed support and encouragement. Additional acknowledgments to everyone that added their piece to this puzzle and helped me prepare for the next adventure.

Contents

| | |
|---|-------------|
| Abstract | ii |
| Acknowledgements | iii |
| List of Figures | viii |
| List of Tables | xii |
| Publications | xiv |
| 1 Introduction | 2 |
| 1.1 Motivation | 2 |
| 1.2 LIDAR systems | 3 |
| 1.2.1 Beam quality | 6 |
| 1.2.2 Wavelength considerations | 7 |
| 1.2.3 High power considerations | 8 |
| 1.2.4 LIDAR laser source | 10 |
| 1.3 Diamond in Raman lasers | 10 |
| 1.3.1 Raman scattering | 10 |
| 1.3.2 Linewidth and wavelength | 13 |
| 1.3.3 Polarization considerations | 15 |
| 1.4 Eye-safe laser sources overview | 17 |
| 1.4.1 Eye-safe wavelength lasers | 17 |
| 1.4.2 Eye-safe optical parametric oscillators | 19 |
| 1.4.3 High power Raman laser pump sources at $1\mu m$ | 20 |

Contents

| | | |
|----------|---|-----------|
| 1.4.4 | Raman lasers overview | 20 |
| 1.5 | Driving of the Raman process | 23 |
| 1.5.1 | Raman laser configurations | 23 |
| 1.5.2 | Diamond Raman amplifier | 24 |
| 1.5.3 | High peak power generation | 26 |
| | Q-switching | 26 |
| | Master Oscillator Power Amplifier | 28 |
| 1.6 | Summary | 29 |
| 2 | Modeling of Raman diamond lasers | 31 |
| 2.1 | Modeling of the Diamond Raman Laser performance | 31 |
| 2.2 | Model overview | 32 |
| 2.3 | ABCD matrix cavity design | 36 |
| 2.4 | Thermal lens impact on the cavity stability | 37 |
| 2.5 | Summary | 40 |
| 3 | Diamond Raman Laser prototype | 41 |
| 3.1 | Pump source at 1079 nm | 42 |
| 3.1.1 | Gain medium | 42 |
| 3.1.2 | Cavity design | 43 |
| 3.1.3 | Experimental setup | 44 |
| 3.1.4 | Spectrum and wavelength stabilization | 47 |
| 3.2 | Pump source at 1079 nm Q-switched operation | 49 |
| 3.2.1 | Performance and output coupler optimization | 52 |
| 3.2.2 | Output spectrum | 54 |
| 3.2.3 | Beam quality | 55 |
| 3.3 | Summary | 56 |
| 3.4 | Research grade diamond samples | 57 |
| 3.4.1 | Diamond samples | 57 |
| 3.4.2 | Diamond coatings | 58 |
| 3.5 | Diamond Raman Laser proof of concept | 59 |

Contents

| | | |
|----------|---|-----------|
| 3.5.1 | Beam conditioning | 59 |
| 3.5.2 | Diamond Raman laser cavity design | 60 |
| 3.5.3 | Pump spot diameter and output coupler optimization | 62 |
| 3.5.4 | Output coupler optimization - experimental results | 66 |
| 3.6 | Diamond Raman laser performance | 68 |
| 3.6.1 | Output energy | 68 |
| 3.6.2 | Output pulse analysis | 69 |
| 3.6.3 | Simulation results | 72 |
| 3.6.4 | Output spectrum of the Diamond Raman laser | 74 |
| 3.7 | Summary | 76 |
| 4 | Fiber pumped Diamond Raman Laser | 78 |
| 4.1 | High average power pump source for diamond Raman lasers | 79 |
| 4.1.1 | Output spectra of the Yb fiber MOPA | 81 |
| 4.1.2 | Pulse traces of the Yb MOPA | 83 |
| 4.1.3 | Summary of Yb MOPA measurements | 84 |
| 4.2 | Beam conditioning of the Yb fiber for DRL pumping | 85 |
| 4.2.1 | Beam conditioning of the polarized pumping of the DRL | 85 |
| 4.2.2 | Beam conditioning for the unpolarized pumping of the DRL | 87 |
| 4.3 | Yb fiber pumped DRL cavity and output emission analysis setup | 89 |
| 4.4 | Depleted pump spectrum analysis | 90 |
| 4.5 | Emission spectra of the DRL | 92 |
| 4.5.1 | Polarized pump emission | 92 |
| 4.5.2 | Unpolarized pump emission | 96 |
| 4.6 | DRL emission spectra summary | 97 |
| 4.7 | Multimode Yb fibre pumped DRL performance | 97 |
| 4.7.1 | Pump focusing and DRL cavity | 98 |
| 4.7.2 | Impact of cooling of the DRL diamond mount | 98 |
| 4.7.3 | Power transfer | 99 |
| 4.7.4 | Time traces analysis | 101 |
| 4.8 | Polarized Yb fibre pumped DRL performance | 103 |

Contents

| | | |
|----------|---|------------|
| 4.8.1 | Pump focusing and DRL cavity | 103 |
| 4.8.2 | Power transfer | 103 |
| 4.8.3 | Time trace analysis | 106 |
| 4.9 | Yb fiber pumped DRL summary | 107 |
| 4.9.1 | Summary table | 107 |
| 4.9.2 | Summary discussion | 108 |
| 5 | Diamond Raman amplifier | 111 |
| 5.1 | Raman amplifier principle of operation | 112 |
| 5.2 | Setup | 114 |
| 5.2.1 | Diamond Raman amplifier | 114 |
| 5.2.2 | Impact of the parasitic emission at second Stokes wavelength on the amplification factor | 116 |
| 5.2.3 | Seed laser | 117 |
| 5.2.4 | Seed laser wavelength tuning | 118 |
| 5.3 | Amplification factor measurement method | 121 |
| 5.4 | Optimization the amplification process | 123 |
| 5.4.1 | Spatial overlap | 123 |
| 5.4.2 | Spectral tuning | 124 |
| 5.5 | The effect of jitter on the amplification factor | 125 |
| 5.6 | Effect of the seed laser pulse energy on amplification | 127 |
| 5.7 | Summary | 128 |
| 5.7.1 | Jitter and pulse duration | 129 |
| 5.7.2 | Wavelength variations | 130 |
| 5.7.3 | Parasitic second Stokes emission | 130 |
| 5.7.4 | First Stokes wavelength | 130 |
| 6 | Discussion and conclusions | 132 |
| 6.1 | External cavity Raman laser model | 132 |
| 6.2 | Diamond considerations | 133 |
| 6.3 | Diamond Raman laser proof of concept | 136 |

Contents

| | | |
|-------|---|-----|
| 6.3.1 | Future work | 137 |
| 6.4 | Diamond Raman laser pumped by a high average power fiber MOPA . . | 138 |
| 6.4.1 | Future work | 139 |
| 6.5 | Diamond Raman amplifier | 139 |
| 6.5.1 | Future work | 140 |
| 6.6 | Context of the eye-safe high power DRL | 142 |

| | | |
|---------------------|--|------------|
| Bibliography | | 142 |
|---------------------|--|------------|

List of Figures

| | | |
|-----|---|----|
| 1.1 | Maximum permissible exposure versus laser wavelength | 5 |
| 1.2 | A simulation of a beam propagation with a different M^2 parameter. . . | 7 |
| 1.3 | Raman scattering in crystals. | 11 |
| 1.4 | Raman laser energy diagram | 12 |
| 1.5 | Wavelengths reached by a second order Raman conversion in different crystals when pumped by $1.08\mu m$ laser. | 14 |
| 1.6 | Configurations of the Raman lasers - intracavity and external cavity configurations and Raman amplifier with external seeding. | 23 |
| 1.7 | Population inversion and laser threshold in the Q-switch lasers. | 27 |
| 2.1 | A model of the external cavity Raman laser. | 31 |
| 2.2 | Smoothing function applied to the Stokes output pulse normalized by the pulse energy. | 36 |
| 2.3 | Laser cavity with a laser crystal with a thermal lens. | 38 |
| 2.4 | Heat and refractive index gradient distribution over an optically pumped crystal. | 38 |
| 2.5 | Stability of the diamond Raman laser cavity against a thermal lens strength in the diamond crystal. | 40 |
| 3.1 | Simulation of the output energy in a Q-switched Nd:YAP laser versus mode radius in the gain medium. | 44 |
| 3.2 | Mode size radius in the Nd:YAP laser cavity | 45 |
| 3.3 | Developed Nd:YAP laser pump source. | 45 |

List of Figures

| | | |
|------|--|----|
| 3.4 | Nd:YAP laser output linewidth narrowing and tuning through the etalon. | 48 |
| 3.5 | Q-switching setup for Nd:YAP laser. | 50 |
| 3.6 | Evolution of the population inversion in the Nd:YAP laser. Normalization to the maximum population inversion. | 52 |
| 3.7 | Nd:YAP laser output pulse analysis. | 53 |
| 3.8 | Pulse energy and duration as function of pump power. | 54 |
| 3.9 | Nd:YAP spectrum in pulsed regime. | 55 |
| 3.10 | Beam diameter fit for the beam quality measurement. | 56 |
| 3.11 | Crystallographic directions of the diamond samples. | 57 |
| 3.12 | Cross-polarization measurement of the birefringence in the diamond samples. | 58 |
| 3.13 | Simulation of the reflectivity spectrum of anti-reflection coatings on diamond. Courtesy of Lambda Research Optics, Inc. | 58 |
| 3.14 | Diamond positioned in between input and output coupler makes a DRL cavity. | 59 |
| 3.15 | Conditioning optics for the DRL. | 60 |
| 3.16 | Mode size propagation along the DRL cavity axis. | 61 |
| 3.17 | Stability and mode diameter of $1516nm$ for a DRL cavity (plane input coupler and $50mm$ output coupler) versus the distance between the diamond surface and the output coupler. | 62 |
| 3.18 | Simulation of the DRL performance versus pump spot diameter and output coupler partial reflectivity at a pump energy $E = 400\mu J$ | 64 |
| 3.19 | Energy transfer of the DRL working at $1.5\mu m$ wavelength range versus output coupling. Solid lines are linear fits of the data. | 67 |
| 3.20 | A setup for measuring the pulse traces at first, second Stokes and depletion of the pump. | 68 |
| 3.21 | Energy transfers of DRL of all available diamond samples. Two simulated energy transfers showcase the accuracy of the model. | 69 |
| 3.22 | DRL output pulses at different output coupling. | 71 |
| 3.23 | DRL output pulses at different output coupling. | 73 |

List of Figures

| | | |
|------|---|----|
| 3.24 | Simulated time traces in the DRL of the depleted pump, first and second Stokes emission. | 74 |
| 3.25 | Simulation and measurements of the energy transfers and conversion efficiency of the DRL performance with the $4mm$ and $7mm$ diamonds. . . | 75 |
| 3.26 | Output emission wavelength cascade from the DRL. | 76 |
| 4.1 | MOPA system developed by the University of Southampton (Optoelectronics Research Center) which was used as a pump source for DRL. . . | 80 |
| 4.2 | Normalized to maximum values output spectra of the MOPA system in polarized and multimode configuration. | 82 |
| 4.3 | Wide scan of the MOPA output emission. | 83 |
| 4.4 | Output pulses of the MOPA system. $150kHz$ operation, $30W$ average power, Nd:YAP pulse for comparison. | 84 |
| 4.5 | Image from a CCD camera of a focused MOPA beam at different operation conditions. | 87 |
| 4.6 | Beam profiles of the MOPA in the focus of a $f = 100mm$ lens operating at $10W$, $150kHz$ | 88 |
| 4.7 | Beam profile of a multimode output of the MOPA system at $10W$, $150kHz$ | 89 |
| 4.8 | Spectrum measurement setup allowing for power, spectrum and pulse traces measurements. | 90 |
| 4.9 | Spectra of depleted and input pump. MOPA at $30kHz$ operation, $15W$ average power, polarized emission. | 91 |
| 4.10 | Spectra of depleted and input pump. MOPA at $150kHz$ operation, $70W$ average power, unpolarized emission. | 92 |
| 4.11 | Wide spectrum of the DRL output emission. | 93 |
| 4.12 | Pump spectra at different repetition rates, $0.05nm$ resolution. | 94 |
| 4.13 | DRL output emission at a wavelength of above $1.5\mu m$ | 95 |
| 4.14 | DRL emission spectrum pumped by $85W$ of unpolarized MOPA spectrum, first and second Stokes at $1264nm$ and $1521nm$ respectively. . . . | 96 |
| 4.15 | Cooling arrangement of the diamond. Diamond rests on the brass mount chilled with water. Thermocouple attached to the surface of the diamond. . . | 98 |

List of Figures

| | | |
|------|--|-----|
| 4.16 | Power transfer of the DRL pumped by a multimode Yb fibre MOPA without and with cooling. | 99 |
| 4.17 | Power transfer of the DRL pumped by a multimode Yb fibre MOPA with cooling. | 101 |
| 4.18 | Time traces of the output of the unpolarized multimode Yb fiber MOPA pumped DRL. | 102 |
| 4.19 | Yb fibre pumped DRL power performance at different repetition rates. . | 104 |
| 4.20 | Yb fibre pumped DRL energy performance at different repetition rates. | 105 |
| 4.21 | Time traces of a MOPA pumped DRL at different operating conditions. | 106 |
| 5.1 | Amplification process of a $1.5\mu m$ seed laser in a diamond Raman amplifier. | 112 |
| 5.2 | Schematic for the diamond MOPA system. | 115 |
| 5.3 | Output spectrum of the DRA seed at different ELD operating conditions. | 119 |
| 5.4 | Output spectrum of the EDFA when seeding with two different seed wavelengths. EDFA pumps at the maximum available current. | 120 |
| 5.5 | Averaged seed laser pulses (ELD at $110mA$ and $47^{\circ}C$) with Nd:YAP on and off. | 122 |
| 5.6 | Average amplification factor of the diamond amplifier depending on the seed laser wavelength. | 124 |
| 5.7 | Amplification of the seed laser pulses with varying Nd:YAP pulse position. | 126 |
| 5.8 | Gain estimation from an area of non amplified versus amplified seed laser pulses. | 129 |
| 6.1 | Simulation of the DRL performance versus the diamond's length L | 134 |
| 6.2 | Simulation of the slope efficiency and maximum conversion efficiency of the DRL at $1.5\mu m$ at pumping energy of $400\mu J$ versus absorption coefficient. | 135 |
| 6.3 | Scheme of the diamond Raman amplifier with a waveplate (WP) and a polarization beam splitter (PBS) outcoupling $1.5\mu m$ second Stokes noise out of the amplifier cavity. | 141 |

List of Tables

| | | |
|-----|--|-----|
| 1.1 | Overview of the laser sources used for LIDAR systems. | 3 |
| 3.1 | Optimization of the output coupler in Nd:YAP laser | 53 |
| 3.2 | Parameter of the developed Nd:YAP laser. | 56 |
| 3.3 | Parameters for the model used for pump spot optimization. d_i are diameters of i order Stokes laser modes ($i = 0$ for pump wavelength), plane input coupler. | 63 |
| 3.4 | Comparison of the performance of the DRL laser versus reflectivity of the output coupler. | 67 |
| 3.5 | Summary of the diamond samples performance in the DRL. | 69 |
| 4.1 | Summary of all the important parameters achieved in the Yb MOPA pumped DRL experiments. (1) This number represents the FWHM value of the highest peak in the emission spectrum in the Figure 4.13. | 108 |
| 5.1 | Intracavity pulse energy for first and second Stokes depending on the coatings partial reflectivity PR. Pump pulse peak power $P_{peak} = 20kW$ | 117 |

Publications

- Dziechciarczyk, Łukasz and Huang, Zhimeng and Demetriou, Giorgos and Cheng, Dan and Pidishety, Shankar and Feng, Yujun and Feng, Yutong and Wang, Guozheng and Lin, Huaiqin and Zhu, Sheng and others: **9 W average power, 150 kHz repetition rate diamond Raman laser at 1519 nm, pumped by a Yb fibre amplifier.** – *The European Conference on Lasers and Electro-Optics*, 2019
- Nikkinen, Jari and Savitski, Vasili and Reilly, Sean and Dziechciarczyk, Łukasz and Härkönen, Antti and Kemp, Alan and Guina, Mircea: **Sub-100 ps monolithic diamond Raman laser emitting at 573 nm.** – *IEEE Photonics Technology Letters*, 2018

Chapter 0. Publications

Chapter 1

Introduction

1.1 Motivation

The motivation for this project is to (i) find a way to efficiently generate high power laser emission at eye-safe wavelengths ($> 1.5\mu m$) for LIDAR and range finding applications (ii) investigate the performance of the optical grade diamonds produced by Element 6 in the high power laser applications using the effect of stimulated Raman scattering. These two research goals were realized by design and development of a high power laser source working at eye-safe wavelength using diamond as a wavelength converter.

Diamond is a focus of this thesis due to its numerous advantages as well as novelty. It has a transparency ranging from $220nm$ (due to the energy bandgap of $5.5eV$ [1]) to $2.5\mu m$ where the multiple phonon absorption band starts to arise[2, 3]. This makes diamond suitable for the use as a Raman crystal in the $1.5\mu m$ wavelength region. The advantages of using diamond are described in more detail in Section 1.3.1. The diamond samples used in this thesis were high quality chemical vapour deposition (CVD) process[4–7] crystals and their specifications are described in Section 3.4.

This work presents a step towards the required laser source for the scanning LIDAR. The ultimate goals for the laser to be developed are as set out by [8]: $1.5 - 1.6\mu m$ wavelength, TEM_{00} beam quality, $1.5MHz$ repetition rate, $100\mu J$ pulse energy with $1 - 2ns$ duration, $150W$ average power.

1.2 LIDAR systems

To motivate the requirements and characteristics of the laser source, a brief overview of LIDAR applications is provided. Light Detection and Ranging (LIDAR) is used for remote sensing applications. Some of the examples of using LIDAR are described in [9–11], where LIDAR was used for optimization of the wind turbines efficiency and wind surveying as a tool for effective wind farm placement. Other applications include environmental measurements [12], ranging, obstacle analysis and 3D mapping[13, 14]. Examples of lasers commonly used for LIDAR are given in Table 1.1 adapted from [15]. It is readily visible that the average powers of these lasers in the eye-safe range (above $1.5\mu m$ [16, 17]) are in the regime of a few watts. The table shows also available LIDAR sources at other wavelengths than eye-safe, which imposes a limit of maximum permissible exposure according to the standard described in [16, 17]. If a LIDAR application requires a high power laser source, using eye-safe wavelength relaxes the power limitations which are provided for reference in Section 1.2.2. Depending on the application, a different type of LIDAR might be desired with a laser source having different characteristics and these will be described now. Then considerations on a choice of the wavelength and power will be discussed.

| Technology | Wavelength | Energy | Repetition frequency | Pulse duration | Average power |
|--------------------|----------------------|-----------------|----------------------|----------------|----------------|
| Pulsed laser diode | 905nm | $< 10\mu J$ | several kHz | 30-200 ns | $\approx 10mW$ |
| Er fiber laser | 1550nm | $< 400\mu J$ | several 10 kHz | 5-100 ns | $\approx 4W$ |
| Yb fiber laser | 1064nm | $< 200\mu J$ | several 10 kHz | 5-100 ns | $\approx 2W$ |
| DPSS Nd:YAG | 1064, 532, 355 nm | 60, 30,10 mJ | < 100 Hz | 5-10 ns | $\approx 5W$ |

Table 1.1: Overview of the laser sources used for the LIDAR systems[15].

The main types of LIDAR include scanning, Doppler and flash schemes. Scanning LIDAR uses a pulsed laser beam which is steered over a desired area by two rotating angled mirrors[15, 18]. This laser beam then scatters off particles in the air or other reflective objects. The distance to such an object can be estimated by measuring the time δt it takes for the back scattered light to arrive back at the LIDAR’s detector.

This distance d equals $d = \frac{c \times \delta t}{2}$, where c is a speed of light and a factor of 2 indicates a roundtrip of the pulse. The distance resolution is then determined by the pulse duration Δt of the laser source $\Delta d = \frac{c \times \Delta t}{2}$. E.g. for a pulse of $10ns$, the distance resolution is $1.5m$. The distance resolution depends on the pulse width [19, 20] and in the extreme case where the roundtrip time is much shorter than the laser pulse width, value of Δt can not be resolved.

In determining the distance a signal processing is used to determine the time between LIDAR output and received pulses. Research shown in [21] shows estimation of accuracy and precision in ranging of a LIDAR system using different algorithms for fitting the outgoing and return pulses. The pulse discriminators were leading edge, maximum of the peak, center of gravity, inflection and constant fraction. The group found that the precision in determining the distance was below $2cm$ for all of the methods below a distance of $20m$, but increased to about $15cm$ for the constant fraction and to about $5cm$ for all other methods at $45m$ distance (maximum of the peak was best objectively). The accuracy was the worst for the leading edge discriminator increasing from $0.4m$ at $10m$ distance to $1.5m$ accuracy at $45m$ distance. Other discriminators were found to be equal in accuracy.

Doppler LIDAR additionally to the position, uses a frequency shift that the laser light experiences when back scattered off of moving objects (Doppler shift)[22]. This shift depends on the speed of the object and sources that use this technique have specific requirements on their linewidth since the speed resolution depends on how narrow the linewidth of the laser is. Therefore, the speed of an object is $v = \frac{\Delta f \lambda}{2}$ [23], where Δf is the Doppler frequency shift of the returning laser light and λ is its center wavelength.

Flash LIDAR uses a single high energy pulse illumination (which can consist be multiple beams[24]) over an area of interest and detects the scattered light using an array of detectors[25]. The detected signal is time gated to give a depth resolution.

The previously mentioned application of a LIDAR for wind surveying shows a common feature of working environment for these systems which is in the open space where the laser light has a chance to scan over a person's eyes. Figure 1.1 shows a graph adapted from American National Standard for safety of lasers [17], where the maxi-

Maximum permissible exposure at $1.5\mu\text{m}$ emission is five orders of magnitude higher than for the sources at $1\mu\text{m}$ mentioned in Table 1.1. This makes the eye-safe wavelength a choice for LIDAR laser source since the higher the average power and pulse energy, the better the signal-to-noise ratio of the given measurements [18, 26] and high repetition rate (which increases the average power) increases the LIDAR scanning rate[19, 20].

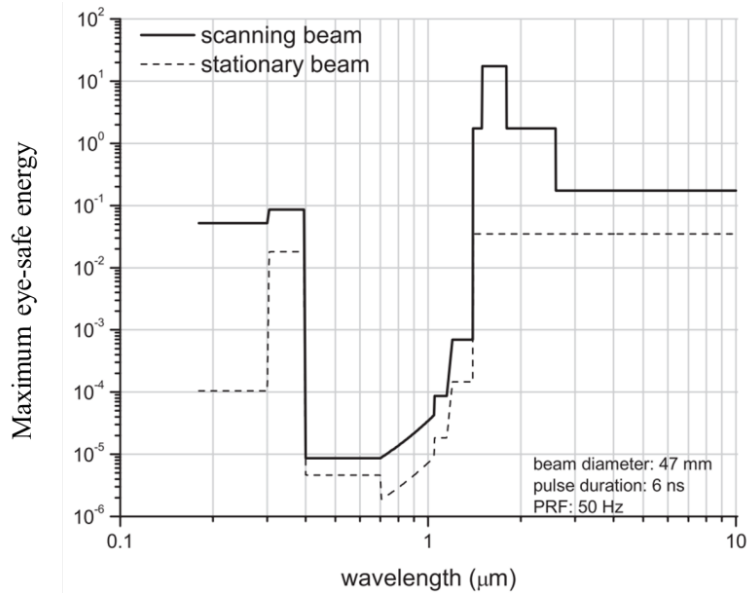


Figure 1.1: Maximum permissible exposure versus laser wavelength[17].

The requirements for the laser sources for LIDAR based on a technology overview research[8] are therefore: operating at so called eye-safe wavelength ($> 1.5\mu\text{m}$) since it allows using the order of magnitude higher powers compared to non eye-safe wavelengths [16]; high repetition rate and high average power - MHz regime and above $100W$ allowing for high signal to noise ratio and fast scanning rates with ns level pulse durations for acceptable distance resolution; very high beam quality for non diverging beam improving the signal-to-noise ratio and the maximum distance the LIDAR can operate. This beam quality is usually measured by an M^2 parameter which is described in detail in the next section.

1.2.1 Beam quality

Part of the laser characterization was measuring of the beam quality parameter M^2 which determines the ratio between the divergence of the measured beam when compared to the ideal Gaussian beam. There are two main reasons why this is important. Beam quality parameter determines how divergent the beam is and influences effective range of the LIDAR source by decreasing the amount of the scattered light from particles that are at large distances. Moreover, the back reflected power would be reduced since only a part of the beam area would be scattered. In terms of the pump for the Raman laser, its beam divergence determines the confocal parameter (twice Rayleigh range) to Raman crystal length ratio which in turn influences the Raman conversion efficiency[27].

As mentioned before, diamond Raman lasers are also considered to clean the pumping beam in terms of the quality. It can be seen in [28, 29] it is possible to pump a Diamond Raman laser (DRL) with a relatively high M^2 factor (up to $M^2 = 7$) which results in a Raman emission with an $M^2 = 1.1$.

To find the M^2 parameter of a laser Gaussian beam, we can use a fact that its radius w changes along the propagation distance z following the Equation 1.1 [30–32]

$$w(z) = w_0 \sqrt{1 + \left(\frac{M^2 \lambda z}{\pi w_0^2} \right)^2} \quad (1.1)$$

where λ is a wavelength of a beam, w_0 is a beam radius at a focus and $w(z)$ is a beam radius after propagation over a distance z and M^2 parameter is a beam quality parameter. Figure 1.2 shows a simulation of the beam diameters versus propagation distance for $M^2 = 1$ and $M^2 = 1.5$ for the same w_0 . It can be seen that the M^2 parameter affects the divergence of the beam. The range over which the beam is considered approximately collimated is called a Rayleigh range z_R and follows Equation $z_R = \frac{\pi w_0^2}{M^2 \lambda}$.

The procedure of the M^2 measurement used here follows one described in[30] and is based on ISO standard EN ISO 11 146: (i) beam diameters d ($d = 4\sigma$, four times standard deviation of the measured beam profile) are measured around the focal position (within

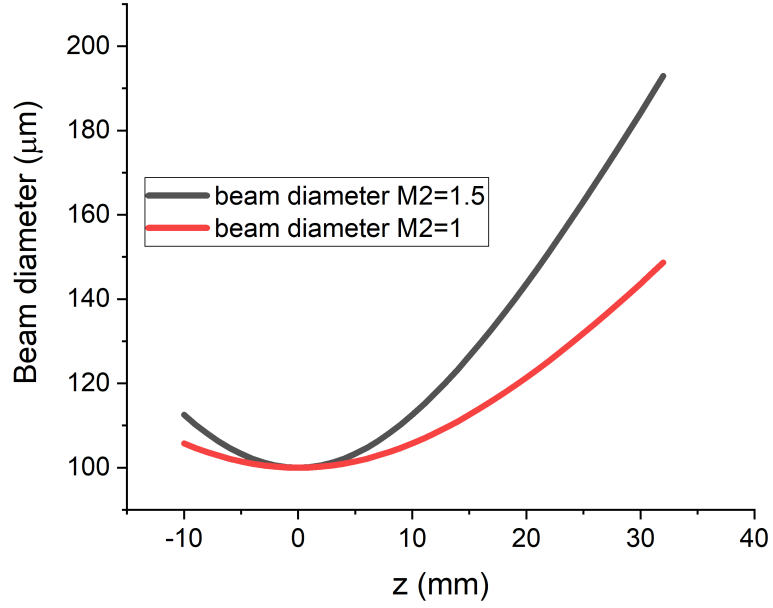


Figure 1.2: A simulation of a beam propagation with a different M^2 parameter.

a Rayleigh range) as well as in the far field (multiple Rayleigh ranges away). The measured beam diameters create a caustic which can be fitted with the Equation 1.2 [30]:

$$d(z) = \sqrt{A + B \times z + C \times z^2} \quad (1.2)$$

where A , B and C are fitting parameters. (ii) the M^2 parameter can then be calculated following Equation 1.3 [30]:

$$M^2 = \frac{\pi}{4\lambda} \sqrt{A \times C - \frac{B^2}{4}} \quad (1.3)$$

In the next section, considerations regarding a laser source emitting at an eye-safe wavelength at high powers are presented. The aim of these is to briefly introduce a motivation behind choosing a diamond as a laser material.

1.2.2 Wavelength considerations

The "eye-safe" wavelength terminology comes from the fact that that laser light at certain wavelengths is absorbed by the interocular fluid before reaching the retina of the eye where it can cause permanent damage and scarring[33]. Maximum permissible

exposure to the eye in terms of intensity is an order of magnitude higher for wavelengths between $1.5 - 1.8\mu\text{m}$ than at $1.4 - 1.5\mu\text{m}$ and $1.8 - 2.6\mu\text{m}$ [16] which establishes a window of operation for the high power sources operating in the open field. It must be mentioned that the standard [16] specifies exposure time as well as intensity and as noted in [34], eye-safe lasers should correctly be called retina-safe lasers and even at "eye-safe" wavelengths, long exposure or high enough energy could cause damage.

Reaching eye-safe wavelength is possible with various technologies e.g. Yb:Er [35] and Er doped [36] fibres, optical parametric oscillators (OPOs) [37] and through nonlinear wavelength conversion such as Raman conversion [38]. The laser sources in first two require an optical medium with a gain at $1.5\mu\text{m}$ wavelength (through the population inversion) while the nonlinear conversion uses $\chi^{(2)}$ and $\chi^{(3)}$ nonlinear optical susceptibilities allowing to convert pump laser light into another wavelength[39]. The focus of this thesis is using diamond, which does not have a population inversion, but has a $\chi^{(3)}$ nonlinearity and the wavelength conversion process through the Raman scattering process will be covered in more detail in Section 1.3.1.

1.2.3 High power considerations

High power LIDAR requirement (e.g. through high repetition rate) also has its implications on the choice of the laser source design. The quantum defect[40] - difference between the pump and laser emission wavelengths - causes heat deposition in the laser gain medium. For example, a quantum defect in a typical laser system - diode pumped Nd:YAG - has at least 25% of the pump power transferred into heat[41]. This amount of heat at high powers can introduce many sources of degradation of the laser performance or even damage. Non-uniform heating of the material can cause a so called thermal lens which is usually a contribution of material bulging through non-uniform expansion and a change of refractive index with temperature $\frac{dn}{dT}$ [42, 43]. Therefore a material of a high heat conductivity is desired for the high power applications, allowing for efficient heat extraction out of the laser gain medium.

Now briefly the $\frac{dn}{dT}$ effect is described. The pump of a solid state laser has usually a spatial Gaussian profile and as such, the dn is larger in the center of the beam due

to its intensity distribution. This non uniform refractive index distribution over the transverse profile of the laser mode can lead to creating an unwanted thermal lens[44] in the laser cavity. The thermal lens can change the laser mode sizes and make the laser behave in an undesirable way. The thermal lens strength is inversely proportional to the thermal conductivity of the material[45–48] making an argument for the high conductivity tied to the laser performance. In [47], thermal conductivity of multiple undoped laser crystals is compared; a YAG crystal being the highest $T_c = 11Wm^{-1}K^{-1}$ and phosphate glass closing the list with $T_c = 0.8Wm^{-1}K^{-1}$. A single crystal high purity diamond’s thermal conductivity was measured to be $T_c = 2400Wm^{-1}K^{-1}$ [2, 49] which is two orders of magnitude higher than in a YAG crystal. This fact makes diamond unrivaled in terms of thermal lens handling but also thermal management in high power laser applications. A case study of the impact of the thermal lensing on the cavity stability is presented in Section 2.4.

In the standard laser geometry and laser crystals, a thermal lens is mostly prominent in solid state lasers, Raman lasers and OPOs and therefore making it difficult to reach high average powers. A solution to this commonly is to use optical fibers as a gain medium in which the thermal lensing is negligible because of the waveguiding effect [50]. The damage in fiber lasers is not then caused by thermal effects, but other mechanisms. When producing high peak powers, because of long interaction lengths of the pump light with the fiber and small core areas, effects such as stimulated Brillouin scattering, self-phase modulation etc. can cause e.g. substantial amount of back-scattered light [51], spectral broadening, four-wave mixing [52], unwanted pump energy transfer to the Brillouin scattered fields, nonlinear polarization rotation [53], self-focusing [54]. In general the choice of technology for high power laser source at the eye-safe wavelength is a mixture of available pump power achieved at a certain wavelength e.g. in the Raman laser output wavelength depends on the pump wavelength, pulse duration, repetition rate, beam quality as well as available expertise.

1.2.4 LIDAR laser source

To summarize the two previous sections, the ideal material for the LIDAR laser source would then be a technology allowing generation of wavelength at above $1.5\mu m$ at high average powers and repetition rates. The material should have therefore a very high thermal conductivity to withstand high thermal load.

Diamond is a very promising laser material due to its thermal conductivity, but it can not be doped to create a gain at $1.5\mu m$ through the population inversion mechanism. Unfortunately the reasons for the diamond having high transparency over a large range of wavelengths and high heat conductivity (crystal structure and strong bonds between carbon atoms) make it unsuitable for doping like in other standard inversion based laser crystals. Doping diamond with common elements like Nd or Yb is not currently possible due to the density of the diamond's lattice structure[55, 56]. Dopants useful in conventional solid state lasers deform the diamond's lattice, compromising its advantages[57]. On the other hand, as mentioned, another method is to use diamond $\chi^{(3)}$ nonlinearity for wavelength Raman conversion and Section 1.3 will explain how this nonlinearity can be used in a context of a Raman laser.

1.3 Diamond in Raman lasers

This section starts with the explanation of the Raman scattering process and how it can be used for eye-safe wavelength generation in a Raman laser. This is followed by the requirements for the various characteristics of the Raman laser pump source. At the end a role of fiber lasers is shown in a context of eye-safe wavelength generation and Raman scattering based lasers.

1.3.1 Raman scattering

Raman scattering was first observed in 1928 in liquids by C.V. Raman [58] in an experiment where the light coming from the sun was focused onto a scattering liquid. Figure 1.3 shows two chosen types of scattering. Rayleigh scattering is observed when the scattered light has the same energy as the light coming into the scattering

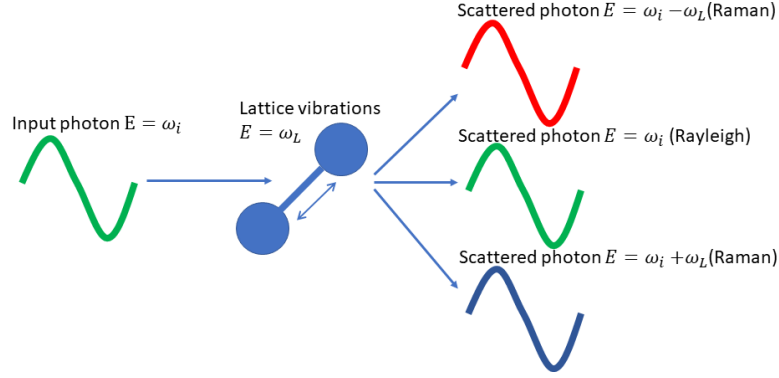


Figure 1.3: Raman scattering in crystals. Energy E of the given photon is represented as ω .

medium ($E = \hbar\omega_i$). Raman scattering occurs when incoming photon loses (or gains) the energy by interacting with the crystal lattice vibrations ω_L and results in the emission of the photon of an energy $E = \hbar(\omega_i \pm \omega_L)$ [59]. Not all materials can be used as Raman generators - these are crystals that exhibit an inversion symmetry of the lattice[39] and are said to be Raman active. The scattered photons with higher energy ($E = \hbar(\omega_i + \omega_L)$) are called anti-Stokes and the lower energy photons ($E = \hbar(\omega_i - \omega_L)$) Stokes components. After the transformation, the output Stokes shifted wavelength can be expressed with Equation 1.4 [39]:

$$\lambda_e[nm] = \frac{1}{\frac{1}{\lambda_i[nm]} - \frac{\omega_L[cm^{-1}]}{10^7}} \quad (1.4)$$

where λ_e and λ_i are Raman shifted emission wavelength and pump incident wavelength respectively.

In the context of lasers, a useful energy diagram is presented in Figure 1.4. The excitation represents here an incoming photon energy of a pump, which creates a virtual energy level. This is not an electronic level and no electronic absorption of the pump photon is present in this case. The scattered photon emission is then determined by the available phonon q energy which is characteristic to the Raman gain medium. Such emitted photons have random direction and phase and are called spontaneous Raman scattering [39, 60]. Now these photons can stimulate the process and in turn

create stimulated Raman scattering with the emitted photons of the same phase and direction. Moreover, the phonons or lattice vibrations contribute to the generation of the heat in the laser crystal. It can be then said, that in Raman lasers, the heat in a defect free, transparent medium is not generated by the absorption of the input light but by generation of phonons in the scattering process.

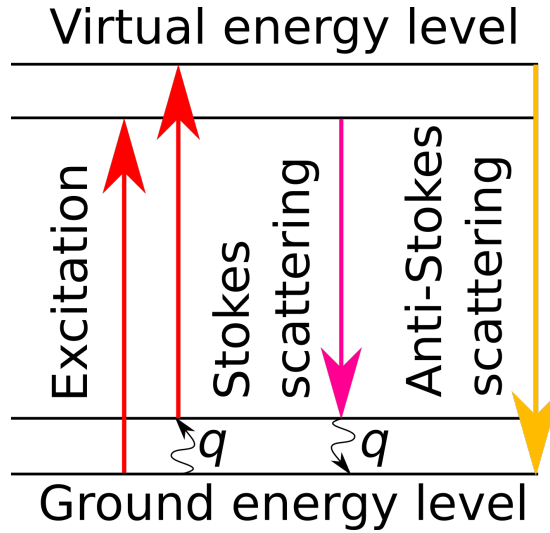


Figure 1.4: Raman laser energy diagram. q - phonon.

Some of the main characteristics of the Raman lasers, expertly pointed out in [57], are e.g. (i) there is no energy storage in the Raman laser cavity, (ii) a vast range of emission wavelengths are possible, limited only by the pump wavelength and losses of the Raman active material, (iii) the Raman process exhibits a "beam clean up" [28, 61, 62] making it possible to use a relatively poor quality pump beam which usually is a characteristic for very high power lasers and achieve high quality output beam from a Raman laser.

Different Raman active materials are characterized in [63, 64], and it was found that diamond has the highest Raman gain g_s , with barium nitrate $Ba(NO_3)_2$ having the second highest gain of only 60% of the diamond. The higher the Raman gain the lower the threshold for the Raman laser oscillation [65]. A comparison of the phonon energies in Raman active crystals was presented in [63]. The phonon energy dictates the difference between the incoming and scattered photons ($E = \hbar(\omega_i \pm \omega_L)$). Di-

amond's phonon energy is $\Omega_R = 1332.9\text{cm}^{-1}$ with the second highest CaCO_3 with $\Omega_R = 1086.4\text{cm}^{-1}$ (although with the Raman gain 100:6 compared to diamond) and the most commonly commercially available crystal being *KGW* with highest phonon energy of $\Omega_R = 901\text{cm}^{-1}$. These phonon energies have very important implications on the design of the eye-safe wavelength laser. The next paragraph is aimed to put the choice of diamond as a Raman gain medium in a context of available Raman laser pump source and other Raman active crystals.

The approach used in this project was to make use of the Yb fibre source at $1\mu\text{m}$ in tandem with Raman scattering in diamond to shift it to the eye-safe wavelengths. Doing so combines access to the high average powers and repetition rates provided by the fibre sources and then utilizes the high Raman gain in diamond to access eye-safe wavelengths. It has to be noted that most of the Yb-based sources mentioned here operate on $1.06\mu\text{m}$ wavelength - this wavelength is not long enough to reach the required $1.5\mu\text{m}$ with a second order Stokes shift. The minimum operating wavelength should be about $1.072\mu\text{m}$ assuming a Raman shift in diamond to be 1332cm^{-1} . This underlines the argument why the diamond is the enabling technology. The Yb fiber amplification bandwidth reaches about $1.15\mu\text{m}$ [66] which for a second order Stokes shift with a *KGW* crystal results in a $1.45\mu\text{m}$ emission wavelength. Figure 1.5 shows an output wavelength out of a second order Stokes Raman laser pumped by an Yb doped fibre laser working at $1.08\mu\text{m}$ depending on a Raman active material used for the wavelength conversion. It can be seen that only diamond allows for generation of wavelengths above the $1.5\mu\text{m}$ whereas using a *KGW* or BaWO_4 crystal would require using longer wavelength pump.

1.3.2 Linewidth and wavelength

This section aims to present how the linewidth and a center wavelength of a pump for a Raman laser impacts its Raman gain coefficient. The latter determines e.g. Raman laser efficiency as well as threshold since the intensity of the generated Raman scattered signal I_s increases as $I_s = I_s e^{g_s I_p}$ when pumping with the intensity I_p [67], where g_s is a Raman gain coefficient usually in units of $\frac{\text{cm}}{\text{GW}}$.

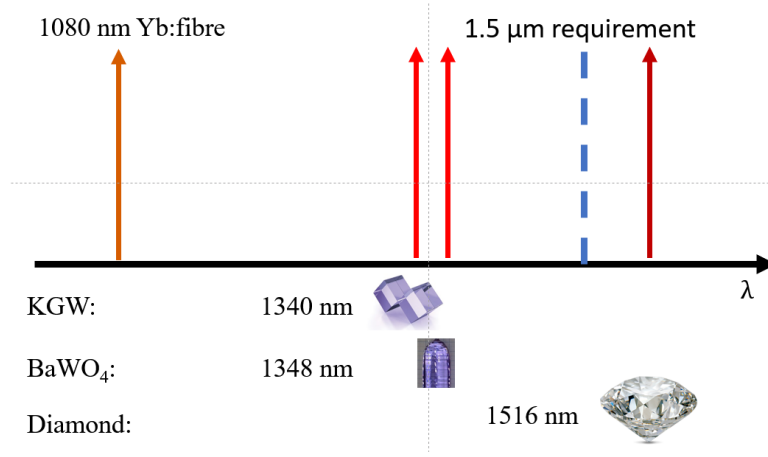


Figure 1.5: Wavelengths reached by a second order Raman conversion in different crystals when pumped by $1.08\mu m$ laser.

Raman scattering is generated by interaction of pump photons with crystal's lattice phonons which have a finite dephasing time (T_2) which determines the Raman gain linewidth $\Delta\nu_L = \frac{1}{T_2}$ [57, 68, 69]. For a synthetic diamond $T_2 = 7ps$ [70] which translates to a linewidth of $FWHM = 143GHz$ or $FWHM = 1.5cm^{-1}$ [71]. The Raman gain linewidth in diamond was measured by various groups to be around $0.2nm$ (or $2cm^{-1}$) at wavelength of $\lambda = 1\mu m$ [3, 71–73]. The threshold of a Raman laser is then dependent on the pump linewidth as presented in Equation 1.5 [74]:

$$I_i^{th(b)} = (1 + \Delta\nu_{pump}/\Delta\nu_{Raman}) I_i^{th(m)} \quad (1.5)$$

where $I_i^{th(b)}$ and $I_i^{th(m)}$ are threshold intensities for a broadband and monochromatic pumps and $\frac{\Delta\nu_{pump}}{\Delta\nu_{Raman}}$ is a ratio between pump and Raman gain linewidth. Therefore, narrowing the pump linewidth reduces the Raman threshold. Efficient Raman lasers require a narrow linewidth pump source as the efficiency falls off for $\frac{\Delta\nu_{pump}}{\Delta\nu_{Raman}} > 1$ [74]. In [75] it was shown, that narrowing the pump laser linewidth from $5cm^{-1}$ to $2cm^{-1}$ increases the Raman gain in diamond by 8%.

The Raman gain coefficient is pump wavelength dependent following Equation 1.6 [67]:

$$g_s = N \left(\frac{\partial\alpha}{\partial q} \right)^2 \frac{4\pi^2 \hbar \omega_{Stokes}}{n_i n_{Stokes} c^2 m \hbar \omega_L T_2} \quad (1.6)$$

Where N is the number density of scatterers, $\frac{\partial\alpha}{\partial q}$ is a polarizability term [76], n_i and n_{Stokes} are refractive indices at pump and Stokes emission wavelengths, ω_{Stokes} is a Stokes emission energy, ω_L is the phonon energy, m is a reduced mass of the scatterer and c is a speed of light. For a constant ω_L (material dependent), the Stokes energy is expressed as $\hbar\omega_{Stokes} = \hbar(\omega_{pump} \pm \omega_L)$ and therefore the Raman gain scales up with pump photon energy (inversely with pump wavelength). This was shown experimentally i.e. in [75] where the gain at $\lambda_i = 1.064\mu m$ was $g_s = 17\frac{cm}{GW}$ versus $g_s = 78\frac{cm}{GW}$ at $0.355\mu m$.

Another interesting consideration for optical cavities that are resonant both at Raman and pump wavelengths (Raman gain medium inside of the pumping laser cavity) is that the pump laser linewidth undergoes spectral broadening[77]. It is a result of the increase loss at a pump wavelength through the Raman generation process and making it possible for other longitudinal pump modes to oscillate around the main pump mode and therefore broadening the spectrum. For the external cavity Raman lasers, where the pump is not resonant, this broadening of the pump is not observed but considering a cascaded Raman effect, it is a point of discussion[78] if the lower order Stokes field can be treated as a spectrally broadened pump.

1.3.3 Polarization considerations

This section shows the how the Raman gain coefficient and output polarization depend on the pump input polarization following the Equation 1.7 [79–81] :

$$g_s \propto (\mathbf{e}_S \cdot \mathbf{R}_i \cdot \mathbf{e}_P) \quad (1.7)$$

,where the Raman gain coefficient g_s for the Stokes polarization indicated as a unit vector e_S is proportional to the pump beam polarization unit vector e_P , its direction of propagation and the Raman tensor R_i . Since the R_i is a tensor, the Raman gain is dependent on the directions of pump and Raman field vectors. Therefore, rotating the pump beam polarization will have an effect on the gain coefficient and in the

Raman laser, the Stokes polarization that will oscillate is the one with the highest gain coefficient. It has to be added, that the Equation 1.7 determines Raman gain coefficient in a position of the optical medium where the Raman scattering took place but does not involve the impact of the propagation of the laser modes in a birefringent optical medium - for reference this discussion is presented in [80]. The Raman gain in the Raman crystal then is given by [82]:

$$G = \frac{2g_s \arctan(\xi)}{\eta \Lambda} \quad (1.8)$$

, where g_s is a Raman gain coefficient, η is a quantum defect, Λ and ξ are parameters involving beam confocal parameters (double the Rayleigh range) of the pump and Stokes beams and crystal length.

The maximum Raman gain in a diamond based Raman laser was observed when the polarization of the pump was aligned with the $\langle 111 \rangle$ direction of the crystal [81, 83] which corresponds to a direction of the bonds between carbons in diamond[84]. The ratio of the Raman gain in a diamond Raman laser between using a pump polarized along $\langle 111 \rangle$ and $\langle 110 \rangle$ crystallographic directions was found to be 1.33 : 1[83].

In [79] a case of using unpolarized pumping for a first order Stokes diamond Raman laser is discussed. The pump was propagating along the $\langle 110 \rangle$ crystallographic direction and its polarization was rotated w.r.t. the optical axis between $\langle 110 \rangle$ and $\langle 100 \rangle$ diamond directions (noted as h and v directions respectively) with a half-wave plate. It was shown that either unpolarized or polarized pump results in a polarized Raman emission. The slope efficiency of about $\approx 85\%$ was achieved for the v polarization and $\approx 81\%$ for the h polarization with the maximum conversion efficiency of about 36%. The unpolarized pumping resulted in a slope efficiency of 81% the same as in a case of h polarization. The threshold for the unpolarized and h polarized pumping was increased by 22% when compared to the v polarized pumping. This is an important consideration for experiments presented in Chapter 4, where an unpolarized pumping was available. This review shows that the unpolarized pumping is possible and it has implication in the design of the pumping source.

1.4 Eye-safe laser sources overview

Section 1.2.4 mentioned that a laser at an eye-safe wavelength can be realized by using (i) a conventional laser material with a gain at $1.5\mu m$ or using (ii) nonlinear processes for wavelength conversion to $1.5\mu m$ e.g. in the Raman active crystal pumped by high peak power laser sources or optical parametric oscillators (OPOs). This section will briefly present an overview of both approaches. Firstly the overview of the state of the art of the conventional $1.5\mu m$ lasers is presented followed by a brief overview of the pump sources for the nonlinear conversion approach and finally an overview of reported Raman lasers.

1.4.1 Eye-safe wavelength lasers

Several groups reported on high power eye-safe wavelengths generation with the Er:Yb codoped fibre lasers e.g. $1.5\mu m$ $188W$ average power with $M2 = 1.9$ [35] source where the linewidth was about $1nm$. Another example was a recent Er doped Yb free fibre laser at $1601nm$ with $656W$ output power and $M2 = 10$ [36]. A master oscillator power amplifier (MOPA) was presented in [85] achieving $8W$ at $1.6\mu m$ with a $25MHz$ linewidth in all polarization maintaining (PM) fiber. These sources, although achieving impressive average powers with high beam qualities and in the latter case with extremely narrow linewidths are not meeting the requirements of LIDAR of working in a pulsed regime.

In pulsed mode, $1mJ$, $1.5W$ average power, $6.6kW$ peak power at $1.5kHz$ and $88ns$ pulse length at $1535nm$ with beam quality of about $M2 = 5$ [86] was achieved, power limitation was due to ASE (amplified spontaneous emission) in the fiber. Another pulsed source was presented in [87] with a use of large core diameter Er doped fibre in an amplifier configuration generating $1.1ns$ pulses, $10kHz$ repetition rate with $1.4mJ$ energy, $1.2MW$ peak power and $14W$ of average power at $1567nm$ with an $M2 = 8.5$. A pulsed source making use of an optical parametric oscillator (OPO) was presented emitting at $1534nm$ with a $5.3W$ output power, $3.71ns$ pulse lengths and $6kHz$ pulse repetition[88]. These sources although working in pulsed regime, are working at moder-

ate repetition rates and although the average power reaches over $10W$, there is a clear trade off with beam quality.

A high repetition rate laser was presented in [89] in an Er Yb codoped fiber laser system using chirped pulse amplification with $156MHz$ repetition rate with ultrafast $450fs$ pulse durations and $10W$ average power. This source had an excellent beam quality of $M2 \approx 1$ and could potentially be applicable to scanning LIDAR applications although this system emitted at a low pulse energy ($\approx pJ$) not suitable for flash LIDAR systems, also because of the ultrashort pulse duration, the broad spectrum ($> 10nm$) would prevent it to be used effectively in Doppler LIDAR configuration. Also it has to be added that the rest of the LIDAR system e.g. electronics etc. have to also be fast enough for such scanning rate. A passively Q-switched Er-doped fiber laser was presented in [90] with a multi wavelength emission around $1.5\mu m$ with 10 to $61kHz$ repetition rates and maximum of $27mW$ output average power which again is not suitable for LIDAR applications due to the low power. A high repetition Er fiber doped Master Oscillator Power Amplifier (MOPA - where a chain of amplifiers is seeded by a stable and narrow linewidth laser) system shown in [91] with a $1.5\mu m$ emission, narrow $0.2pm$ linewidth, $3.4kW$ peak power emitted with $2.3W$ of average power presents in turn a trade-off between narrow linewidth advantageous for Doppler LIDAR, but low average power. The newest publication (at the time of writing) was presented in [92] where an Er Yb:glass waveguide laser was used to produce $1.55\mu m$ emission with $3.2mJ$ output energy, $4kHz$ repetition rate and $12.8W$ average power with a pulse duration of about $0.6\mu s$ and the waveguide amplifier was seeded by a narrow linewidth source $< 100Hz$. This source although having high pulse energy and extremely narrow linewidth, has a very long pulse duration which is a drawback for a distance resolution in scanning LIDAR systems and is aimed at Doppler LIDAR technology.

It can be seen, that there is a trade-off between high power, beam quality and linewidth in the available eye-safe wavelength laser sources. The causes for these limitations are only briefly mentioned here as it is far beyond the scope of this work. As mentioned in [66], the performance of the Er doped fiber lasers is limited by processes such as upconversion through excited state pump absorption or ion pair quenching[93, 94]

which was found not to affect the gain in Yb based fibers even for high concentrations. Also as mentioned before, other issues such as stimulated Brillouin scattering etc. arises in high peak intensity narrow linewidth fiber lasers due to the long interaction length of the gain medium and the laser field[50]. Overall, the Yb based lasers have wide range of parameters such as repetition rate of output pulses, average powers, pulse energies although with large limitations at the eye-safe LIDAR required wavelengths.

1.4.2 Eye-safe optical parametric oscillators

One of the methods of wavelength conversion is a use of the OPO - by a use of the nonlinear crystal such as BBO, LBO or LiNbO₃, a wave of an energy E_1 generates two other waves of energies $E_3 = E_1 + E_2$ [40]. It has to be added, that the authors of the works presented in this Section usually mention the choice of the OPO above the Raman systems especially for the high energy sources due to the handling problems of the high pressure gas cells used in Raman sources. This further increases the importance of the development of the solid state Raman source at the eye-safe wavelengths.

Work presented in [95] shows a comparison of two eye-safe laser sources - one at $1.54\mu m$ which was a Stokes shifted $1.06\mu m$ Nd:YAG laser using a gas Raman cell and $1.57\mu m$ using a KTP OPO and the same pump source. In this work, the highest output energy reached at $100mJ$ pump was about $25mJ$ and $21ns$ pulse duration with the KTP and $27mJ$ and $14n$ with the Raman gas cell. The repetition rate was limited to about $100Hz$.

The other work including OPOs in [37] where a Q-switched Nd:YVO₄ laser pumped a KTA crystal achieving $1.1W$ of average power at $30kHz$ and $2.5ns$ pulse duration at $1.53\mu m$. In [96] a LIDAR system was presented at $1.55\mu m$ with a high $125mJ$ output energy and 30% conversion efficiency although about $20mJ$ was calculated to be in the other wavelengths that had to be filtered. The beam quality of this source was very good about $M^2 = 1.3$. Another relatively high energy - $8.1mJ$ source at $1.57\mu m$ presented in [97] was an intracavity Q-switched Nd:YAG with a KTP nonlinear crystal producing $5.9ns$ pulses at $5Hz$ operation. Another source presented in [98] shows an intracavity OPO based on a Q-switched Nd:YVO₄ achieving a $1.5W$ average power at

40kHz and 1.57 μ m wavelength and 4ns pulse duration at conversion efficiencies of 50% and $M^2 = 1.6$. Other sources in a W output power range and kHz repetition rate and eye-safe wavelengths were presented e.g. in [99–103].

The OPO technology then is a very compelling alternative to the Raman sources although there is a clear distinction between sources operating at very high energies (10–100mJ) and "high repetition rate" sources (≈ 10 –50kHz) with non of the reviewed OPOs reaching MHz repetition rate levels due to the thermal issues of the solid state laser pumping the OPO.

1.4.3 High power Raman laser pump sources at 1 μ m

Yb doped fibre sources working at 1 μ m are considered highly efficient and reliable sources for high power generation[66]. Reported were kW levels of CW power[104], high energy (2.3mJ) in pulsed mode (500Hz) at non conventional 1090nm wavelength (operation at above 1073nm wavelength is important to this project as is explained later)[105] and are suitable for working in high power > 100W MOPA configuration with excellent beam quality $M2 \approx 1.2$ and ≈ 20 ns pulse durations[66, 106]. It has to be mentioned, that the work in [106] presents a pump source for a diamond Raman laser in Chapter 4 and is described there in more detail. A laser source described in [107] presents a 100W average power ("limited by available pump power") with 908MHz repetition rate and 21ps pulse lengths. A previous work from this group [108] showed a 100W average power system after the seed (mode locked Yb fibre laser) amplification, 60MHz repetition rate, 16ps pulse width and excellent beam quality of $M2 < 1.5$. Looking at the available commercially sources based on Yb[109] one can find a 200W average power, 4MHz repetition rate, ns pulse duration range and ≈ 1.5 mJ pulse energy with a beam quality $M2 < 1.6$. These sources operate with a high repetition rate, high power and excellent beam quality and have very high peak powers.

1.4.4 Raman lasers overview

Many Raman lasers were presented using various Raman active media like silicon, diamond or KGW crystals[110–113]. One of the earliest solid state Raman lasers pre-

sented was based on passively Q-switched self-frequency conversion in Nd:KGW [114] in which the laser and Raman medium were the same optical crystal with the emission at $1.18\mu m$ and $0.97\mu m$ as Stokes and anti-Stokes wavelengths converted from $1.067\mu m$ fundamental laser oscillation.

The early Raman source based on diamond in an external cavity configuration was demonstrated in [115] where a Q-switched $532nm$ pump was converted into $573nm$ pulses with $0.3mJ$ output energy and 22% slope efficiency. A year later the same group improved their results to 75% slope efficiency, $0.67mJ$ output energy and $1.2W$ output power at $5kHz$ repetition rate [116]. Other visible wavelengths work is referenced in [113, 117]. An intracavity configuration was presented later on in [118] with output powers of $375mW$ at $1.2\mu m$ and $6.3kHz$ repetition rate by converting a $1\mu m$ Q-switched $Nd : YVO_4$ laser. The first venture into the high repetition rate and high average power was reported in first Stokes type diamond Raman laser [119] with an output power of $24.5W$ at $1.2\mu m$ and a 57% slope efficiency with $29ns$ pulse durations at $40kHz$ repetition rate.

In a CW mode, a high power diamond Raman laser pumped by a MOPA Yb based fiber laser source operating at $1060nm$ was presented in [45]. This particular work generated $154W$ of CW average power at first Stokes wavelength of $1234nm$ when pumped by $309W$ of a narrow linewidth ($0.16nm$) Yb fiber laser emission. The limitations in power scaling were imposed mostly by the amount of heat deposited on the Raman laser input coupler and back scattered light going back to the fiber amplification chain. The power scaling of up to $381W$ with 61% conversion efficiency was achieved when operating the fiber laser in QCW regime with $10ms$ pulses which reduced the thermal loading of the system. A second Stokes diamond Raman laser in [120] was presented where $21.8W$ of CW average power at $1.5\mu m$ was generated pumped by an Yb fiber laser with $191W$ CW average power. In [121] a diamond Raman laser operating at $1.4\mu m$ was presented generating an average CW power of $34W$ with a 11% conversion efficiency limited mainly by the temperatures generated on the Raman laser mirrors. This constant improvement shows, that the diamond Raman lasers are capable of generating high powers. It is also worth reiterating, that most of the pump sources used

are Yb based fibers or YAG lasers operating at "standard" wavelengths not allowing the second Stokes to reach wavelengths above $1.5\mu m$ with a few presented exceptions.

Second Stokes diamond Raman lasers most relevant to this thesis were presented in [38, 83]. These lasers were pumped with a $1.064\mu m$ Nd:YAG laser in pulsed regime and an external cavity configuration reaching wavelengths of $1.485\mu m$; the output average power reached $1.63W$ with a $5kHz$ repetition rate and 51% power conversion efficiency and pulse energies of $0.3mJ$.

Other work on generating eye-safe wavelengths using a Raman phenomena was presented in [122] where in intracavity configuration, an Nd:YAG crystal oscillating at $1.3\mu m$ was used as a pump to generate $1.5\mu m$ emission from a $Ba(NO_3)_2$ crystal with a very high $12mJ$ output energy from $25mJ$ of pump with a drawback of repetition rate being limited to $1Hz$ due to the thermal effects. Self-frequency Raman conversion in Nd:YVO₄ Q-switched laser operating at $1.3\mu m$ was presented in [123] achieving $1.2W$ average power, $60\mu J$, $10kW$ peak power at $20kHz$ repetition rate at $1.5\mu m$. Later the group improved the laser performance to $2.2W$ of average power at $40kHz$ and $55\mu J$ with a 13% conversion efficiency[124]. Another self-frequency conversion, this time in Nd:KGW Q-switched laser operating at $1.3\mu m$ was presented achieving output energies of $31.8mJ$ in $2ns$ pulses at $10Hz$ repetition rate with $1.5\mu m$ emission[125] followed by work presented in [126] where a Q-switched Nd:KGW laser with its multimode emission converted to a $1.5\mu m$ radiation of $7mJ$ and $15ns$ pulse duration at a conversion efficiency of 20%. It is worth to mention work presented in [127], where a cascaded fiber Raman laser achieved a $301W$ of CW average output power at $1.48\mu m$ with over 60% conversion efficiency from $1\mu m$ emission of the Yb based fiber laser to $1.4\mu m$ of the Raman emission.

Work presented in [28, 61, 128, 129] focused on brightness enhancement, where brightness B is proportional to the laser power P divided by the laser beam angle of divergence ϕ and its diameter D ; $B = \frac{4P}{(\pi D\phi)^2}$ [40]. A beam divergence of a Gaussian beam can be expressed by $\phi = M^2(\frac{\lambda}{\pi w})$, where λ is a laser wavelength, w is its beam waist radius and M^2 is a beam quality parameter. The brightness enhancement in this case is then reducing the M^2 parameter. In extreme case, pumping of the diamond

Raman laser with a poor pump quality of $M2 = 15$ was shown to improve the Raman laser output to $M2 = 3$ depending on the pump power[129]. This was relevant in Chapter 4 where switching to a pump source of a worse beam quality ($M2 = 5$ from $M2 = 1.1$) improved the reliability of a system making it possible to operate for a prolonged periods of time.

1.5 Driving of the Raman process

This section presents methods of pumping of the Raman laser that were implemented in this thesis. Firstly we will look at the possible configurations of the Raman lasers and amplifier followed by the description of the methods of generating high peak power that would efficiently drive the Raman signal generation process.

1.5.1 Raman laser configurations

Raman lasers are able to operate in different configurations shown in Figure 1.6 and each will be described in this section.

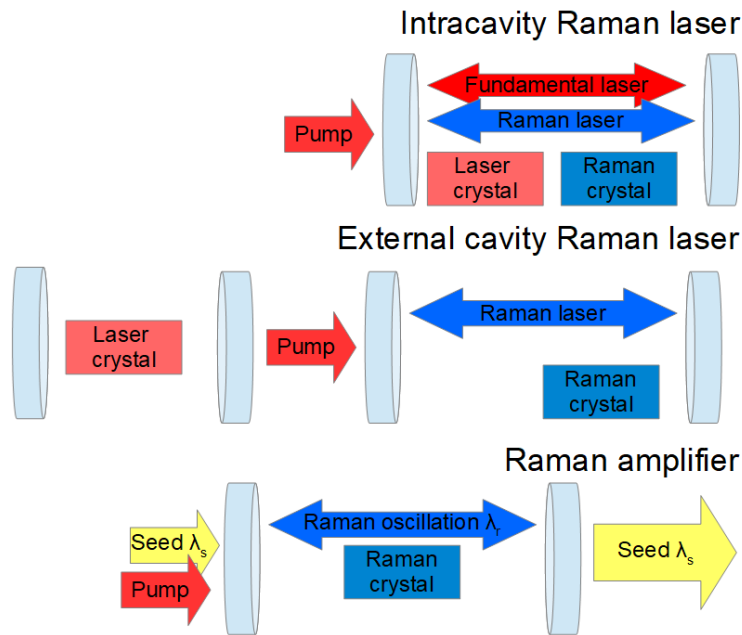


Figure 1.6: Configurations of the Raman lasers - intracavity and external cavity configurations and Raman amplifier with external seeding.

External cavity configuration (the most common) where the external pump beam is focused into a standalone Raman cavity resonant at Stokes wavelength was used e.g. in [38, 61, 75, 83, 113]. The Raman threshold in [83] for a first Stokes Raman laser at $1.2\mu m$ was about $30\frac{MW}{cm^2}$ of a $1\mu m$ pump with about $10ns$ pulse duration at $5kHz$ repetition rate. The external cavity design is simplified in comparison to the intracavity configuration since the considerations for the mode size design of the pump and Stokes fields are separated.

In the intracavity configuration, a diamond Raman laser was presented in a pulsed regime in [130] and CW operation was shown in i.e. [131, 132]. The threshold intensity is expected to be the same as in the external cavity case although the high pump intensity for Raman laser can be accessed easier due to the high reflectivity of the Raman laser cavity mirrors at the pump wavelength. Such mirror configuration reduces threshold of the pump laser and in an example of the intracavity solid state laser, relaxes the diode pump power requirement. Since the intracavity Raman laser is resonant at both pump and Stokes wavelength the mode size considerations extend to all of the wavelengths oscillating in this cavity.

The configuration chosen for this project was external cavity due to a fact that the master oscillator power amplifier (MOPA) fiber system used as a pump in Chapter 4 was not compatible with intracavity configuration.

1.5.2 Diamond Raman amplifier

An alternative method is an amplifier configuration as seen on Figure 1.6. This type of a laser system consists of two parts - a seed which operates at a desired wavelength and the amplifier which is essentially an external cavity Raman laser with highly reflective mirrors at (in this particular case) first Stokes wavelengths and non reflective mirrors at a second Stokes wavelength. Therefore all energy transferred from the pump to the first Stokes field is oscillating within the cavity with minimum losses. This energy is then extracted by the seed laser with the wavelength tuned to the second Stokes of the Raman laser cavity. Gas Raman amplifiers have been demonstrated previously i.e. in [133] but no Raman amplifier was demonstrated using diamond. The difference

between straight forward generation of Stokes emission in a Raman laser and the amplifier is that the latter emission is defined by the characteristics of the seed laser. This is especially important for the Doppler LIDAR applications[8] where a narrow linewidth sources are required to improve upon speed measurement resolution. As an example, a KGW intracavity Raman laser shown in [134] was a basis to investigate the impact of the pump linewidth on the Raman emission. The intracavity pump linewidth was varied from 1.2cm^{-1} to 0.6cm^{-1} and no particular change in Raman emission linewidth (1.2cm^{-1}) was observed. When the Raman cavity was seeded by the external narrow linewidth (0.4cm^{-1}) laser source, the seed after the amplification retained its linewidth. It might draw conclusions that seeding of the Raman laser systems is a way of achieving a narrow linewidth Raman laser source.

The principle of the Raman amplifier is now described. When a seed laser beam passes through the cavity in amplifier configuration and its wavelength corresponds to the second Stokes shift in the Raman crystal the seed signal is amplified through the stimulated Raman scattering. This is explained by looking at Figure 1.4, where in the case of second Stokes wavelength amplification, excitation is a first Stokes intracavity field creating phonons that contribute to gain at second Stokes wavelength. Since the second Stokes field is not resonant, in the absence of the seed, the emission of the second Stokes originates mostly from inefficient spontaneous Raman scattering. It has to be noted, that some stimulated Raman scattering can still occur due to reflections from optical surfaces. An external photon of a seed laser can then stimulate the Raman scattering at the second Stokes. Following work in [68, 69] it can be seen, that the amplification is highest at the peak of the Raman gain spectrum therefore a seed has to be sufficiently narrow spectrally and be centered on the Raman gain peak. In pulsed operating regime, the pump driving generation of the first Stokes field has to be synchronized with the seed laser pulses since the amplification is only present when the Stokes field is present.

Having now reviewed possible configurations of Raman lasers as well as an overview of the Raman sources using diamond, the next Section will present the requirements for the pump source.

1.5.3 High peak power generation

The condition of the pump peak intensity to reach the Raman laser threshold is described in the Equation 1.9[68], where R are reflectivities of the laser cavity mirrors assumed to be $R_1 = 0.99$ and $R_2 = 0.8$. For a reasonable length of a Raman crystal of $5mm$ and gain coefficient g_s in the order of $\frac{cm}{GW}$ (wavelength dependent) [75, 111], pump peak intensity has to be in a range of tens to hundreds of $\frac{MW}{cm^2}$ to achieve threshold which corresponds to a value of couple of kW peak power focused to pump spot diameter $\approx 100\mu m$ at threshold for the Stokes generation.

$$R_1 R_2 \exp(2g_s I_p l) \geq 1 \quad (1.9)$$

The methods chosen to achieve high peak power for the pump of the Raman laser in this work were (i) Q-switching for the small scale test setup of a second Stokes diamond Raman laser presented in Chapter 3 (ii) using an Yb MOPA fiber system for diamond Raman laser pumping in Chapter 4 where a pulsed seed laser operating at relatively high repetition rates compared to (i) is amplified in a chain of fiber amplifiers to reach high average and peak power. These two methods are described now.

Q-switching

Q-factor of an optical cavity is a relation between laser cavity "stored energy to energy lost in one cycle of oscillation" [40]. If the Q-factor is low, and so the round trip losses are large, there is no laser oscillation and all the stored energy is lost to spontaneous emission. If the Q-factor is high, and so the round trip losses are low, laser oscillation can be sustained and most of the energy stored in the gain medium can be extracted via stimulated emission.

Figure 1.7 shows a time dependent population inversion in a laser gain medium and giant pulse generation in a Q-switching process. It can be seen that when the pump starts and with the lack of stimulated emission, the excited state population in a laser gain medium N_2 starts to grow following the Equation $\frac{dN_2}{dt} = R_p - \frac{N_2}{\tau}$ [40], where the

τ is the lifetime of the excited state and R_p is pumping rate. Because the Q-factor of the cavity at this time is low, the threshold for lasing is high and no laser oscillation is present for a relatively high population inversion. The delay time Δt between starting the pumping process and switching the Q factor to high is often set to the time needed to achieve maximum population inversion. Inversion saturates at maximum value due to the spontaneous emission being balanced by the pumping rate. Then the Q-factor is switched (for the time Δw) to high and because the laser threshold is now relatively low compared to the level of population inversion - most of the stored energy in the gain medium can be emitted in a giant high energy pulse. The start of such pulse begins with a spontaneously emitted photon being amplified in a gain medium with a high level of population inversion causing the pulse rise edge to grow, at the top of the pulse, most of the population inversion is brought back to the ground state through the stimulated emission process to the lasing threshold. Then the ringdown of the intracavity field causes the falling edge of the pulse with a duration of the cavity photon decay time $\tau_c = \frac{L}{c\Gamma}$ [40], where L is a length of the cavity, c is a speed of light and Γ is a roundtrip cavity loss consisting of output coupling as well as parasitic losses.

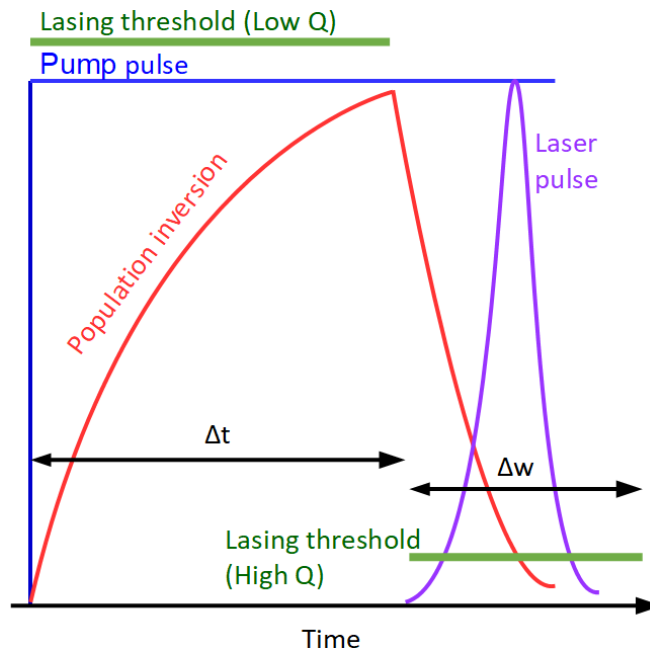


Figure 1.7: Population inversion and laser threshold in the Q-switch lasers.

The energy of the emitted pulse is quantified by the Equation 1.10[40].

$$E = \left(\frac{\gamma_2}{2} \frac{N_i}{N_p} \eta_E\right) \left(\frac{A_b}{\sigma}\right) h\nu \quad (1.10)$$

, where γ_2 is an output coupler transmission, $\frac{N_i}{N_p}$ is a ratio of the maximum (before Q-switch is opened) to the threshold (at the peak of the Q-switched pulse) level of population inversion, η_E is energy utilization factor, A_b is the mode area, σ is an emission cross section and $h\nu$ is a photon energy at the lasing wavelength. Therefore, the higher the population inversion the higher the energy of the output pulse that is possible to achieve.

The duration of the achieved pulse is described by the Equation 1.11[40], which implies that the higher the output coupling (cavity losses determine τ_c) and the higher the ratio $\frac{N_i}{N_p}$ the shorter the output Q-switched pulse. Usually, the pulse duration achieved in Q-switching of the solid state laser are in range of tens of *ns*. The expected energy of the pulse to be achieved in the Q-switching process might be in the *mJ* range.

$$\Delta\tau_p = \tau_c \frac{(N_i/N_p) \eta_E}{[(N_i/N_p) - \ln(N_i/N_p) - 1]} \quad (1.11)$$

Master Oscillator Power Amplifier

As previously mentioned, a second approach towards generating high peak intensities is to make use of a MOPA configuration where the seed laser with a set repetition rate, pulse length, linewidth and wavelength is then amplified in a series of amplification stages. Chapter 4 presents briefly a system developed by collaborators in Optoelectronics Research Center in Southampton University[106]. In this project a seed laser was a distributed Bragg reflector diode emitting at $1\mu m$ wavelength with a narrow linewidth of about $0.2nm$ in CW regime. Then the output was shaped into pulses with acousto-optic modulator. The advantage of that instead of using current modulation is that the latter can cause a modulation of the wavelength through the e.g. temperature modulation. The seed laser can have a low output power since it is amplified to the required energy and peak powers in the amplification chain. The design of this system is beyond

the scope of this thesis, but the main considerations are that the seed is first amplified with a high gain pre-amplification stages (small diameter Yb doped fiber amplifiers) to reach the saturation powers of the last power amplification stage. The latter had a larger diameter core fiber which allowed for reaching high powers since the saturation power is proportional to the area of the mode [135]. The required pulse peak powers to reach the diamond Raman laser threshold are the same as in the case of Nd:YAP small scale system and are about $P_{peak} = 5kW$. At the same time, the fiber MOPA system was capable of reaching relatively high repetition rates; assuming a moderate rate of $150kHz$ and $20ns$ pulse durations then the second Stokes laser threshold should be at average power of about $15W$. The ultimate goal of using this system was to achieve pump limited powers at levels.

1.6 Summary

In this Chapter it was shown that there is a place in the LIDAR laser source market for a high power, high repetition rate laser working at the eye safe wavelength and this was the motivation for a project presented in this thesis. The method that was chosen was to use a diamond crystal as a Raman gain medium in order to shift the $1\mu m$ wavelength of the high power high repetition rate Yb fiber based MOPA system to $1.5\mu m$. Requirements for characteristics of the pump such as peak intensity, polarization and linewidth were outlined in this Chapter that would allow for efficient wavelength conversion in the diamond Raman laser. Methods for reaching required high peak intensities used in this thesis were described in Section 1.5. As a reference, Section 1.4 provided some of the available eye-safe wavelength sources reported in the literature.

Now an overview of the further chapters is presented. Firstly, **Chapter 2** will provide a tool to model an external cavity Raman laser. This chapter describes not only optimization of the Raman cavity such as choosing an output coupler or mode sizes but also provides a useful analysis tool to explain the physics behind the experiment but also to inform diamond growers about what size and absorption parameters are acceptable for best Raman laser performance. **Chapter 3** shows a process of a design of the high

Chapter 1. Introduction

peak power laser as a pump for the diamond Raman laser (DRL) also described in the same chapter. This system was invaluable in gaining experience in alignment as well as assessing and measuring the parameters important for the performance of the DRL. The findings of the Chapter 3 were then a foundation for the analysis of the system described in **Chapter 4** which presents a high power high repetition rate DRL pumped by a fiber MOPA which was built with cooperation with the Southampton University team. The **Chapter 5** concludes experimental part of the thesis with somewhat limited (due to the time constraints) measurements of the alternative approach towards amplification of the eye-safe wavelengths in the diamond Raman amplifier system.

Chapter 2

Modeling of Raman diamond lasers

2.1 Modeling of the Diamond Raman Laser performance

Modelling of the diamond Raman laser is presented in this Chapter. The considered Raman laser cavity is presented in Figure 2.1. The pump pulses come into the two mirror cavity (from left) at a frequency ν_P and certain peak power $P_{peak} = \frac{E}{\Delta t}$, where E is the energy of a pulse of duration Δt . The input and output couplers are characterized by their reflectivities R_{i2} and R_{i1} respectively, where k is the Stokes order. The diamond is characterized by its length l_R , absorption α_k and Raman gain g_r coefficient at a given Stokes order. The output emission is at a frequency ν_S determined by the Raman shift of the Raman crystal.

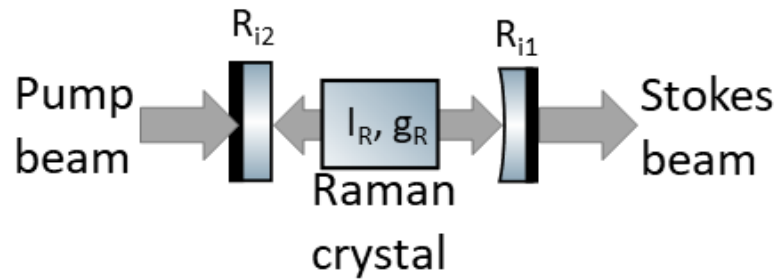


Figure 2.1: A model of the external cavity Raman laser. Pump beam is incident onto the crystal through an input coupler and the Raman signal is resonant in the cavity.

For a second Stokes operation, the input coupler is coated with an anti-reflective coating at the pump wavelength and highly reflective coating at first and second Stokes wavelengths. The output coupler is highly reflective at a pump wavelength (double pass configuration) and the first Stokes and partially reflective at a second Stokes wavelength. The diamond is a plane-plane crystal with optical facets coated with an anti-reflective coating at all wavelengths of interest providing minimum intracavity losses.

Firstly an overview of the model is provided. This model was used as a design tool for the Raman laser cavity in determining its output coupling, length and the dependence of the laser performance on the pumping spot size and Raman mode sizes. The model was also used to create a comment on the optimum values for the diamond as a Raman gain medium such as absorption and crystal length. These two parameters are controllable, within certain practical limits, by the material growers so the conclusions (in Section 6.2) were drawn to help in optimising the production of synthetic diamond for Raman lasers. The laser mode sizes were calculated using the ABCD matrix method presented in the later part of this chapter.

2.2 Model overview

The model was based on work in [136], adapted for use in the solid state laser system using appropriate parameters and modified to include the influence of the spontaneous Raman scattering as shown in e.g. [65, 67]. Second modification was to include an area overlap function between Stokes and pump modes as presented in [137]. The modification will be presented in more detail throughout the text. Although this paper presented theoretical considerations for a cascaded fiber Raman laser, the model is also applicable for the external cavity diamond Raman laser in the Schematic 2.1 relevant for this thesis. The coding for this model was started by the author by implementation in MatLab and finished by Florian Worme as part of a summer internship at the University of Strathclyde, working with Dr Vasili Savitski and the author. Now the equations governing the flow of energy between pump and Stokes field in the Raman

crystal will be presented.

$$\frac{dP_p^{F/B}}{dz} = -\alpha_p P_p^{F/B} - \frac{v_p}{v_{s1}} \frac{g_R^1}{A_{\text{eff}}^1} (P_{s1}^F + P_{s1}^B) P_p^{F/B} \quad (2.1)$$

$$\begin{aligned} \frac{dP_{s1}^{F/B}}{dz} = & -\alpha_{s1} P_{s1}^{F/B} - \frac{v_{s1}}{v_{s2}} \frac{g_R^{s1}}{A_{\text{eff}}^{p,s1}} (P_{s2}^F + P_{s2}^B) P_{s1}^{F/B} \\ & + \frac{g_R^p}{A_{\text{eff}}^{p,s1}} (P_p^F + P_p^B) P_{s1}^{F/B} + K_{sp} (P_p^F + P_p^B) \end{aligned} \quad (2.2)$$

$$\frac{dP_{s2}^{F/B}}{dz} = -\alpha_{s2} P_{s2}^{F/B} + \frac{g_R^{s2}}{A_{\text{eff}}^{s1,s2}} (P_{s1}^F + P_{s1}^B) P_{s2}^{F/B} + K_{sp} (P_{s1}^F + P_{s1}^B) \quad (2.3)$$

Equation 2.1 governs the pump power P_p evolution over propagation length z and its power transfer to first Stokes power P_{s1} . The first term on the right hand side α_p represents absorption of the pump. The second term governs the flow of energy from the first Stokes field (of power P_{s1} from the backward and forward traveling components of the pump field, P_p^F and P_p^B respectively, scaled by the pump and Stokes optical frequencies ratio $\frac{\nu_P}{\nu_{S1}}$ and the effective interaction area of the Stokes and pump modes A_{eff} . The calculation of the effective area was based on work in [137]; $A_{\text{eff}} = \frac{\pi(w^2(\lambda_S, z) + w^2(\lambda_F, z))}{2}$ where w is the mode radius position at z for the fundamental λ_F or Stokes wavelengths λ_S [38, 137, 138]. The fundamental field in this case can be either a pump or Stokes field that is the source of the energy flow into the higher order Stokes field.

Equation 2.2 governs the signal evolution of the first order Stokes field oscillating over the length of the Raman laser cavity and Equation 2.3 shows the second Stokes order evolution which is outcoupled from the Raman laser cavity and it is assumed no higher order modes are involved in the scattering process.

The negative terms on the right hand side of the Equations 2.2 and 2.3 represent attenuation of the signal due to a diamond bulk absorption as well as AR coatings of diamond and mirrors and the transfer of the first Stokes order power $P_{s1}^{F/B}$ to the forward and backward propagating $P_{s2}^F + P_{s2}^B$ power of the second Stokes order. This power transfer is dependent on the Raman gain g_R at a pump wavelength scaled to the

appropriate Stokes order by multiplying it by the ratio of the pump to the first Stokes wavelength $\frac{\nu_p}{\nu_{s1}}$, over the effective area A_{eff} .

Positive terms in Equations 2.2 and 2.3 show the transfer of energy from the pump to the first Stokes and first Stokes to the second Stokes field respectively. This energy transfer is governed by the product of the sum of forward and backward propagating fundamental and Stokes fields $(P_f^F + P_f^B)P_{si}^{F/B}$ scaled by the Raman gain coefficient g_R over an effective area A_{eff} . This influence of the beforementioned spontaneous scattering is represented by signal $P_{sp,s1}^{F/B} = K_{sp}(P_p^F + P_p^B)$, where K_{sp} is a spontaneous scattering factor. The negative term contributing to the spontaneous scattering in the Equation 2.1 is omitted, because not all of the scattered photons will end up contributing to the first Stokes laser mode. Instead this was adjusted by reduction of the Raman gain coefficient at the pump wavelength which was more convenient.

After each roundtrip, the intracavity pump and Stokes fields $P_{p,s}$ are multiplied by the mirror reflectivity - R_1 in case of bouncing off the output coupler and R_2 off the input coupler.

$$P_{p,s} = R_{1,2} \times P_{p,s} \quad (2.4)$$

The output power for the second Stokes laser is then defined by the output coupler reflectivity at the second Stokes wavelength following

$$P_{out,s2} = P_{s2}^F * (1 - R_1) \quad (2.5)$$

In the pulsed regime, the pump and Stokes fields were divided into dt segments one by one transferred through the Raman crystal model. The energy of the emitted second Stokes order pulse E could be then found by integrating the instantaneous power of the pulse in a time dt following

$$E = \int_{-\text{inf}}^{\text{inf}} P_{out,s2} dt \quad (2.6)$$

It has to be mentioned, that the absorption coefficients α consist of bulk diamond absorption as well as losses on the AR coatings on the diamond surfaces following equation:

$$\alpha = \frac{2(AR_1 + AR_2)}{L} + \alpha_{abs} \times L \quad (2.7)$$

,where L is a length of the crystal, AR_1 and AR_2 are losses on the AR coatings at the diamond surfaces at a given wavelength and α_{abs} is a bulk diamond absorption.

The MatLab implementation consists of firstly initiating the parameters of the model like Raman gain coefficient, reflectivity values of mirrors and diamond surfaces, K_{sp} starting noise values. Then the initial power of each Stokes order in each of the dz segment of the Raman crystal is set to the starting noise value. The input pump pulse, divided into time segments dt was transmitted through each of the spatial segment dz of the cavity updating the pump and Stokes fields values using Equations 2.1 2.2 and 2.3. In each time step dt then, the instantaneous power of each Stokes field in dz segment is a sum of the incident fields at a time dt propagating in forward and backward directions. This was consistent with a model for the external Raman laser which was presented in [65].

As mentioned in [38], the resulting simulated pulses had to be filtered to simulate the photo detector's response. In this case, the low pass filter's cut-off frequency was $215MHz$ at the $3dB$ point implemented by a MatLab smoothing function *butter* which is a Butterworth filter. This frequency was chosen empirically to reduce the spikes in the unfiltered simulated pulses and to closely resemble the experimentally recorded pulses with a $350MHz$ photodetector. Figure 2.2 shows simulated second Stokes pulse with and without smoothing the pulse.

This section showed the overview of the Raman laser model. It could be seen, that the laser mode size plays an important role because of the A_{eff} factor in the equations for the energy transfer between subsequent Stokes fields. The size of the laser modes can be determined using ABCD matrix method which is presented next.

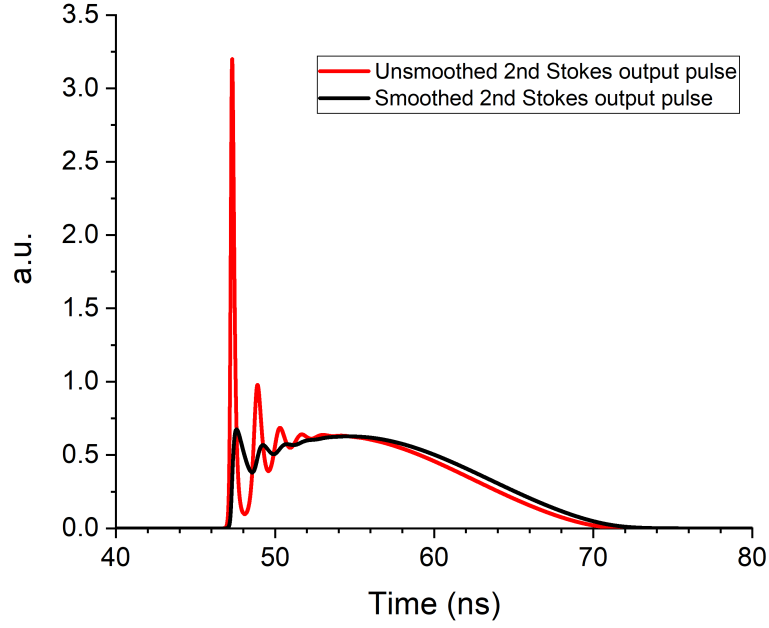


Figure 2.2: Smoothing function applied to the Stokes output pulse normalized by the pulse energy.

2.3 ABCD matrix cavity design

A Gaussian beam complex parameter q can be used to fully describe its parameters and therefore intensity distribution following Equation 2.8

$$\frac{1}{q} = \frac{1}{R} - j\frac{\lambda}{\pi w^2} \quad (2.8)$$

where R is a propagating wave radius of curvature, λ is a wavelength and w is the Gaussian beam radius.

The intensity distribution of a Gaussian beam after propagating through the optical system described by the $ABCD$ parameters is shown in Equation 2.9 [40]:

$$u(x, y, z) = \frac{1}{A + (B/q_1)} \exp -jk \frac{x^2 + y^2}{2q} \quad (2.9)$$

where $u(x, y, z)$ is an intensity distribution over x, y plane after propagating in a z direction, $k = \frac{2\pi}{\lambda}$ is a wave vector and q_1 is a complex beam parameter of the initial Gaussian beam.

Extending this beam propagation principle to the laser cavities, in a stable cavity, the condition of $q = \frac{Aq_1 + B}{Cq_1 + D}$ must be satisfied at each roundtrip in any position in the cavity. Therefore for the $ABCD$ matrix describing the laser cavity, a laser mode spatial and phase parameters can be calculated when substituting Equation 2.8 to Equation 2.9. A free software reZonator was used simulating the laser cavity[139] and it was based on this method. In the next section it is shown how the calculation of the laser cavity mode size and stability using the $ABCD$ matrix method can indicate the impact of the thermal lens. In this case, a stable laser cavity is referred to as supporting oscillation of the low spatial order TEM₀₀ Gaussian beam at a given wavelength.

2.4 Thermal lens impact on the cavity stability

A brief case study is now presented of the impact of the thermal lensing on the DRL cavity stability. The stability of the laser resonator is understood as such a geometric configuration of the cavity tht it is able to support oscillation of the laser mode. When the cavity is out of the stable condition, no laser mode can oscillate and the laser action is not possible. The cavity stability can be described with a condition in Equation 2.10 [40]:

$$0 < 1 - \left(\frac{A + D}{2}\right)^2 \leq 1 \quad (2.10)$$

,where the elements in the laser cavity create an optical system of $ABCD$ parameters.

The cavity model that allows for the simulation of the thermal lens is presented in Figure 2.3. Figure shows a cavity which consists of two mirrors: plane input coupler, $ROC = 50mm$ output coupler and a $4mm$ diamond with about $10mm$ free space and a simulated thermal lens.

The thermal lens strength f^{-1} presented in Equation 2.11[45] depends on various contributors such as deposited heat P_{dep} , refractive index n , Poisson's ratio ν , absorption coefficient α_T , T_c is a thermal conductivity and photoelastic coefficient C . As mentioned in [45, 140], in diamond, only the $\frac{dn}{dT}$ needs to be taken into account since the other contributions such as bulging of the crystal end facets and the photo-elastic effect (refractive index change with thermally induced stress[141]) are orders of magni-

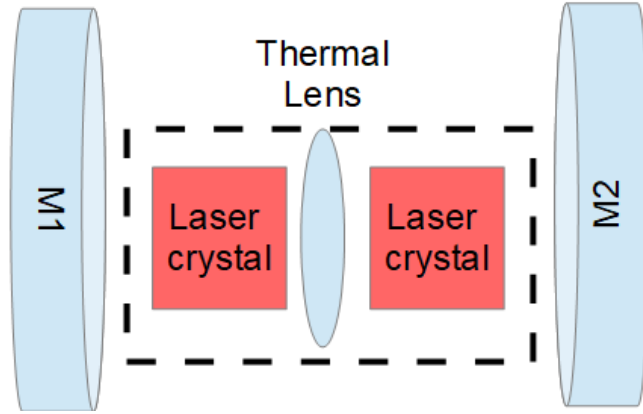


Figure 2.3: Laser cavity with a laser crystal with a thermal lens. M1 - input coupler, M2 - output coupler.

tude lower. For example the bulging is caused by the material expansion due to heat and for diamond the thermal expansion coefficient is $1.1 \times 10^{-6} K^{-1}$ [45] which is much lower than $7.9 \times 10^{-6} K^{-1}$ [44] of a Nd:YAG crystal.

$$f^{-1} = \frac{P_{\text{dep}}}{2\pi T_c \omega_0^2} \left(\frac{dn}{dT} + (n-1)(\nu+1)\alpha_T + n^3 \alpha_T C \right) \quad (2.11)$$

Figure 2.4 shows the cause of the formation of the thermal lens. The heat deposited in the diamond through the optical pumping with a Gaussian spatial distribution is shown by a dotted red line. The pump beam is focused into the crystal and the resulting heat gradient causes a refractive index change over the transverse coordinates of the laser crystal, where the highest heat is deposited in the center of the crystal and falling off to its edges. The circular arrow indicates rotational symmetry of the system.

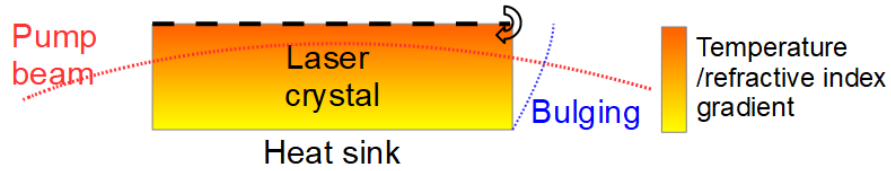


Figure 2.4: Heat and refractive index gradient distribution over an optically pumped crystal. Pump beam is indicated with a red dotted line and the bulging effect with blue dotted line. Dashed line indicates axis of the symmetry.

It is worth mentioning here, that the $\frac{dn}{dT}$ coefficient in diamond is $1.5 \times 10^{-5} K^{-1}$ [45] which is in the same order of magnitude as Nd:YAG $\frac{dn}{dT} = 0.73 \times 10^{-5} K^{-1}$ [142], but the important difference is that because the thermal conductivity of diamond is $T_c = 2400 W m^{-1} K^{-1}$ as compared to conventional laser material such as YAG with $T_c = 11 W m^{-1} K^{-1}$ (ref. Section 1.2.3), for the same deposited power P_{dep} , the strength of the thermal lens in diamond is expected to be about 100 times smaller than in Nd:YAG (ratio of the thermal conductivity of diamond to Nd:YAG).

The thermal lens can be used in a laser cavity ABCD model and by varying its focal length, a stability and the intracavity laser mode size can be analyzed. Figure 2.5 shows the variation of the DRL laser cavity stability parameter versus thermal lens focal length. It can be seen, that the cavity is stable up to a focal length of near a few mm point although this is not to say that it will not impact the laser performance. Zooming in near the $f = 0 mm$ point, the cavity is unstable at $f = 0 - 2 mm$ and then $f = 3 - 6 mm$ which represent a very strong thermal lens. In terms of laser mode diameter change, also shown in the Figure 2.5, the mode diameter can change from $185 \mu m$ to $140 \mu m$ for a thermal lens between $400 mm$ and $5 mm$. This thermal lens model was used in the Raman cavity design to mainly determine if the laser mode sizes would change substantially as the laser mode size affects the energy transfer between subsequent Stokes laser sizes through the overlap area factor as is described in detail in the Section 2.2. Taking into account assumed deposited power of $100 W$ (let's say in a much improved system in Chapter 4) and pump spot diameter of $144 \mu m$, the thermal lens in the diamond Raman cavity would be around $500 mm$ not really reaching the very strong lensing effects. Focusing tighter in the future experiments to improve the conversion efficiency might lead to introducing a stronger thermal lens.

To complicate the picture of thermal lensing, an extreme case in a diamond Raman laser presented in [45], the calculated thermal lens in diamond with the heat load of about $60 W$ and a $40 \mu m$ pump diameter was about $f = 6 mm$ which would destabilize the laser mode oscillations, but as also stated, the minimum lens strength for which the cavity would still be stable was $f = 28 mm$. Additionally, for the lens approaching the stability limit, the authors indicated that the laser modes would change reducing

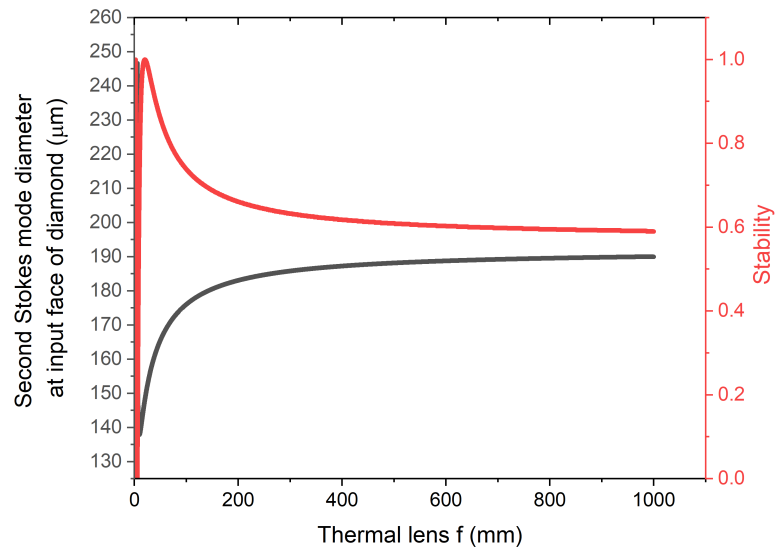


Figure 2.5: Stability of the diamond Raman laser cavity against a thermal lens strength in the diamond crystal.

the laser efficiency. The model in Equation 2.11 might not be sufficient to fully predict thermal lensing in diamond not including effects such as guiding effects [143].

2.5 Summary

This Chapter presented a model used for the optimization of the diamond Raman laser in terms of pump energy and peak intensity but also in terms of the Stokes mode sizes. The results of these optimization of the DRL are presented in the experimental chapters where it is relevant. The model was also used to simulate the efficiency of the diamond Raman laser by changing the length of the diamond as well as its absorption coefficient which could be a useful information to the material growers. These diamond consideration results are presented in Chapter 6. Having presented the tools needed for the Raman laser design, the proof of concept laser is presented in Chapter 3 and its high power version in Chapter 4.

Chapter 3

Diamond Raman Laser prototype

Chapter 2 presented tools that were needed to design a laser cavity namely: calculation of mode sizing through ABCD method and optimization of the Raman laser performance using parameters such as pump spot diameter and output coupler reflectivity. In this Chapter, two lasers are developed – a Q-switched high peak power pump laser and a diamond Raman laser (DRL). Firstly the process of designing the pump laser is described (Section 3.1), where we start with assuming an output energy (based on the literature review) that is enough for pumping of the second Stokes DRL. From this energy requirement, we can then calculate the mode sizes of the pump laser cavity as well as Q-switch parameters. As it will be seen, the output average powers from the laser achieved in this Chapter are not rivaling any of the systems described in Section 1.4. This was expected since this system was only but a test subject for the large scale system developed with the Optical Research Center (ORC) in Southampton University (described in Chapter 4.1). The "large scale" system consisted of the same diamond Raman laser but with the difference that the pump laser was a high repetition rate, high average power Yb fiber master oscillator power amplifier (MOPA).

The DRL cavity is described later on in the chapter. It consisted of two mirrors and a diamond in between. The diamonds used in the Raman laser were provided by Element 6 and are briefly described in Section 3.4. Then the performance of the DRL is characterized in terms of energy, pulse durations and wavelength shift. The outcomes of this Chapter should be seen as a starting point for the fiber pumped DRL which

potentially could rival existing eye-safe technology.

3.1 Pump source at 1079 nm

Threshold for the second order Stokes diamond Raman laser oscillation was reported in the literature to be about $35 \frac{MW}{cm^2}$ [38, 61] peak intensity and about $10ns$ pulse duration at $1\mu m$ pump. As mentioned in [45, 82], the conversion efficiency in the external cavity Raman laser becomes independent of the pump intensities at above 4 times the threshold (conversion efficiency saturates at this level). Therefore, a pump laser that would deliver peak powers of at least 5 – 6 times the threshold (to be sufficiently above the 4 times the threshold requirement) of the DRL was designed which corresponded to the maximum output energy of $E \approx 0.5mJ$ assuming pump diameter of about $140\mu m$. This value of pumping spot size was found to be optimal by simulations will be presented in Section 3.5.3. The pump laser linewidth was controlled by putting an etalon in the cavity allowing for efficient Raman conversion. We now start with the design of the pump laser considering the gain medium, moving onto the cavity design and linewidth narrowing. Then the performance in a Q-switched regime is described.

3.1.1 Gain medium

The requirement for the eye-safety of the laser is for the emission wavelength to be above $1500nm$ as set out by the industrial partners and in [16]. There were a few reasons to utilize Nd:YAlO₃ (Nd:YAP) crystal as a gain medium instead of the more commonly used Nd:Y₃Al₅O₁₂ (Nd:YAG). Firstly, the differences in emission wavelengths [144]. The $1079nm$ emission wavelength of Nd:YAP results in the second Stokes Raman shifted wavelength of $1514nm$ when using diamond, as compared to $1485nm$ when using Nd:YAG with its highest emission cross-section corresponding to $1064nm$ emission. As presented in [145], the excited state lifetime at 1% doping level of Nd³⁺ in the Nd:YAP is about $\tau = 156\mu s$ and is $100\mu s$ shorter than Nd:YAG potentially making Nd:YAG a better choice for storing the energy for extraction in the Q-switch process (see Equation 1.10, where $N_p \propto \frac{1}{\tau}$), but since the emission cross-section at

$\lambda = 1064nm$ in Nd:YAG is $\sigma_e = 71 \times 10^{-20}cm^2$ compared to its $\sigma_e = 12 \times 10^{-20}cm^2$ at $\lambda = 1077.9nm$, it would be more complex to make the Nd:YAG laser oscillate at such longer wavelength. Usually this would be achieved through diffraction gratings or prisms. Therefore Nd:YAP was chosen as a gain material with the highest cross section of $\sigma_e = 46 \times 10^{-20}cm^2$ at $\lambda = 1079.6nm$. Nd:YAP and Nd:YAG have similar refractive indices (1.9 versus 1.8) and pumping wavelengths. The highest absorption coefficient for Nd:YAG is at $808nm$ with about $2nm$ bandwidth [40] which is usually similar to the pump laser diode's linewidth and $4.3cm^{-1}$ absorption coefficient at this wavelength. Typically $803nm$ laser diode is used for pumping of Nd:YAP and depending on its cut, the bandwidth can be up to $7nm$ [146] with $4.8cm^{-1}$ absorption coefficient[145, 147].

The differences in material characteristics can be explained by the difference in crystal structure, Nd:YAG being isotropic and Nd:YAP anisotropic making the latter emission wavelength and emission cross section dependent on the output polarisation [145]. In a nutshell, as outlined in [146], the overall performance of both Nd:YAG and Nd:YAP based lasers is very similar and the most important reason to chose Nd:YAP was the emission wavelength.

3.1.2 Cavity design

In this section, the laser mode diameters needed for a desired energy extraction in the Nd:YAP laser are calculated through rate equations analysis. After that, the ABCD method is used to match these diameters with the available mirrors and optics.

The output energy in an actively Q-switched laser is a function of the ratio between the maximum and a laser CW threshold inversion population[40]. As seen in Section 1.5.3 and as mentioned before, it was assumed that a pump pulse energy of $0.5mJ$ was required to sufficiently far above the Raman laser threshold.. Equation 1.10 was used to calculate the energy stored in the Nd:YAP laser. Assumption of the typical $\frac{N_i}{N_p} = 3$ [40] was made which corresponds to the energy utilization factor of $\eta_E = 0.9$. An output coupler of partial reflectivity $PR = 30\%$ was assumed in this calculation as one of the available mirrors. The plot of the Nd:YAP energy calculated using Equation 1.10 versus mode radius r ($A_b = r^2\pi$) is presented in Figure 3.1. It was found that

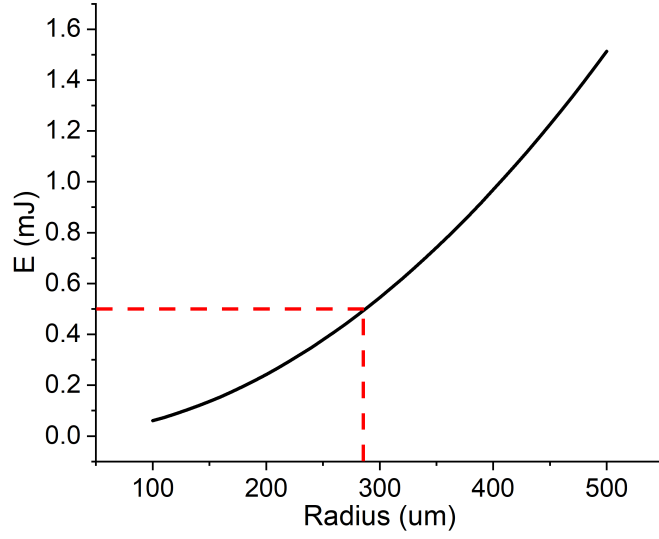


Figure 3.1: Simulation of the output energy in a Q-switched Nd:YAP laser versus mode radius in the gain medium. Parameters for Equation 1.10: $\eta_E = 0.9$, $\frac{N_i}{N_p} = 3$, $\gamma_2 = 0.7$.

reaching the energy of $E = 0.5mJ$, the fundamental mode diameter in the Nd:YAP crystal should be about $w = 580\mu m$.

Next, the ABCD matrix method was used to design and develop the laser cavity of a specified mode size with the help of the software(reZonator). The mode size could not be ideally matched with the calculated value because of the mirrors availability. The input coupler was $ROC = 758mm$ (highly reflective at laser emission wavelength) and the output coupler was $ROC = 1000mm$ (partially reflective at laser wavelength). The fundamental mode diameter at the Nd:YAP crystal in a laser cavity with the available mirrors was about $660\mu m$ diameter with a cavity length of about $230mm$ which was long enough to accomodate for all the needed optical elements. Additionally, the ABCD matrix method also included the acousto-optic modulator (AOM) crystal needed for the Q-switch operation. Mode propagation throughout the cavity is shown in Figure 3.2.

3.1.3 Experimental setup

Figure 3.3 shows a block diagram of the Nd:YAP laser that was developed. It has an "L" shaped cavity in order to allow for double side pumping. An available crystal,

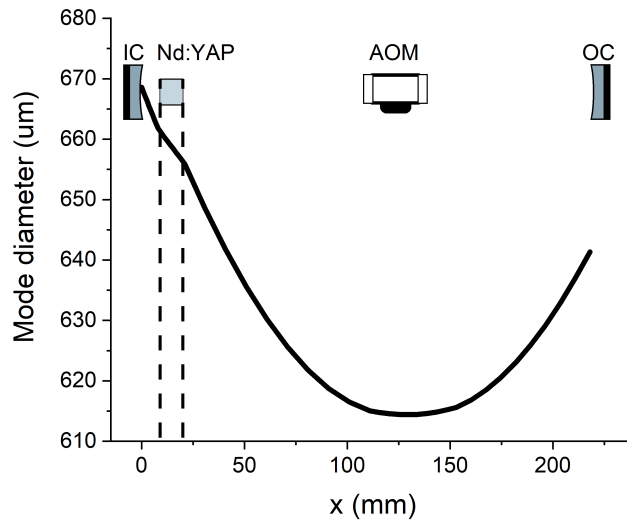


Figure 3.2: 1079 nm mode size radius in the Nd:YAP laser cavity.

Nd:YAP (Crytur) in the shape of a rod ($\phi 3 \times 5\text{mm}$) had a doping of 1at.%. The choice of the laser material was dictated by availability. Crystal was a-cut to maximize the emission cross-section at 1079nm [145]. The crystal was pumped by two fibre coupled laser diodes (LD) emitting at 808nm. The diodes were Coherent FAP-808-25C-800-B (LD1) and LIMO (LD2) connected to a pulsed current drivers (Newport ILX Lightwave and LIMO) synchronized together allowing for quasi-CW pumping reducing the thermal load on the crystal.

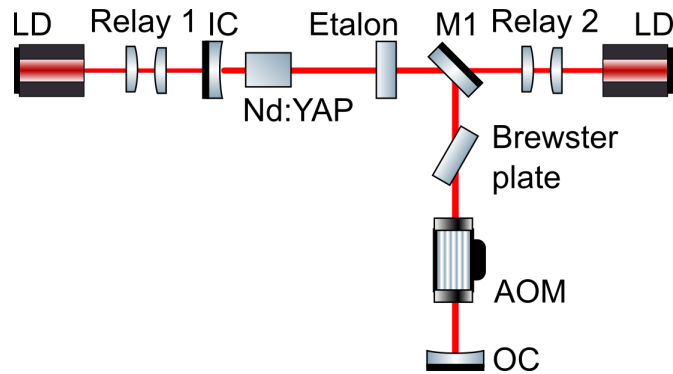


Figure 3.3: Developed Nd:YAP laser pump source. LD - laser diode, IC - input coupler, OC - output coupler, M1 - dichroic mirror, AOM - acousto-optical modulator, Relay 1,2 - a set of lenses for resizing the pump beam focal spot.

In CW mode, LD1 and LD2 power current curves had gradients of $0.98 \frac{W}{A}$ and $0.85 \frac{W}{A}$ respectively. While pumping the Nd:YAP laser for the purpose of Q-switching, the diodes operated at a 2% duty cycle resulting in the total of $0.25W$ average quasi CW power, $20Hz$ repetition rate with about $0.47ms$ pump on time. The repetition rate and duty cycle were dictated by the performance in the Q-switch regime described in later Sections. Increasing the repetition rate above $20Hz$ or operating at the higher duty cycle resulted in the output energy falling off most likely due to the thermal roll-off. Both of the LD output beams were focused into the gain material to match the cavity mode sizes with the lens relays. For efficient pumping, the pump focus spot should be about the laser mode size[40] following Equation 3.1 where the average pumping rate over a laser mode field distribution $\langle R_p \rangle$ is proportional to the inverse of the laser mode radius w_o and pump radius w_p over a gain medium of length l . It also has to be noted, that reducing the pump radius at the focus below a certain point does not increase the pump rate averaged over the length of the rod.

$$\langle R_p \rangle \propto \frac{2}{\pi (w_o^2 + w_p^2) l} \quad (3.1)$$

It was assumed here, that the spot sizes do not change over the distance l which for real divergent beams is not true - therefore, decreasing the pump spot radius does not necessarily increase the pump rate since the divergence increases for tightly focused beams[40]. In this case, a calculation of the average beam size over the gain medium should be used, presented e.g. in [148]. As mentioned in [40] a practical approach is to match pump and laser modes as closely as possible. It is also worth mentioning, that if the pump size is much larger than the fundamental laser mode size, it is possible to pump higher order modes and decrease the output beam quality, on the other hand, pumping with too small spot size can increase the risk of crystal or coatings damage.

The matching of the pump and laser modes was achieved by two lens relays as seen on Figure 3.3. Each relay conditioned a beam of each of the LDs and consisted of two plano convex lenses, the first of which (focal length f_1) collimated the LD light coming

out of the optical fiber (output diameter d_0) and the second of which (focal length f_2) focused the beam into the Nd:YAP crystal to a spot $d_1 = \frac{f_2}{f_1}d_0$. As the focused beam spot diameter is determined by the ratio of the two focal lengths of the lenses, the matching is limited by the availability of the lenses and it was not perfectly accurate. On the other hand it was found that despite this, the performance of the laser met the requirements for the generated energy and no further improvements were needed.

The first lens relay ($f_1 = 63mm$, $f_2 = 50mm$) focused the LD1 beam from $800\mu m$ which was a fibre output core diameter, to a calculated value of $640\mu m$ diameter in the crystal.

The second lens relay ($f_1 = 35mm$, $f_2 = 175mm$) expanded the LD2 beam from $200\mu m$ fibre core diameter to measured value of $850\mu m$ diameter. Therefore the first pump diode spot diameter was about $20\mu m$ smaller than the laser mode in Nd:YAP (calculated) and the second laser diode was about $200\mu m$ larger (as measured).

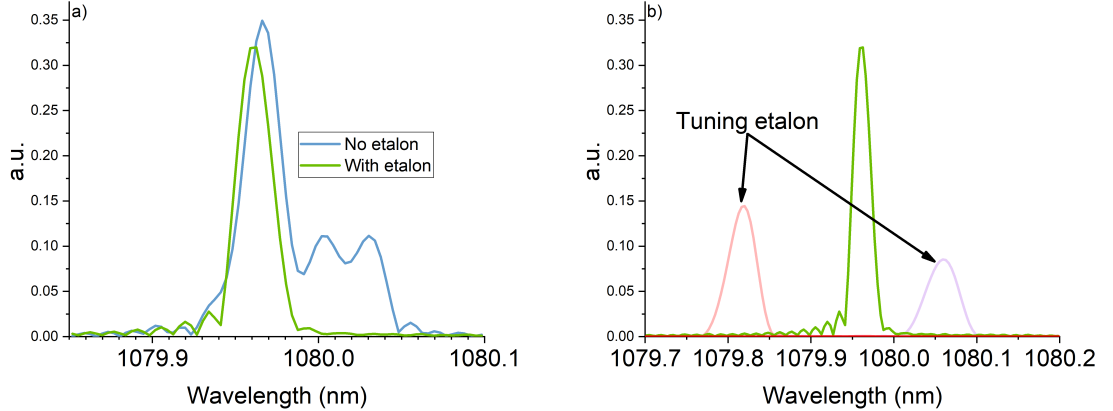
The input coupler was highly transmissive at the pump wavelength and highly reflective at laser emission wavelength and the output coupler was partially reflective at the laser emission wavelength. The dichroic mirror M1 was highly reflective at a $1079nm$ and transparent at LD wavelengths to allow for the side pumping. A glass etalon ($2mm$) and a glass Brewster plate were used for wavelength and polarization control. An Acousto-optic modulator (AOM) was used to control the Q-factor of the cavity in the Q-switched pulsed operation. The following sections will focus on how these optical elements in the cavity impact the laser performance and its emission spectrum.

3.1.4 Spectrum and wavelength stabilization

Firstly, the output spectrum of the Nd:YAP laser was analyzed in a quasi-CW regime and turned off AOM. The LD1 pump was set to 17A, which was equal to about 1W of quasi-CW average power, 50Hz repetition rate and 1.5ms on time. It resulted in about 120mW of average power in the Nd:YAP emission. These parameters were chosen to fall into the operating range of the optical spectrum analyser (OSA 205C, Thorlabs) in terms of the signal duration. The chosen output coupler of the Nd:YAP laser had

a partial reflectivity $PR = 70\%$ since this was the optimum output coupler for the Q-switching operation (described later in Section 3.2.1). As a reference, the optimum parameters for the Q-switching operation were $20Hz$ repetition rate and $0.47ms$ pump on time but these were outside of the OSA operating range. The Q-switched spectrum of the Nd:YAP is presented in Section 3.2.2.

The OSA had an $0.02nm$ resolution at $1\mu m$ wavelength. The cavity consisted of the same elements as seen on Figure 3.3. The glass etalon of a length $L = 1.3mm$ placed in the cavity acted as a wavelength filter due to its own mode spacing (free spectral range) of $FSR = \frac{c}{2L} = 74.7GHz$ which was about $\Delta\lambda = 0.29nm$ at $\lambda = 1080nm$. Green curve in Figure 3.4a shows the Nd:YAP emission at the center wavelength of $1079.96nm$ with the linewidth of a Gaussian fit of $FWHM = 0.020nm \pm 0.001$ which is about the OSA's resolution at $1079nm$. A blue curve in Figure 3.4a shows the output spectrum without the etalon in the cavity. It can be seen that this element narrows the linewidth as well as clears additional features in the spectrum which could have resulted from either multimode operation or wavelength instabilities seen as a time averaged broadened spectrum. The rotation of the etalon was found to tune the output wavelength of the laser over about $0.3nm$ as seen on Figure 3.4b. The gain bandwidth of around the $1080nm$ is about couple nm wide as described in [149].



(a) Effects of linewidth narrowing of the etalon in CW regime.

(b) Nd:YAP wavelength tuning by etalon in CW regime.

Figure 3.4: Nd:YAP laser output linewidth narrowing and tuning through the etalon.

3.2 Pump source at 1079 nm Q-switched operation

Raman conversion is a non-linear process requiring high peak powers[39], hence the pump laser is usually operated in the pulsed mode since the emitted peak power of the laser is then $P_{peak} \propto \frac{P_{avg}}{f_{rep}\Delta t}$ and it can be already seen that the shorter the pulse width Δt and the lower the repetition rate f_{rep} , the higher the peak power. For short pulse generation the Q-switch method is used and is described in detail in 1.5.3, whilst here we will focus on the practical implementation. The switching of the Q factor of the laser cavity was achieved using an acousto-optic modulator (AOM - Stallion, Gooch and Housego)[40] which periodically diffracted the intracavity laser field increasing drastically the lasing threshold. The diffraction efficiency (DE) could be adjusted using the RF power from the RF driver [150]. The higher the DE, the higher the lasing threshold when the AOM is operating but if the DE is too low, the laser could always be above the threshold and the Q-switching action would not be achieved. The angle of diffraction is dependent on the frequency of the RF power from the driver. If this frequency is too low, the diffracted beam could potentially contribute to lasing and reduce the Q-switching efficiency. Another parameter important to the AOM operation is an active aperture which indicates the area over which the acoustic wave interacts with the laser beam to diffract it. This aperture is smaller than the crystal itself and is determined by the size of the acoustic transducer. The AOM driver available in the experiment had an operating frequency of $24MHz$ and the AOM crystal had an active aperture of $8mm$. Figure 3.5 is a reminder of the Q-switch operation. The crystal in the modulator was water cooled and made of fused silica, AR coated at $1064nm$ with damage threshold of $> 1\frac{GW}{cm^2}$. Firstly, the RF power is supplied to the AOM to prevent the laser from lasing (low Q factor by diffracting the laser photons). Then the pump laser is turned on at time $t = 0$ initiating the population inversion N_i growth in the laser gain medium. At a certain population inversion level, the laser gain reaches the threshold of CW emission (in a high Q-factor state) but because the Q-factor of the cavity is low, the losses of the cavity are actually higher than the gain and the laser does not emit. The population inversion then approaches an asymptotic maximum determined by the

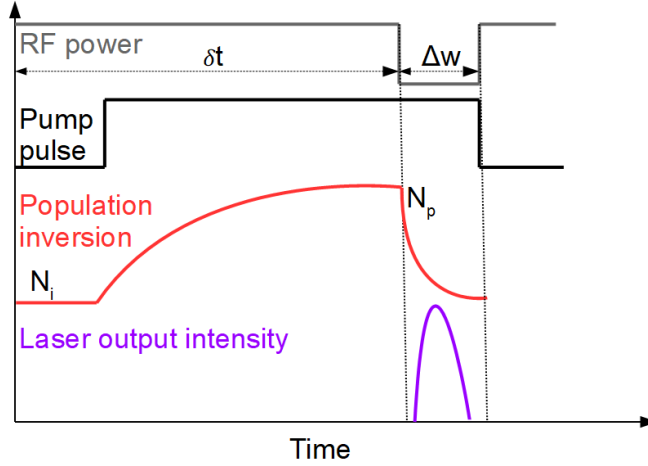


Figure 3.5: Q-switching setup for Nd:YAP laser. The schematic represents one pulse generated in a loop. N_i - initial population inversion before AOM opening, N_p - population inversion at the CW operation threshold for high Q state.

product of pump rate and the photon excited state lifetime $N_{i,max} = R_p\tau$ [40]. After a delay of δt controlled by the function generator, the Q-factor of the cavity is turned high by switching off the AOM for a time window of Δw , allowing the energy stored in the gain medium to be released in a form of a high energy pulse. The amount of energy in this pulse is determined by Equation 1.10 in which $\frac{N_i}{N_p} = 3$ can be taken as a ratio of the LD current needed to reach the threshold for the pulsed operation to the current needed to reach threshold for the CW operation. It was found that the Nd:YAP laser threshold in CW regime was at a 12A of LD current and about 35A in Q-switched case which matched the typical[40] ratio of $\frac{N_i}{N_p} = 3$, taken into account for the cavity design in Section 3.5.2.

The procedure of optimizing for the high energy output involves finding right parameters for the trigger delay δt and width of the off window Δw . For the long trigger delays, the population inversion can reach the lasing threshold for even a low Q factors which results in a laser free-running operation and therefore extracting part of the energy from the gain medium. This was observed as a series of spikes in the laser output before the Q-switched high energy pulse and although the overall average power increases, this additional energy is not a part of the high energy pulse and it can contribute to the error in the Raman laser conversion efficiency analysis. On the other

hand, if the trigger delay is made too short, the $\frac{N_i}{N_p}$ ratio is low and limits the output energy.

The population inversion evolution N in a gain medium in the absence of stimulated emission as in the case of low Q cavity can be calculated using Equation 3.2[40]

$$\frac{dN}{dt} = R_p - \frac{N}{\tau} \quad (3.2)$$

where the term R_p is the pump rate and τ is an excited laser level lifetime. For a $P_{abs} = 26W$ absorbed pump average power in the gain medium (average total pump power in the Q-switching pumping cycle), absorbed photon energy ν_p and a pumping volume $V = 3.5mm^3$ (which was about the volume designed for the Nd:YAP pumping), the pump rate was $R_p = \frac{P_{abs}}{h\nu_p\pi V} = 2.7 \times 10^{34} \frac{1}{m^3s}$. Figure 3.6 shows the evolution in time of the normalized population inversion calculated with the Equation 3.2 which reaches the maximum at around $600\mu s$. The optimal performance of the laser was found when this time was reduced to $420\mu m$ since after increasing this time further some CW emission was observed in the output as the laser reached the threshold for the low Q factor. Pumping for shorter times decreased the output energy in the pulse as the population inversion was lower.

The width of the q-switch window $\Delta w = 188ns$ was chosen to maximize the output energy of the laser. A window that is too short will clip the tail of the output pulse reducing its energy and by decreasing it further, it will introduce cavity losses during the Q-switch pulse buildup and reduce the output energy, on the other hand if the window is too long, some spikes may occur after the main pulse of the laser indicating laser reaching a free running threshold. This situation is described in [40] as the slow switching of the cavity losses (and not switching them at all in a case of a long Δw is certainly the case) can lead to multi pulsing.

Figure 3.7a shows the output pulse of the laser which was about $20ns$ long of FWHM width. The used pump combined average power was about $0.22W$ average power with the $420\mu s$ on time and $20Hz$ operation. Mode beating, similar to [151], was observed in the output pulse and the distance between the peaks was $1.75ns$ which corresponds to

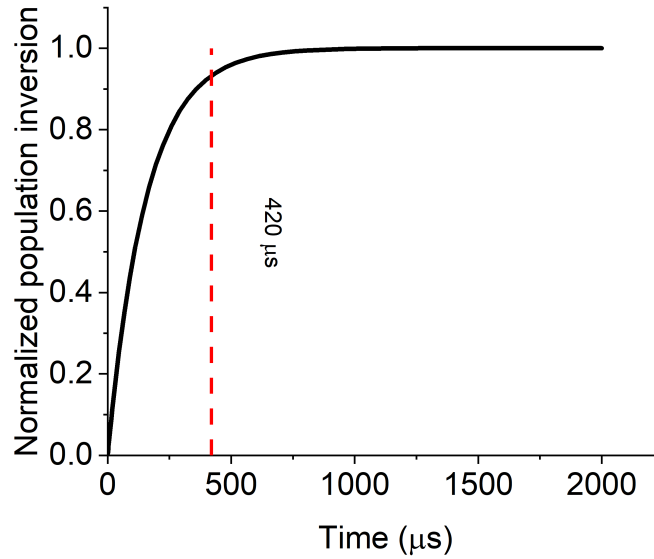


Figure 3.6: Evolution of the population inversion in the Nd:YAP laser. Normalization to the maximum population inversion.

576MHz beat frequency. Figure 3.7b shows the Fourier transform of the output pulse. The intermode beat frequency for a 262mm cavity of the Nd:YAP laser was 576MHz which corresponds to a 1.75ns period which confirmed intermode beating in this laser. The secondary peak at 1.17GHz is a second harmonic of the 576MHz peak. This means that there are at least two adjacent longitudinal modes oscillating in the cavity. The pulse duration as well as the output energy depended on the used pump power and this is described in the next section together with the output coupler optimization.

3.2.1 Performance and output coupler optimization

The output coupler for the Nd:YAP laser was chosen from the available mirrors: 70% and 80% reflectivity. The results are summarized in the Table 3.1. The 70% reflectivity mirror was chosen based on the highest output energy. The pump on-time in the 20Hz case was equal to the trigger delay time δt (plus RF off time δw) and the maximum achieved output energy was 0.55mJ. In the 50Hz case, the output energy was 0.46mJ and not as high as in the 20Hz which was most likely caused by shorter pump on time (ref. Table 3.1). Increasing the pump on-time resulted only in decreasing the Nd:YAP output energy possibly due to the thermal load so the repetition rate of

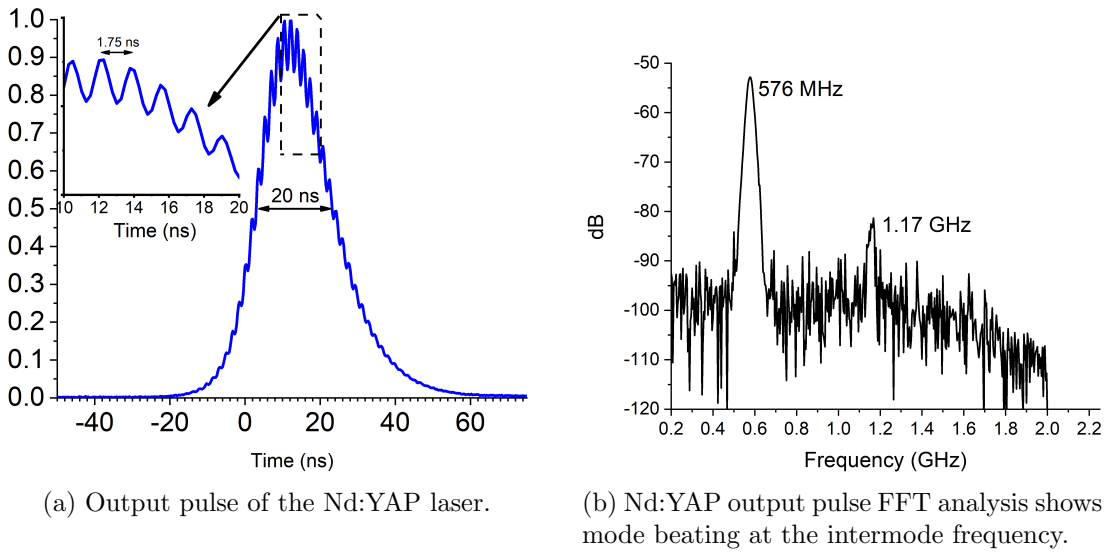


Figure 3.7: Nd:YAP laser output pulse analysis.

operation was chosen to be 20Hz . As a proof of concept laser, the repetition rate was not the most important factor and the main goal was to produce as much of energy as possible per single output pulse which as described in the beginning of this Chapter would be a few times above the Raman laser threshold energy. The investigation of the high power and high repetition rate is described in Chapter 4 where Yb fiber MOPA is used as a pump laser.

| Output coupler [%] | Energy [mJ] | Pulse length [ns] | Trigger delay [μs] | Repetition rate [Hz] |
|--------------------|-------------|-------------------|---------------------------------|----------------------|
| 70 | 0.55 | 21 | 420 | 20 |
| 70 | 0.46 | 21 | 276 | 50 |
| 80 | 0.44 | 21 | 184 | 50 |

Table 3.1: Optimization of the output coupler in Nd:YAP laser

Figure 3.8 shows an output pulse energy and pulse duration as a function of LDs quasi-CW (2% duty cycle) average power. The operating point was set to be 25A for LD1 and 20A for LD2 which corresponds to about 0.23W of quasi-CW average power and about $E = 0.4\text{mJ}$ output energy at $\lambda = 1080\text{nm}$ which gave enough energy to use this laser as a proof of concept system for diamond Raman laser pumping. It was possible to generate more energy, but it was observed, that the coatings on the Nd:YAP

were damaged. The graph shows that the roll-off point for this laser, most likely due to thermal effects was around $0.24W$ average power. The pulse duration also decreased as the pump power increased since the pulse duration also depends on the maximum population inversion [40, 152] and is limited usually by the cavity decay time. The pulse duration in Figure 3.8 reaches a steady value for a certain pump power. As mentioned before, the rising edge of the pulse is determined by the gain in the laser medium and the trailing edge by the cavity decay time. By increasing the pump power, the $\frac{N_i}{N_p}$ ratio increases and the $\Delta\tau_p$ from Equation 1.11 tends to cavity decay time τ_c which depends on the output coupling, losses and length of the laser cavity.

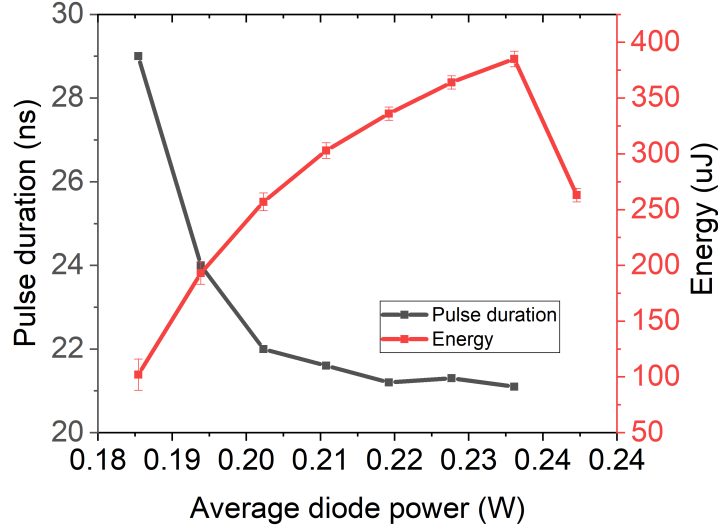


Figure 3.8: Pulse energy and duration as function of pump power.

3.2.2 Output spectrum

The pulsed regime spectrum seen in Figure 3.9 was measured with about $0.5W$ of quasi-CW average power at $50Hz$ repetition rate. The laser repetition rate was increased from $20Hz$ because the OSA measurements at lower repetition rates are difficult due to the artifacts in the output spectra and low sensitivity[153]. The resolution of the OSA at $1080nm$ was about $0.03nm$. The center wavelength was measured to be $1079.6nm$ and the linewidth was limited by the resolution and was $0.03nm$. The achieved wavelength of operation of the Nd:YAP laser operating in the pulsed regime

allowed for the second Stokes conversion in diamond to reach $1.5\mu\text{m}$ making it a suitable pump source for the eye-safe laser system.

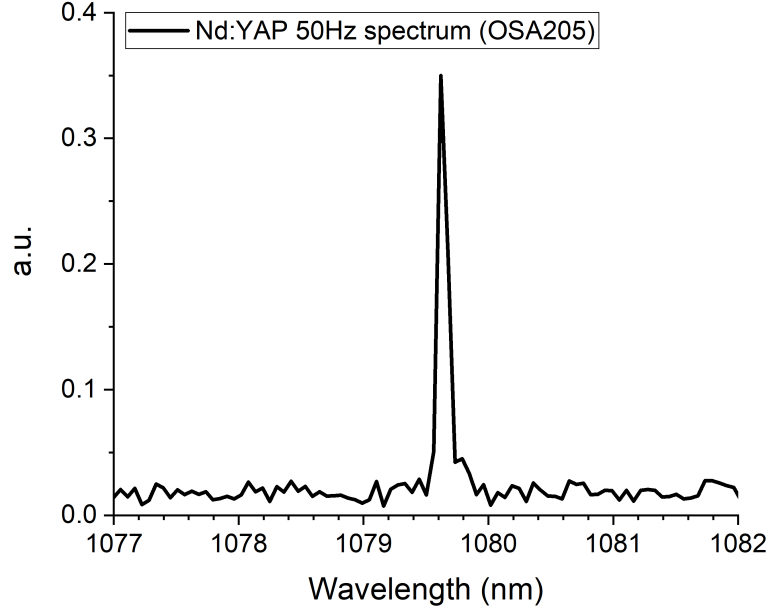


Figure 3.9: Nd:YAP spectrum in pulsed regime.

3.2.3 Beam quality

The method for the measurement of the laser output beam quality is described in Section 1.2.1 and [154]. Here, the output beam of the Nd:YAP was focused by a $f = 100\text{mm}$ lens to a spot and a series of beam profiles were measured through this focus. Figure 3.10 shows the beam diameter versus propagation distance with the $z = 0$ representing the focus position. Each point represents an average of the beam diameter of 100 frames taken with the CCD camera. Each single measurement had an error of about 10% therefore after averaging, the error is negligible. The resulting solid curve is a fit to the Equation 1.2 and parameters: $A = 2.39 \pm 0.41 \times 10^{-8}\text{m}$, $B = 7.95 \pm 2.85 \times 10^{-7}\text{m}$, $C = 1.15 \pm 0.3 \times 10^{-4}\text{m}$ with 95% confidence bounds and R-Square value of 0.97. The beam quality M^2 parameter was about $M^2 = 1.2 \pm 0.2$ calculated with the Equation 1.3. The Rayleigh range (range over which the beam expands by the factor of $\sqrt{2}$) for this beam is about 14mm which was much longer than the diamond length in the Raman laser cavity. This simplified the pump rate calculations for the

Raman laser since Equation 3.1 assumed a non diverging beam.

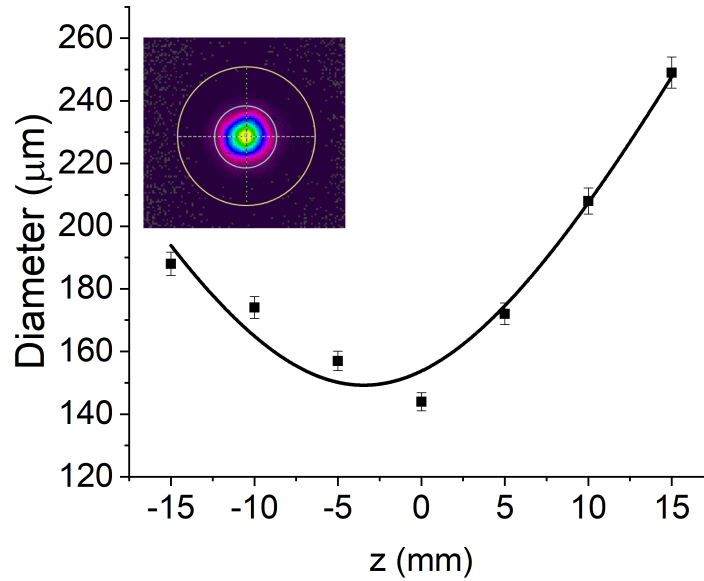


Figure 3.10: Beam diameter fit for the beam quality measurement. Inset shows a beam at the focus. R-Square value of the fit 0.97.

3.3 Summary

The first part of this Chapter concludes with a summary of the achieved parameters of the Nd:YAP laser presented in Table 3.2. The maximum energy in the following table represents the energy available for DRL pumping and is lower than the one presented in Table 3.1 due to (i) degradation of the AR coatings on the Nd:YAP crystal over time and (ii) the transmission function of the DRL conditioning optical system (ref. Section 3.5.1). It is still about 4 times above the expected second Stokes threshold [38]. The output polarization of the laser was linear and could be rotated with the external half-wave plate to adjust for the polarization with the maximum Raman gain in diamond as mentioned previously in Equation 1.7.

| Wavelength | Linewidth | Pulse energy | Pulse duration | Repetition rate | M2 |
|------------|-----------|--------------|----------------|-----------------|-----------|
| 1079nm | < 0.3nm | 0.42mJ | 21ns | 20Hz | 1.2 ± 0.2 |

Table 3.2: Parameter of the developed Nd:YAP laser.

3.4 Research grade diamond samples

3.4.1 Diamond samples

Before moving on to characterizing the diamond Raman laser, a brief description of the Element 6 diamond samples is provided. There were five $4 \times 2 \times 2mm$ samples and one $7 \times 2 \times 2mm$ sample. Figure 3.11 shows the orientation of the sample where the laser beam propagation was along a $\langle 110 \rangle$ crystallographic direction with its polarization aligned with a $\langle 111 \rangle$ direction. The specification for the absorption coefficient of the crystals was $< 0.005cm^{-1}$ at $1064nm$ wavelength. Birefringence can cause polarisation changes which can result in losses if there is some polarisation dependent loss in the cavity. It is measured by the difference in the refractive index Δn for the two orthogonal polarizations. The birefringence can be assessed by using e.g. cross-polarizer method[155] where a polarized light is passed through a medium and later is analyzed through a polarizer which is orthogonally oriented w.r.t. to the input light polarization. In a case of a medium with no birefringence, the light should be completely blocked by the second polarizer. Figure 3.12 shows a measurement (supplied by Element 6) of the birefringence of the crystals. It can be seen, that the image does not show any light which means that there is no significant birefringence present in the crystal. The specifications of the birefringence for the samples was $\Delta n = 2 \times 10^{-5}$. Such ultra low birefringent material is essential for the efficient Raman laser: Equation 1.7 shows that the Raman gain is dependent on direction of the pump and Raman field vectors and if these become depolarized due to the birefringence, the gain can be reduced.

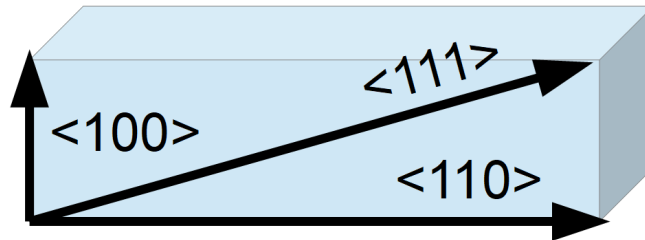


Figure 3.11: Crystallographic directions of the diamond samples.

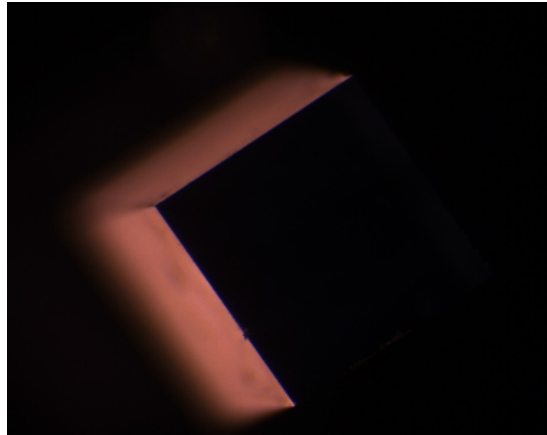


Figure 3.12: Cross-polarization measurement of the birefringence in the diamond samples.

3.4.2 Diamond coatings

The diamonds were coated with anti-reflective (AR) coatings at three wavelengths of interest. The lowest reflectivity was at $1.5\mu m$ and $1.2\mu m$ with about 0.3% and 0.5% respectively and about 3% at $1\mu m$. Figure 3.13 shows a measurement performed by the coating company Lambda Research Optics, Inc.

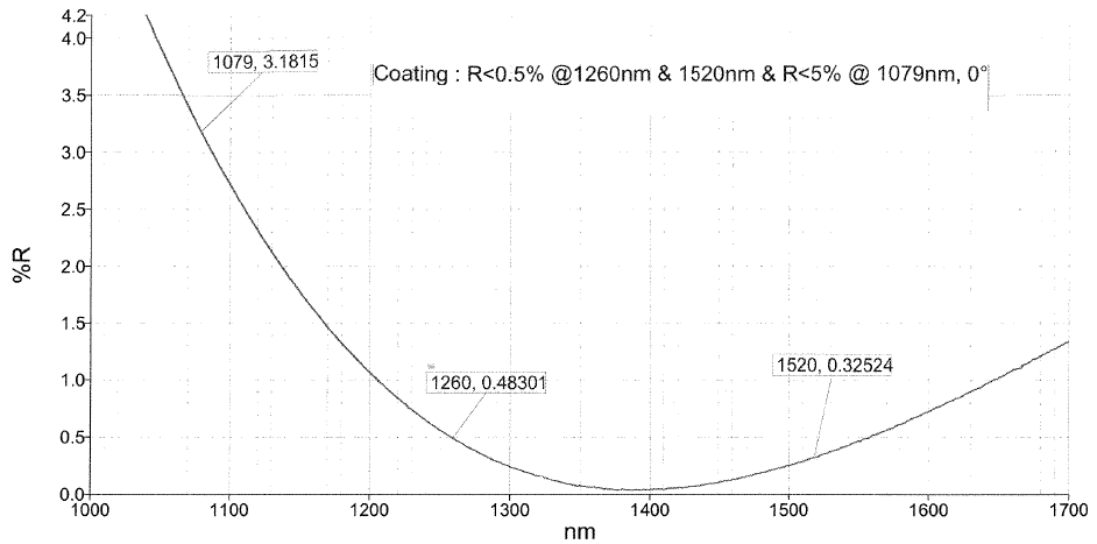


Figure 3.13: Simulation of the reflectivity spectrum of anti-reflection coatings on diamond. Courtesy of Lambda Research Optics, Inc.

3.5 Diamond Raman Laser proof of concept

The diamond Raman laser (DRL) presented in this section was a second Stokes Raman laser which means that the pump wavelength is shifted by Raman shift in diamond from $1\mu\text{m}$ twice to reach eye-safe wavelengths. The DRL consisted of pump conditioning optics (power attenuator, polarization control and focusing) and the DRL cavity itself - an input coupler, diamond crystal and an output coupler.

Figure 3.14 shows a DRL cavity with a piece of diamond in between two mirrors. The diamond is positioned on a micro adjustable XYZ stage which can also tilt allowing for precise alignment.

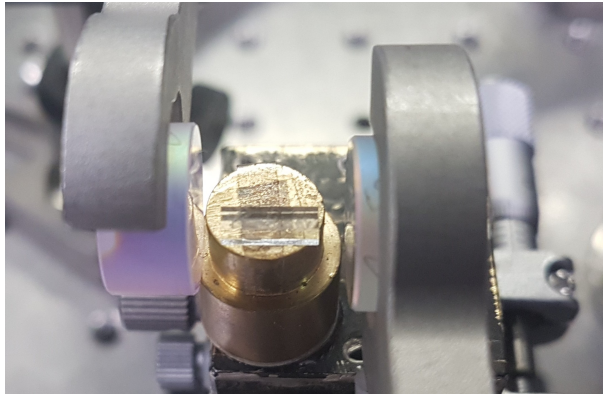


Figure 3.14: Diamond positioned in between input and output coupler makes a DRL cavity.

3.5.1 Beam conditioning

Additional optical elements were used for power, polarization control and for focusing the pump beam. This allowed for the characterization of the DRL performance depending on the input pump beam conditions.

Figure 3.15 shows the conditioning optics elements. The isolator (Electro-Optics Technology - PAVOS, 33dB isolation) prevented the back reflected light affecting the Nd:YAP performance. Due to the chosen reflective coatings of the DRL output coupler, the pump was double passed in the Raman cavity and removing the isolator substantially limited the Nd:YAP laser performance. The attenuator consisted of a rotating

Chapter 3. Diamond Raman Laser prototype

zero-order halfwave plate (HWP, Thorlabs) anti-reflection (AR) coated at $1080nm$ and a Polarizing Beamsplitter (PBS, Thorlabs). By rotating the HWP it was possible to control the intensity of light being passed through the PBS. An additional HWP was added after the attenuator to control the polarization of the pump beam since the Raman gain is dependent on the pump polarization [81]. The focusing lens was a spherical plano-convex lens (Thorlabs, C AR coating $1050nm - 1700nm$) and was used to focus the pump beam into a desired diameter. The lens was positioned on an XYZ stage allowing for shifting the focal spot along the optical axis which was found to be the most important factor in the alignment. An aperture was added after the focusing lens as well to aid with the DRL alignment process. The reflections from the DRL (couplers and diamond's surfaces) were visible with an IR viewer on the aperture and can be used as an indication if all the reflecting surfaces are positioned in parallel to each other (the reflections are going back the same optical path). The Raman cavity itself consisted of the input coupler, diamond crystal and an output coupler.

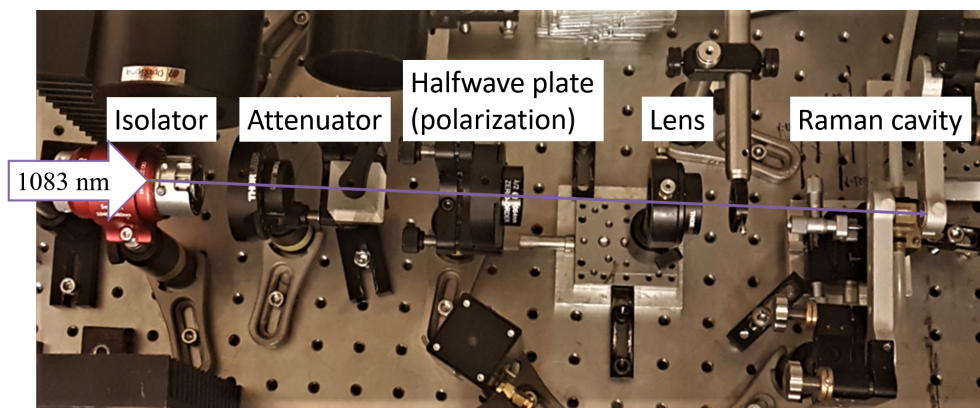


Figure 3.15: Conditioning optics for the DRL.

3.5.2 Diamond Raman laser cavity design

This section presents an analysis of the DRL mode sizes for the first and second Stokes. The laser mode sizes were important for the simulation of the DRL efficiency in Section 3.5.3, where the pump spot diameter and output coupler partial reflectivity were optimized for the following ABCD matrix calculated laser modes.

Available mirrors for input and output couplers had radii of curvature (ROC) 50, 100, 150mm and plane. Figure 3.16 shows the first and second Stokes laser modes diameter variation in the DRL cavity for a plane input coupler, 4mm diamond (using a 7mm diamond does not increase the mode diameter significantly) and a $ROC = 50mm$ output coupler generated by the reZonator software [139]. The $ROC = 50mm$ output coupler provided the smallest mode size over the diamond's length ($187\mu m$ at $1261nm$ and $202\mu m$ at $1516nm$). The mirrors in the DRL cavity were positioned as close as

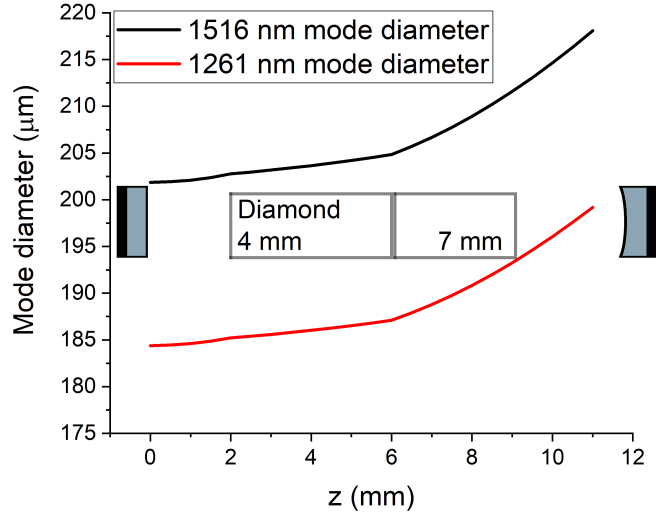


Figure 3.16: Mode size propagation along the cavity axis, starting at $z = 0mm$ - the input coupler. The diamonds represent positions of the diamond samples (4mm and 7mm).

possible to the diamond (as also indicated in [38]) which minimized the mode radius of the second Stokes and it varied from $202\mu m$ to $218\mu m$ over the crystal length. The full length of the cavity was about 1.1cm. This allowed for matching of the pump and DRL laser modes over the diamond length which simplified the model as the overlap of the pump and laser modes shown in Equation 3.1 assumes low-diverging beams.

Figure 3.17 shows the stability parameter (ref. Section 2.3) and laser mode size on the diamond's input face versus the distance between the diamond surface (closer to the output coupler) and an output coupler. The mode size changes from $150\mu m$ to about $210\mu m$ over the stability range. Changing the output coupler ROC to 100mm further increased the mode diameter by $80\mu m$. The mode diameter used in the exper-

iment is also indicated in the Figure 3.17 for reference and we will see in the Section 3.5.3 that it was chosen to best match the pump spot size. It has to be added that a similar mode size could have been achieved by increasing the distance between the diamond and the output coupler to 40mm but the lasing action was difficult to achieve, possibly due to the increased pump beam size on the second pass through the DRL cavity. The diameter of the pump beam from the Nd:YAP laser at the center of the diamond after reflecting off the $ROC = 50\text{mm}$ output coupler positioned 8mm away from the diamond output surface was estimated to be about $170\mu\text{m}$ diameter versus $186\mu\text{m}$ when the output coupler was positioned 40mm from the diamond surface.

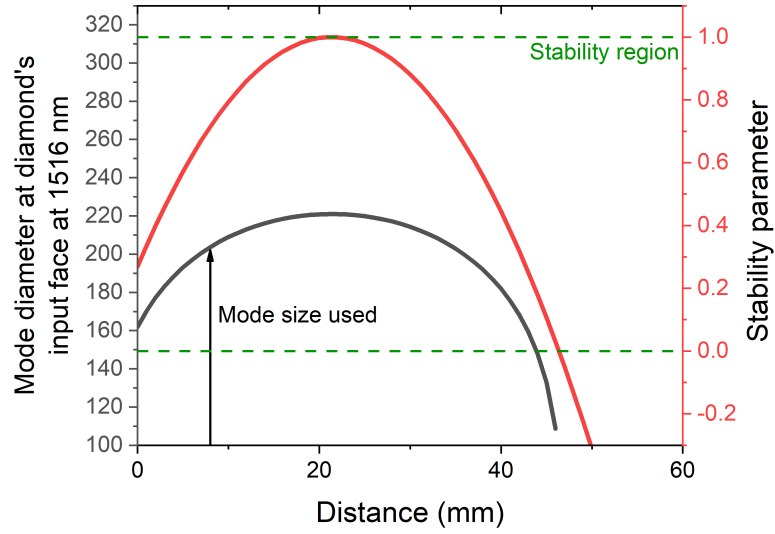


Figure 3.17: Stability and mode diameter of 1516nm for a DRL cavity (plane input coupler and 50mm output coupler) versus the distance between the diamond surface and the output coupler.

3.5.3 Pump spot diameter and output coupler optimization

This section shows the optimization of the pumping spot size and the partial reflectivity of the output coupler (OC PR) of the DRL as two main variables. The Model presented in Chapter 2 was used to simulate the conversion efficiency of the DRL. Table 3.3 shows the parameters used in the model. The DRL laser mode diameters for this simulation were as calculated by the ABCD matrix method for a 2cm long cavity with a 4mm diamond: $d_{first\ Stokes} = 187\mu\text{m}$, $d_{second\ Stokes} = 202\mu\text{m}$. Diamond

was assumed to have an absorption coefficient of $\alpha = 0.003\text{cm}^{-1}$ at pump and Stokes wavelengths. The input coupler had anti-reflective (AR) coatings on a side facing away from the diamond to transmit the pump light ($< 2\%$ at 1080nm) and the side facing diamond was highly reflective at Stokes wavelengths ($> 99.9\%$ at $1.2\mu\text{m}$ and $1.5\mu\text{m}$) as well as AR at the pump wavelength. The output coupler was highly reflective at pump wavelength ($> 99.9\%$ to allow for a double pass operation) and first Stokes-shifted wavelength ($> 99.9\%$ at $1.2\mu\text{m}$). It was also partially reflective (15%, 30% or 60%) at the second Stokes wavelength of $1.5\mu\text{m}$. Raman gain coefficients reported in [75] at $1.064\mu\text{m}$ was $g_0 = 17\frac{\text{cm}}{\text{GW}}$ and $g_1 = 7.6\frac{\text{cm}}{\text{GW}}$ at $1.28\mu\text{m}$. The gain coefficients were first adjusted to the experimental wavelengths by taking the gain at fundamental wavelength and multiplying it by the ratio of the wavelengths as shown in [38]. The pump wavelength gain coefficient: $g_{1079} = \frac{1064}{1079}g_{1064} = 16.7\frac{\text{cm}}{\text{GW}}$ and first Stokes gain coefficient $g_{1264} = \frac{1280}{1264}g_{1280} = 7.7\frac{\text{cm}}{\text{GW}}$. These values were further adjusted to match the experimental results in Section 3.6.3 by multiplying the gain factors by a constant $k = 0.9$ resulting in the so called effective gain coefficient that takes into account mismatch in the pump and Stokes beams overlap and first Stokes photons scattering not contributing to the laser mode. The gain coefficients used in this simulation were therefore $g_0 = 15.3\frac{\text{cm}}{\text{GW}}$ and $g_1 = 6.8\frac{\text{cm}}{\text{GW}}$.

| | | | | |
|------------------------------------|------------------------------------|-------------------------------------|-----------------------------|-----------------------|
| $g_0[\frac{\text{cm}}{\text{GW}}]$ | $g_1[\frac{\text{cm}}{\text{GW}}]$ | Pump pulse energy [μJ] | $d_1[\mu\text{m}]$ | $d_2[\mu\text{m}]$ |
| 15.3 | 6.8 | 400 | 187 | 202 |
| $l_r[\text{mm}]$ | K_{sp} | R_{12} (1st Stokes IC) | R_{22} (2nd Stokes IC) | R_{01} (pump OC) |
| 4 | 10^{-9} | 0.99 | 0.99 | 0.99 |
| R_{02} (pump IC) | R_{11} (1st Stokes OC) | R_{21} (2nd Stokes OC) | ROC OC [mm] | ROC IC [mm] |
| 0 | 0.99 | variable | 50 | plane |

Table 3.3: Parameters for the model used for pump spot optimization. d_i are diameters of i order Stokes laser modes ($i = 0$ for pump wavelength), plane input coupler.

Keeping the mode sizes constant, optimum performance can be found by varying the pump spot diameter and OC PR parameters and plotting the conversion efficiency of the second Stokes output in a "heat map" plot which is presented in Figure 3.18.

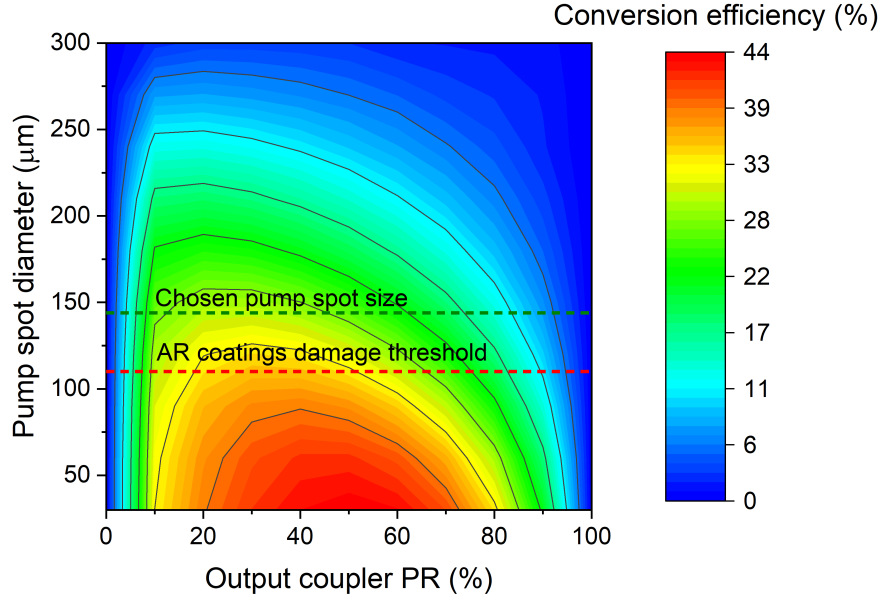


Figure 3.18: Simulation of the DRL performance versus pump spot diameter and output coupler partial reflectivity at a pump energy $E = 400\mu J$. Indicated are the damage threshold for a pump double pass $10\frac{J}{cm^2}$ [8] and chosen pump spot diameter.

Figure 3.18 shows the conversion efficiency of the DRL at the second Stokes wavelength versus pump spot diameter and OC PR of the DRL cavity. It can be seen, that for the decreasing pump spot diameter (increasing the intensity of the pump) the conversion efficiency of the DRL increases towards maximum at about $25\mu m$ pump spot diameter and about 50% OC PR. The damage threshold of the AR coatings was observed at about $10\frac{J}{cm^2}$ [8] corresponding to the pump spot diameter of $110\mu m$ indicated by the "AR damage threshold" dashed line in the Figure 3.18. The pump spot diameter chosen was $140\mu m$ for the experiment was sufficiently larger not to induce damage. The maximum simulated conversion efficiency for a pump spot diameter of $140\mu m$ was about 33% for an OC PR of about 30%.

Figure 3.18 also shows that the second Stokes conversion efficiency for the pump spot size of $50\mu m$ reaches maximum between 30% and 60% OC PR and falls off for both higher and lower PR. This is consistent with the findings in [38], where a very similar laser was presented (second Stokes laser, pumped by $1.064\mu m$ laser) and where the higher efficiency was achieved when using a low output coupler reflectivity at second

Stokes wavelength. For the $PR = 0\%$, there is no feedback to start the lasing action and only spontaneous scattering is present in the output of the laser. For $PR = 100\%$ all the energy is contained within the cavity and no second Stokes signal outputs from the laser.

A preference of the low versus high partial reflectivity of an output coupler for the DRL is presented in a discussion in [156], where the analysis of the performance of the odd and even order Raman laser is shown. Burgoyne et.al show, that this is due to the amount of residual power of the not fully depleted pump. The higher the depletion, the higher the efficiency of the Raman conversion as seen explained using following equations.

Equation 3.3[156] shows, that the residual pump power P_r in the even order Raman laser case is minimized by using the low reflectivity of the output coupler as well as it depends on the L length of the cavity, gain coefficient g_0 , α_j absorption and $\rho_j = \frac{\alpha_j}{2g_j} - \frac{\ln(R_j^- R_j^+)}{4g_j L}$, where R_j^+ is an output and R_j^- input coupling reflectivity of the j Stokes order.

$$P_r = P_{in} R_0^+ \exp \left[-4g_0 L \left(\sum_{\substack{j=2 \\ j \text{ even}}}^n \rho_j + \frac{\alpha_0}{2g_0} \right) \right] \quad (3.3)$$

On the other hand, Equation 3.4[156] shows, that for the odd order Raman laser, the P_r is on the both sides of the equation and therefore, maximizing the reflectivity of the output coupler is going to increase the residual pump depletion.

$$P_r = P_{in} R_0^+ \exp \left[-\frac{P_{in} - P_r}{\sum_{\substack{j=1 \\ j \text{ odd}}}^n \rho_j} \right] \quad (3.4)$$

The higher DRL efficiency at tighter focusing agrees with the optimization of Raman stimulated scattering shown in [27] where it is stated that the lowest threshold for the SRS is achieved at the optimum value of the ratio between the pump confocal parameter (twice the Rayleigh range) to the Raman crystal length of 0.5 which for the Nd:YAP would mean focusing to the spot size of a $w_0 = 20\mu m$ radius (4σ). The confocal

parameter follows the equation $z_{bcf} = 2 \frac{\pi w_0^2}{M^2 \lambda}$ and for the Nd:YAP laser of beam quality $M^2 = 1.1$ operating at $\lambda = 1.08 \mu m$ focused to a spot size diameter of $144 \mu m$, it is about $z_{bcf} = 30 mm$ which is almost an order of magnitude longer than the length of the diamond. This means that decreasing the confocal parameter of Nd:YAP laser - or focusing tighter, the efficiency of the DRL should also increase.

To summarize - the chosen output coupler was 30% (from available 15 ,30 and 60%) which seemed to be optimal taking into account a pump diameter of $140 \mu m$. This allowed to reasonably safely operate the DRL avoiding damage and maximizing the efficiency. To increase the damage threshold point and use tighter focusing one might think that it would be beneficial to use a Brewster cut crystals which would increase the possible pumping fluence to $26 \frac{J}{cm^2}$ which is a damage point of the uncoated diamond surface[157]. Using Brewster cut diamonds also introduce the astigmatism and so a larger mode size in one crystallographic direction which would need to be taken into account for this type of design. Another important drawback is that this crystal cut requires pumping with the polarized emission which is not preferred by the industrial partners for this project.

3.5.4 Output coupler optimization - experimental results

This section presents results from the experimental output coupling optimization. The available output couplers (OC) had a partial reflectivity (PR) of 15%, 30% and 60% and a $ROC = 50 mm$. A diamond sample of a size $2 \times 2 \times 4 mm$ was chosen for preliminary tests of which OC would perform best. The pump energy was varied by the attenuator from $100 \mu J$ to $300 \mu J$. The maximum output energy from the DRL was when the pump polarization was aligned with a $\langle 111 \rangle$ crystallographic direction as is described in more detail in Section 1.3.3. Figure 3.19 shows the energy of the second Stokes shifted output at $1.5 \mu m$ wavelength with varying pump energy for three different OC PR and the results are summarized in Table 3.4. The lowest threshold was achieved for the $PR = 30\%$ OC and highest for the $PR = 15\%$ OC although all values were within the error margin. The highest slope efficiency of 46% was achieved from the $PR = 15\%$ OC followed closely by $PR = 30\%$ OC with 44% slope efficiency.

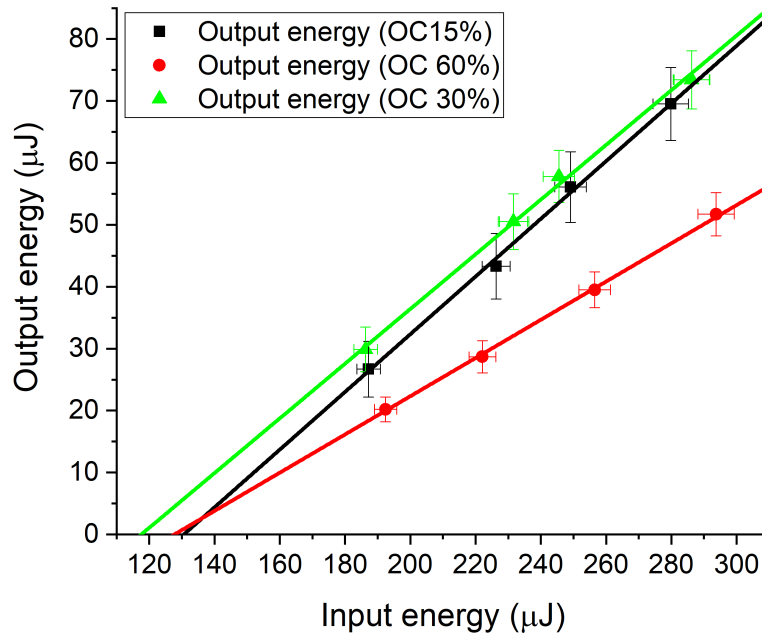


Figure 3.19: Energy transfer of the DRL working at $1.5\mu\text{m}$ wavelength range versus output coupling. Solid lines are linear fits of the data.

A reason to choose a $PR = 30\%$ OC was that a damage to the diamond's coatings was observed when using $PR = 15\%$ OC possibly due to a high first Stokes intracavity field. As suggested in [83] the careful choice of the OC can deplete, or enhance the first Stokes intracavity field which could influence the damage threshold of coatings or mirrors. The experimental results are consistent with the modeling presented in Section 3.5.3 where the efficiency between OC PR of 15% and 30% should not change as much and fall off for OC PR of 60%.

| Output coupler reflectivity % | Slope efficiency % | Threshold μJ |
|-------------------------------|--------------------|-------------------------|
| 15 | 46.6 ± 1.6 | 130 ± 8 |
| 30 | 44.1 ± 1.6 | 118 ± 9 |
| 60 | 30.8 ± 0.6 | 127 ± 5 |

Table 3.4: Comparison of the performance of the DRL laser versus reflectivity of the output coupler.

3.6 Diamond Raman laser performance

This section aims to measure characteristics of the DRL such as efficiency, transient analysis and spectral analysis. Figure 3.20 shows a setup used. Observation of pulses of each Stokes signals could be done with a use of a monochromator (Edmund Optics) which acted as a wavelength discriminator. An additional 45 deg dichroic mirror, HR at $1.5\mu\text{m}$ was used to direct the light onto an energy meter (Thorlabs, ES111C) for energy measurements. On the output of the monochromator, a photodetector (Thorlabs, 1 – $1.7\mu\text{m}$ 350MHz GaAs) connected to an oscilloscope was placed to show time traces of each signal. A lens was used to focus the DRL output beam into the monochromator ($f = 35\text{mm}$ coated for high transmission at $1050 - 1700\mu\text{m}$). The monochromator's entrance and exit slits were $100\mu\text{m}$.

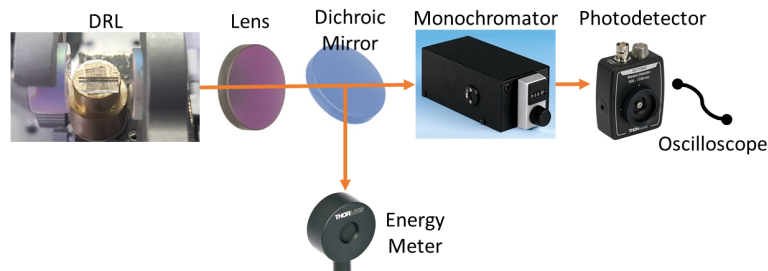


Figure 3.20: A setup for measuring the pulse traces at first, second Stokes and depletion of the pump. Dichroic mirror allowed for measurement of the output energy at $1.5\mu\text{m}$.

3.6.1 Output energy

Energy transfers of available diamond samples (five $2 \times 2 \times 4\text{mm}$ samples and one $2 \times 2 \times 7\text{mm}$ sample) are presented in Figure 3.21. It can be seen that the 7mm sample performed best due to the longest interaction length (detailed considerations on diamond length are presented in Section 6.2). From the 4mm diamonds, Diamond 2 performed above the average of other 4mm samples. One possibility is specially well aligned cavity in this one case or unknown production differences of either coatings or diamond. Table 3.5 summarizes the thresholds and slope efficiencies for each of the diamonds. In a rough comparison to a DRL presented in [38] where a 6.9mm diamond

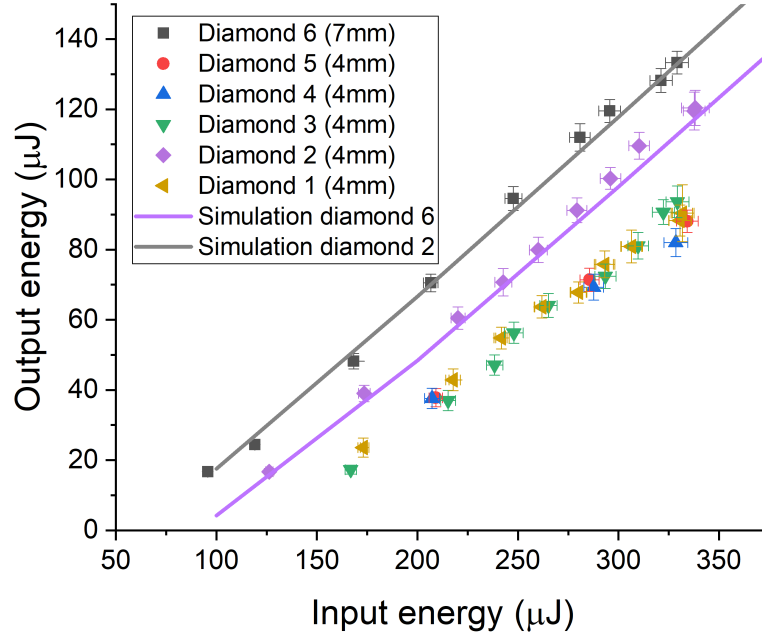


Figure 3.21: Energy transfers of DRL of all available diamond samples. Two simulated energy transfers showcase the accuracy of the model.

pumped with $1.064\mu\text{m}$ had a slope efficiency of 56% which is comparable to the slope efficiency of 50% achieved with the 7mm diamond in this experiment.

| Diamond | Threshold μJ | Slope efficiency % | Maximum output energy μJ | Maximum conversion efficiency % |
|---------|-------------------------|--------------------|-------------------------------------|---------------------------------|
| 6 | 64.9 ± 0.1 | 50 ± 1 | 133.3 ± 3.2 | 40.5 |
| 5 | 115.1 ± 0.2 | 41 ± 2 | 88.1 ± 3.2 | 26.4 |
| 4 | 105.5 ± 0.2 | 37 ± 2 | 82 ± 4 | 25 |
| 3 | 130.1 ± 0.1 | 46 ± 1 | 93.6 ± 4.5 | 28.4 |
| 2 | 92.52 ± 0.03 | 49 ± 1 | 120.4 ± 5 | 35.6 |
| 1 | 114.8 ± 0.1 | 42 ± 1 | 90.4 ± 8.1 | 27.2 |

Table 3.5: Summary of the diamond samples performance in the DRL obtained with the output coupler of PR=30%.

3.6.2 Output pulse analysis

Analysis of the first, second Stokes and both depleted and an input pump signals was achieved using setup shown on Figure 3.20 where the signal was recorded with a 350MHz photodetector connected to a 1GHz bandwidth oscilloscope. Figure

3.22a shows output pulses from a DRL (with a $7mm$ diamond, pumped with $300\mu J$ of Nd:YAP output energy, OC used was $PR = 30\%$) at first, second Stokes as well as depleted pump after only one pass through the diamond - leakage through the output coupler - and the input pump (leakage through the misaligned DRL). After the pump pulse reaches the threshold for the first Stokes oscillation, first Stokes pulse begins to rise, after which the pump pulse depletes (transfer of the energy to the Stokes emission). The first Stokes pulse builds up and caps[158, 159] at the intensity needed to generate the second Stokes. In turn, the second Stokes pulse rises after its threshold is reached by the first Stokes intracavity field. Then both of the Stokes fields reach their maximum value, after which as the pump pulse begins to fall off, the Stokes fields also fall with a trailing edge of the pulse equal to a cavity decay time.

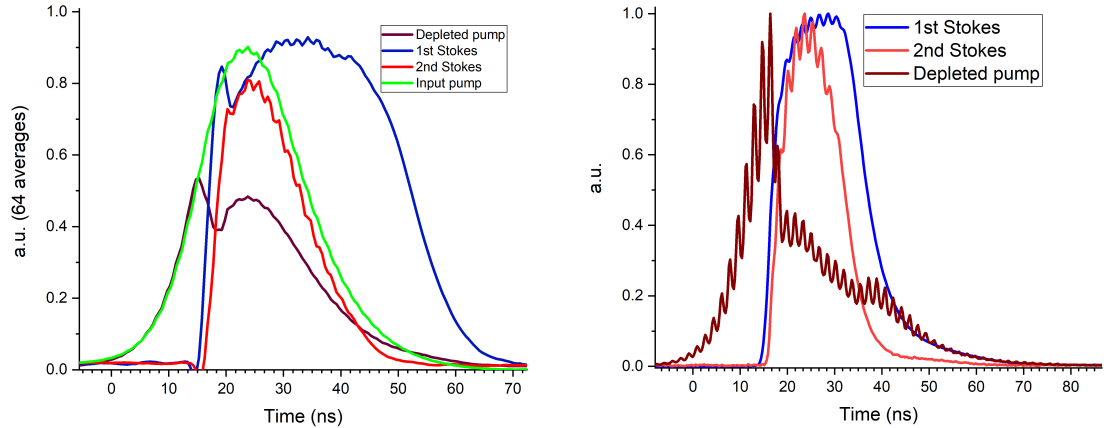
In Figure 3.22a the full-width half maximum of the input pump pulse was about $20ns$ and the resulting second Stokes pulse was about $16ns$. The first Stokes pulse was $35ns$ which was much longer than the pump pulse which agrees with the simulations and also was observed in [38, 83]. The first Stokes pulse duration can be broken down into three parts: (i) increase of the first Stokes field due to the Raman gain[38, 40, 68], (ii) plateau due to the energy transfer towards the second Stokes field and (iii) decay of the pulse with a time equal to the cavity decay time $\tau = \frac{-2L}{c \ln(R1 * R2 * (1 - T)^2)}$ [40].

The decay time of the first Stokes pulse was fitted by converting the falling edge part of the pulse into $y = \alpha e^{\beta x}$ natural logarithmic scale and fitting the data with a linear regression equation $\ln y = \ln \alpha + \beta x$ where $\frac{1}{\beta}$ is a decay time of the exponential function. The measured decay time of the first Stokes pulse was $\tau_{1s} = \frac{1}{\beta} = 5ns$ and roughly agreed with the calculated cavity decay time $\tau_{1s} = 3.6ns$ [40], where $L = 22mm$ is an optical cavity length, $R1 = 0.99$ and $R2 = 0.99$ are mirror reflectivities at first Stokes wavelength and $T = 0.01$ is an assumed cavity loss which is a reasonable assumption for a very high Q cavity. The difference in the calculation and the measurement can partially be explained by the unknown differences in the high reflective coatings on of the mirrors at the first Stokes wavelengths which are specified as $PR > 0.99$

The second Stokes pulse measured decay was $\tau_{2s} = 4.8ns$ which was much longer than the $\tau_{2s} = 0.1ns$ of the calculated value for $R1 = 0.99$, $R2 = 0.3$, $L = 22mm$ and

$T = 0.01\%$. Of course, the additional losses T can be different for second Stokes compared to the first Stokes fields, but the increasing the losses only decreases the decay time instead of increasing it and decreasing the losses does not lead to an order of magnitude difference in τ before reaching unreasonable values. The most likely assumption would be that whereas the first Stokes field has a clear pump cut-off, the second Stokes does not. It is because the first Stokes pulse oscillates in the high Q cavity and its plateau part as well as the decaying part of the pulse can still have enough intensity to generate the second Stokes signal.

Figure 3.22b shows the output pulses for the DRL with a $4mm$ diamond and OC $PR = 15\%$. The second Stokes pulse had a duration of about $FWHM = 13ns$ for the same $FWHM = 20ns$ pump pulse and was $3ns$ shorter than in the case of $PR = 30\%$ as expected. In this measurement, it was possible to record the depleted pump after the second pass in contrast to Figure 3.22a, where only single pass of the depleted pump is shown. The double passed depleted pump does not have an additional bump as in the single pass case meaning that the second pass contributes to the energy transfer to the second Stokes signal.



(a) Output pulses of the DRL at first, second Stokes and the pulse traces of input and depleted pump. $7mm$ diamond, $30\%PR$.

(b) Output pulses of the DRL at first, second Stokes and the pulse traces of input and depleted pump. $4mm$ diamond, $15\%PR$.

Figure 3.22: DRL output pulses at different output coupling.

The first Stokes pulse duration in the case of OC $PR = 15\%$ and $PR = 30\%$ (at second Stokes wavelength) were $20ns$ and $35ns$. As the cavity is highly reflective at the

first Stokes wavelength in both cases, the difference in the first Stokes pulse duration could be a sum of different cavity decay τ values due to the slight difference in the reflective coatings at the first Stokes wavelength and possible impact of the higher order DRL laser modes. It needs reminding, that the Nd:YAP laser output signal showed a mode beating behavior which is also present in the Stokes pulses.

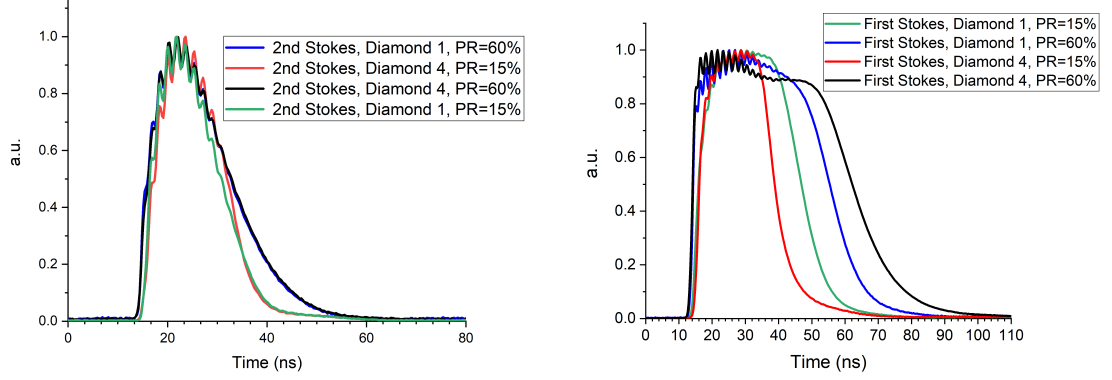
For completeness, the time traces of the first and second Stokes pulses with an output coupler of $PR = 15\%$ and $PR = 60\%$ at the second Stokes wavelength were measured in combination with two different $4mm$ diamond crystals. The recorded pulses of the first and second Stokes are shown in Figure 3.23.

For different diamond samples, the rise time of the second Stokes pulse in Figure 3.23a does not change indicating the same Raman gain of the diamond samples. The fall time of the pulse was fitted by the exponential decay function and was about $6ns$ for $PR = 15\%$ and about $10ns$ for the $PR = 60\%$ which is consistent with the modeling and as mentioned before, is much longer than the calculated cavity decay time probably due to a long duration of a high intensity intracavity first Stokes field. The overall pulse duration of the second Stokes pulse was $16ns$ with $PR = 60\%$ OC and $13.5ns$ with $PR = 15\%$ OC.

The first Stokes pulse duration shown in Figure 3.23b (recorded in the same experiment as the second Stokes pulses) for a $PR = 15\%$ was $FWHM = 27ns$ for diamond 4 and $FWHM = 37ns$ for diamond 1 and for a $PR = 60\%$ was $FWHM = 50ns$ for diamond 4 and $FWHM = 40ns$ for diamond 1. It can be seen, that the red and green curves of the shortest two first Stokes pulses correspond to the shortest trailing edges of the second Stokes pulse. This at least partially confirms that the long duration on the first Stokes pulse impacts the decay time of the second Stokes pulse as mentioned before. The model presented in Chapter 2 does not include impact of the higher order modes and therefore further investigation into this was not currently possible.

3.6.3 Simulation results

In this Section a brief analysis of the results in the context of the model is presented. It will be seen, that the gain coefficient parameters and assumed absorption



(a) Measured second Stokes output pulse with different diamonds ($4mm$) and different output couplers.

(b) First Stokes output pulses with different diamonds ($4mm$) and output couplers used in the DRL.

Figure 3.23: DRL output pulses at different output coupling.

in the diamond crystal are reasonably close to the literature reported values and the simulations give an adequate representation of the experimental results. Firstly, fitting of the time traces of the DRL will be shown followed by the energy transfers for two diamonds.

The pump simulation parameters were identical to those in the experiment and were presented in Table 3.3. Nd:YAP laser was operating at $1079nm$, $20Hz$ with $21ns$ output pulses focused down to $144\mu m$ spot diameter. The DRL cavity had a plane input coupler anti-reflective at pump wavelength and highly reflective at first and second Stokes wavelength. The output coupler was $ROC = 50mm$ and highly reflective at first Stokes wavelength and $PR = 30\%$ at second Stokes wavelength. Diamond length was $4mm$ with the absorption coefficient assumed to be $a = 0.003cm^{-1}$ at all wavelengths.

Figure 3.24 shows simulated pump, depleted pump and first and second Stokes time signals in the output of the DRL. The amplitude of the simulated signals were adjusted to match the rising edges of the measured signals. The simulated depleted pump shows a double passed depleted pump whereas the measurement shows a single pass depleted pump and that explains the additional energy in the measured depleted pump pulse at $20 - 35ns$ time. It can be seen in Figure 3.24, that the measured pulses duration of Stokes and pump signals matches well with the simulation. Also the point at which the depletion of the pump starts to occur is quite consistent with the model as seen on

the purple curve.

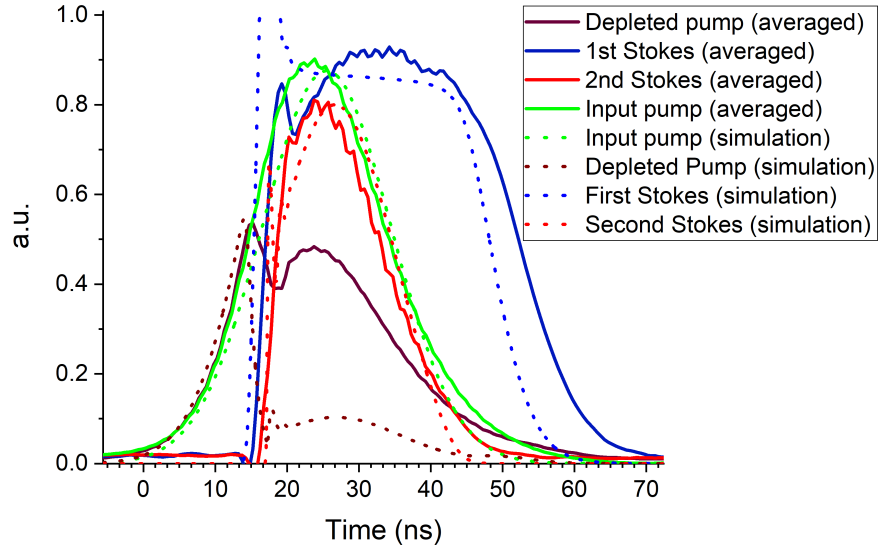


Figure 3.24: Simulated time traces in the DRL of the depleted pump, first and second Stokes emission.

To simulate the output energy of the DRL, an integration of the second Stokes pulses was performed and the results are presented in the Figure 3.25. The simulations were performed with the same set of parameters as mentioned before for two lengths of the diamond $4mm$ and $7mm$. As seen, the measured and simulated values for the output energy match quite closely.

This Section showed, that the model described in Chapter 2 is adequate to predict the DRL performance and is in line with the literature reported values for important coefficients. The theoretical analysis of the output coupler optimization in [156] is also consistent with the results. Therefore, the model was further used to create discussion on the other optimal conditions for the DRL operation and these are presented in the conclusion chapter.

3.6.4 Output spectrum of the Diamond Raman laser

An automated monochromator (Spectral Products, CM110) was used to measure the output spectrum at the individual Stokes wavelengths. Using a leakage through the output coupler and a setup similar to the one shown on Figure 3.20 it was possible

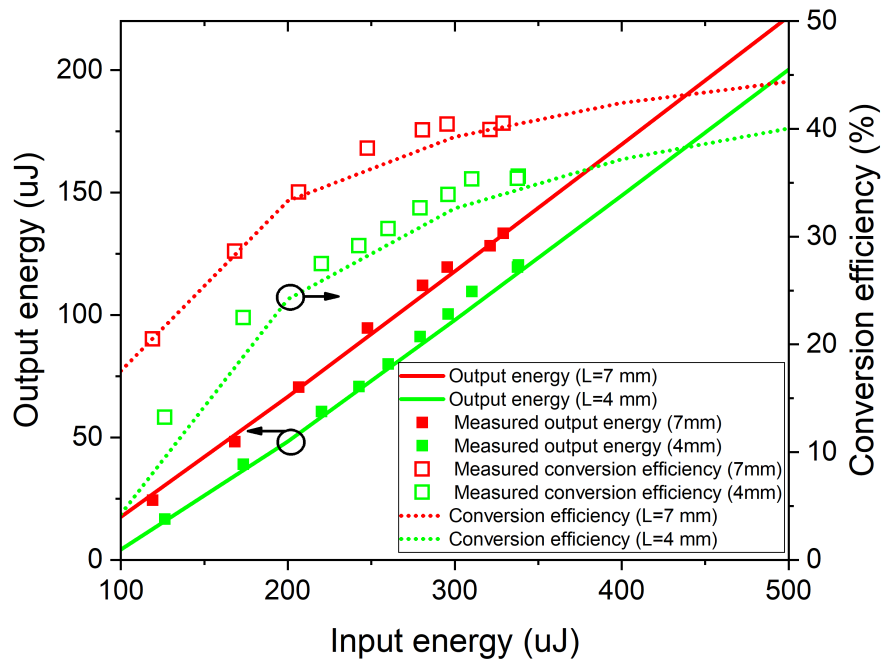


Figure 3.25: Simulation and measurements of the energy transfers and conversion efficiency of the DRL performance with the 4mm and 7mm diamonds.

to observe emission at both Stokes wavelengths at $1.2\mu\text{m}$ and $1.5\mu\text{m}$ as well as the pump leakage. The monochromator used in this experiment was an automated grating monochromator with a wavelength resolution of 0.2nm and a wavelength accuracy of $\pm 0.6\text{nm}$ which was connected to a smart scope (LabNation). Both the monochromator and the scope were connected to the computer through a LabVIEW plugin. This allowed the transmission wavelength of the monochromator to be tuned while recording the signal on the photodetector. Figure 3.26 shows an output spectrum recorded through the setup. This is not a linewidth measurement since the expected linewidth (0.2nm [3]) is less than the instrument resolution. The structure of the spectral lines could be an outcome of the time averaging of the collected data. Each emitted laser pulse lasted about 20ns whereas the averaging window was about a 1ms so with 20Hz repetition rate, for a single monochromator wavelength step, measurement was taken of a different pulse.

The emission of the first Stokes was observed at 1262nm and second Stokes at 1515nm . The lines are separated by $1320 \pm 29\text{cm}^{-1}$ where the literature reported value

is 1332cm^{-1} [3]. The large error was due to the instrumental limitation as well as the fact that the scanning took place over number of pulses.

The main outcome is that there is a very clear emission in the second Stokes wavelength region and at the available pump energies ($< 400\mu\text{J}$). The achieved wavelength is above $1.5\mu\text{m}$ which makes this proof of concept viable to generate eye-safe wavelengths. More detailed spectral analysis was undertaken for the fibre-laser pumped DRL described in Chapter 4.

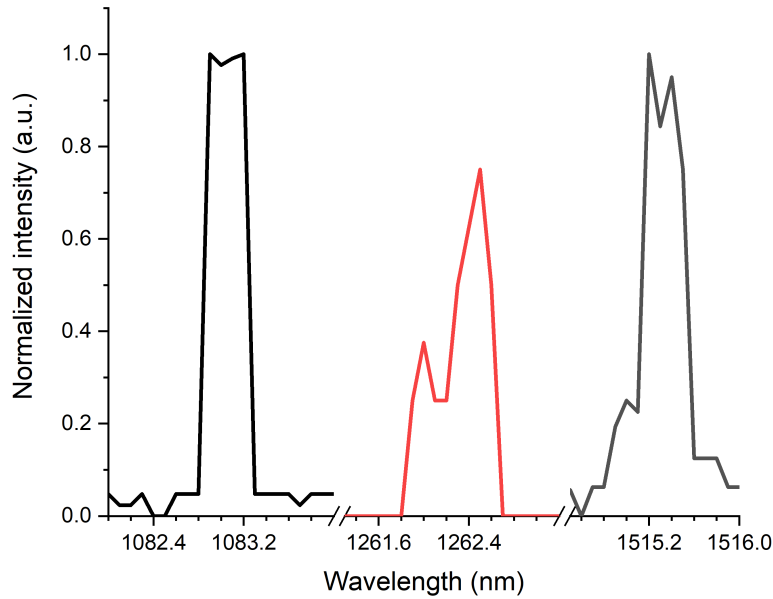


Figure 3.26: Output emission wavelength cascade from the DRL.

3.7 Summary

This Chapter showed that the developed DRL is a proof of concept for generating eye-safe wavelength and that diamond is an enabling component for this technology. Firstly, the Nd:YAP laser was developed with a repetition rate of 20Hz , 0.5mJ output energy and 20ns pulse width which met the requirements for the DRL pumping. The available energy was about $5\times$ higher than the achieved threshold for the generation of the second Stokes emission. Then, the DRL was developed with the emission wavelength above $1.5\mu\text{m}$ which was a requirement for industry. Maximum output energy

Chapter 3. Diamond Raman Laser prototype

was $130\mu J$ at $1.5\mu m$ with the repetition rate of $20Hz$. The requirement for high average power can not be met due to the thermal issues of the pump laser. To overcome this, a fibre laser was employed as a pump which could operate in kHz to MHz regime. The fibre pumped DRL is described in Chapter 4.

Chapter 4

Fiber pumped Diamond Raman Laser

Chapter 3 showed a proof of concept system converting $1\mu m$ wavelength to $1.5\mu m$ through a second-Stokes Raman conversion in diamond. The maximum output energy reached was about $120\mu J$ but the requirement for high average power and repetition rate operation was not. To achieve the latter, a more powerful pump source that could operate at high average powers had to be used. The approach of using an Yb:fibre Master Oscillator Power Amplifier (MOPA) as a pump was chosen due to the scalability of the average power of Yb: fiber lasers (as described in detail in Section 1.4) as well as the expertise provided by the collaborators in the project at the ORC (Optoelectronics Research Center) at University of Southampton. The MOPA system that was developed by the ORC met the requirements for the pulse energy determined in Chapter 3 at relatively high repetition rate and high average power.

The elements of the MOPA system are described in the next Section based on the ORC publication in [106]. Further on, a brief characterization of the output pulses and spectrum is presented as measured during the DRL experiments (not from the publication). Further sections provide the results of the DRL experiments with the MOPA system as a pump. An important remark has to be made here - the sets of data were usually taken during visits to Southampton that were months apart and therefore direct comparison should be done carefully always keeping in mind, that the DRL cavity

was rebuilt each time - with slightly different cavity length and overall alignment etc. Additionally, due to the limited time with the pump laser (due to reliability of one of the fibers or time constraints) the full set of data (pulse traces, power transfer, spectra) was difficult to obtain at times.

4.1 High average power pump source for diamond Raman lasers

The schematic of the MOPA system itself is presented in Figure 4.1 and now its elements will be described. To summarize the ORC's work as reported in [106], this system consisted of a narrow linewidth diode laser as a seed source. This DFB (distributed feedback) diode laser operated in CW with $40mW$ output power, $1083nm$ wavelength and a specified linewidth of $< 2MHz$. This linewidth was later broadened by the electro-optic phase modulator (EOPM) driven by the white noise source (WNS) in order to mitigate for SBS (stimulated Brillouin scattering) in the amplification stages[160–162]. To meet the requirements of the pulse energy with high repetition rate, the CW output of the seed laser was modulated by an AOM (acousto optical modulator) to achieve pulses with the duration of $18ns$. The amplification stages consisted of the polarization maintaining ytterbium doped fibers of X/Y core and cladding diameters (e.g. PM-YDF 5/130 on Figure 4.1) and were separated by the isolators (ISO) to prevent back reflections. Hybrid isolators (Hybrid-1,2) were also filters to block the amplified spontaneous emission from propagating in the amplification chain. The maximum output average power after 5 amplification stages was $120W$, $150kHz$ repetition rate, $0.8mJ$ pulse energy, linearly polarized at $1083nm$ with a $69GHz$ linewidth. The linewidth is about $2.3cm^{-1}$ and corresponds roughly to the Raman gain bandwidth in diamond of about $2cm^{-1}$ [3]. A beam quality was good at $M2 = 1.2$. The schematic also shows mirrors (M-1,2,3) and lenses (f-1,2,3) used for alignment of the laser beam into the fifth amplification stage and f4 to align the pump beam. Polarization optics ($\lambda/2$,PBS) were placed after the MOPA output to maximize its power.

One of the issues encountered during the experiments was reliability of the fifth

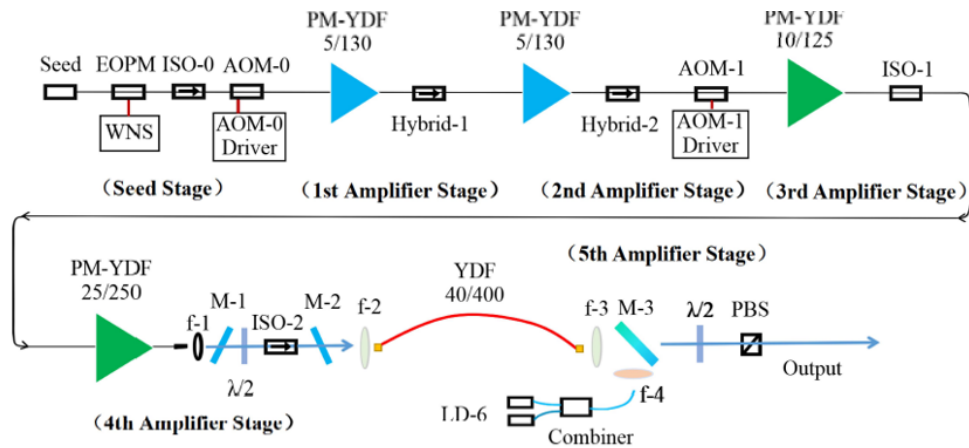


Figure 4.1: MOPA system developed by the University of Southampton (Optoelectronics Research Center) which was used as a pump source for DRL[106].

amplification stage optical fiber in the MOPA system. Most of the measurements presented in this Chapter are done with the fiber YDF 40/400 but reaching high powers as well as having time to record full data sets proved to be difficult - the endings of the fiber kept evaporating when reaching powers of $\approx 50W$ at $150kHz$ operation in an unpredictable fashion. To prevent this, end-caps were used that expanded the fiber end tip areas to allow, in theory, for larger damage threshold [163]. Unfortunately, at this stage, the middle of the fiber damaged. The reliability and system complexity is a very important point of discussion for the industrial partners and lessons learned by using this fiber led to replacing it by a multimode Yb based fiber (ORC, 100/760) which proved to be more reliable.

The remarkable feature of the original fiber, as noted in [106], was that despite it not being polarization maintaining, the output light was polarized in about 83% and after using a high power polarization beam splitter in the output beam path, the output light from MOPA was fully polarized retaining most of the power in one polarization ($\approx 80\%$). This allowed for the DRL pump light polarization manipulation. On the other hand, the multimode fiber output was unpolarized which allowed us to greatly simplify the setup by removing the polarization dependent optics making it more attractive for the industrial partners. Another consequence of using the unpolarized emission was that the isolator preventing the DRL back reflected light from going

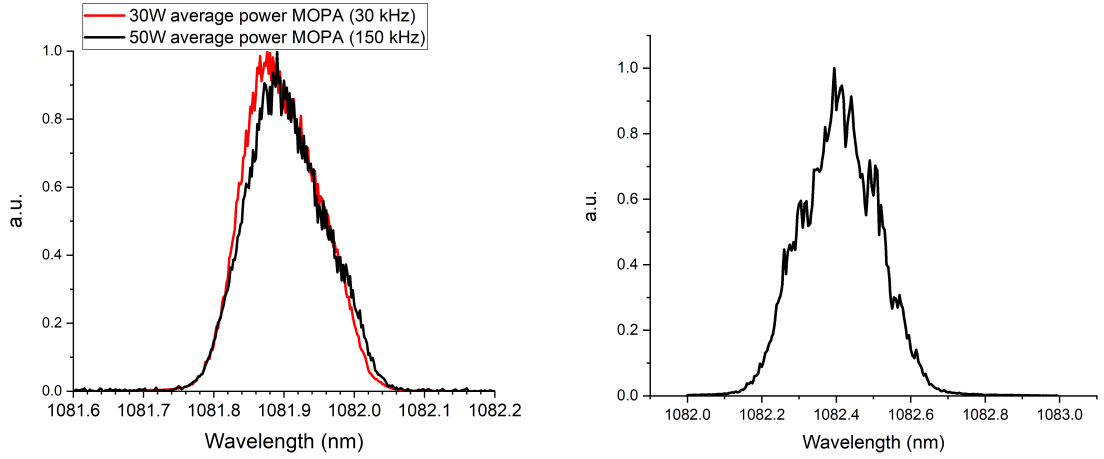
back into the MOPA system was replaced by a polarization independent isolator (SPI) and ultimately completely removing the isolator would be desirable by exploring the possibility of off-axis pumping. Off-axis pumping would save additional cost (polarization dependent high power isolators cost about 3500\$, EOT website, 2019) as well as remove the back reflections from the diamond Raman laser. At the same time the emission of $1.5\mu m$ was still possible with comparable $\approx 10W$ output average powers as in the polarized pump case. It is not a trivial case to compare these two results (with polarized and unpolarized pumping) since not only was the polarization a factor but using a multimode fiber - due to the larger core size - the beam quality decreased from $M^2 = 1.2$ to $M^2 = 5.7$ (measurement provided by University of Southampton) which could also influence the DRL performance.

Characterization of the MOPA system that follows in further sections (spectral, output pulses, output power) was measured by the author unless specified otherwise in the text.

4.1.1 Output spectra of the Yb fiber MOPA

In this Section, output spectra of the MOPA are included that were measured during the work on DRL. Results from before replacing the fifth stage fiber are referred to as "polarized emission" and after replacing the fiber as "multimode emission". Figure 4.2a shows the output spectrum recorded with an optical spectrum analyzer (OSA) ANDO AQ6317B with $0.01nm$ resolution for the polarized emission of the MOPA. The center wavelength of the emission was $1081.9nm$ with the FWHM linewidth of $0.13nm$ for both $30kHz$ and $15W$ average power and $150kHz$ and $50W$ average power operation. The emission of the MOPA after the fifth stage fiber was changed to the multimode one was measured with ANDO AQ6315E with a $0.05nm$ resolution and is presented in Figure 4.2b. It shows that the center wavelength was $1082.4nm$ and the FWHM linewidth was $0.25nm$ with $150kHz$ and $50W$ operation.

The output spectra measurement has another important function closely related to the output power measurement. The Yb fiber lasers emission consists usually of a main peak wavelength (determined by the seed laser and amplification bandwidth of



(a) Output spectrum of MOPA system (polarized emission) at $30kHz$ and $150kHz$ operation at $15W$ and $30W$ average power respectively.

(b) Output spectrum of MOPA (multimode) at $150kHz$ and $50W$ average power.

Figure 4.2: Normalized to maximum values output spectra of the MOPA system in polarized and multimode configuration.

the power amplifiers[66]) where usually maximum power is concentrated although if not addressed through a careful design, an ASE (amplified spontaneous emission) band at a wavelength range of $1030 - 1070nm$ [135, 164, 165] can also significantly contribute to the total output power. Because of the broad spectrum of the ASE, it is not useful for Raman conversion and its amount in the overall output power of the fiber laser had to be assessed. This assessment was done by evaluating the output spectrum and comparing the integrated area of the main emission peak to the area of entire spectrum. This procedure is described now.

The scan of the MOPA spectrum between $1000 - 1100nm$ with a $1nm$ resolution (to allow the OSA measurement of such a wide spectrum scan) was done and is presented in Figure 4.3. It was then converted to linear scale for convenience in integrating the area under the curve. The linear scale plot is not shown here since it is less readable than the logarithmic scale in the case of large differences in signal levels as in the case of relatively small ASE and large signal levels. The integrated amplified seed emission at $1080.6 - 1084.5nm$ consisted of 99% emission of the entire MOPA output spectrum. Therefore the ASE was found to be less than one percent of the total energy in the

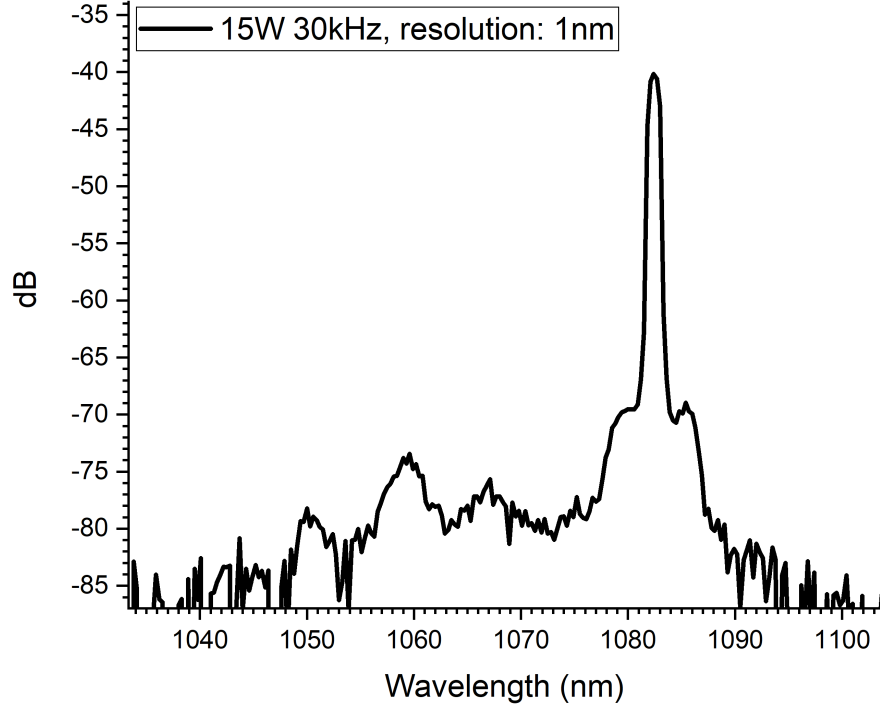


Figure 4.3: Wide scan of the MOPA output emission.

spectrum and hence was negligible.

4.1.2 Pulse traces of the Yb MOPA

To record the output pulses from the MOPA, the light was attenuated with ND filters and filtered by a manual monochromator (Edmund Optics, slits = $100\mu m$) which allowed us to observe a wavelength of interest. The light then was transmitted onto a photodetector (Thorlabs, 1 – $1.7\mu m$ 350MHz GaAs) connected to an oscilloscope and the result is shown in Figure 4.4. The pulse duration of the MOPA (gray curve) was $15.5ns$ both for $30kHz$ and $150kHz$ operation and for comparison an output pulse from the Nd:YAP is shown with the $23ns$ duration (red curve). It can be seen, that the rising edge is the same (both pulses are normalized to their maximum values) with the longer falling edge of Nd:YAP. The advantage of shorter pulse duration δt is that, for the same pulse energy E , the peak power is higher $P_{peak} = \frac{E}{\delta t}$. It should be mentioned here, that for both $30kHz$ and $150kHz$ the maximum pulse energy achieved was about $0.5mJ$. No particular differences were seen when using multimode or polarized emission which

was as expected since the pulse length only depends on the seed laser pulse shaping as described before.

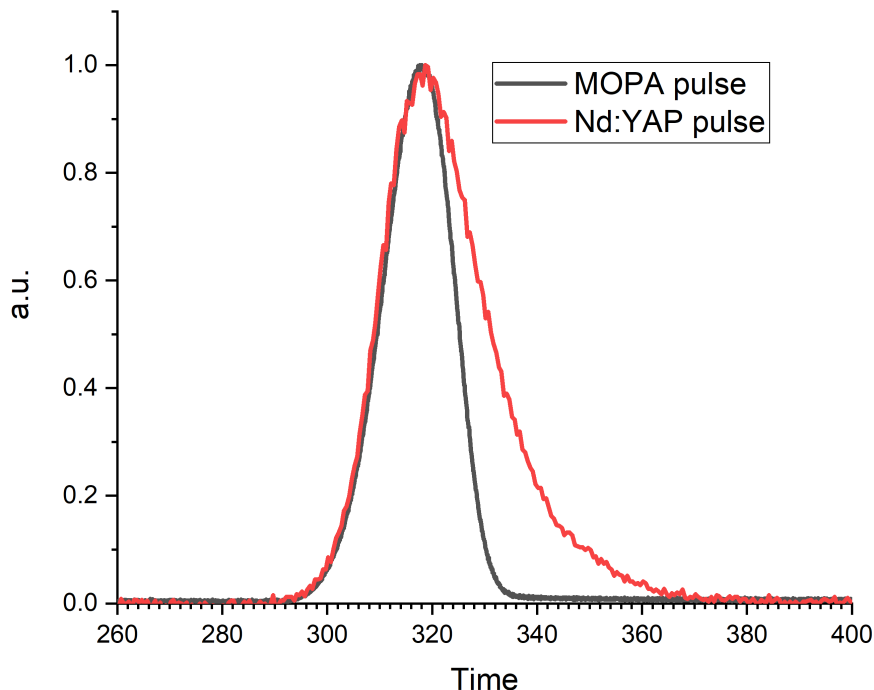


Figure 4.4: Output pulses of the MOPA system. $150kHz$ operation, $30W$ average power, Nd:YAP pulse for comparison.

4.1.3 Summary of Yb MOPA measurements

This section concludes a preliminary characterization of the MOPA system where it was found that the pulse energy was adequate for the DRL experiments with the energy of about $0.5mJ$ and about $30kW$ peak power. The ASE in the output power was negligible making it easier to assess the input power for the DRL experiments. It has to be mentioned though, that, by design, the seed for the MOPA system operated with the $600kHz$ repetition rate and the reduction to either $30kHz$ or $150kHz$ was done by a pulse picker (acousto-optic modulator) which picked every n -th pulse and rejected the pulses in between. It was found that the rejected pulses are not completely isolated and make their way through the amplification chain. The assessment of the power in between the useful pulses proved to be extremely difficult and therefore, it is not taken into account in the power transfers measurements in further sections. Possible

solutions would be to improve the diffraction efficiency of the pulse picker or increase the repetition rate of the system. The latter solution would deplete the available energy in the amplification chain as well as increase the duty cycle; it is also a goal of the project - to increase the repetition rate and average power of the DRL.

In the next section, a description of the conditioning optics for the DRL pump is presented. Also presented are beam profiles for multimode and polarized MOPA output. It will be made clear in the text if the following data was produced by the polarized single mode or unpolarized multimode pumping.

4.2 Beam conditioning of the Yb fiber for DRL pumping

This Section describes the MOPA - now referred as the pump - conditioning optics system that was a buffer zone between the DRL and the MOPA output. It allowed for measuring the pump DRL input power as well as the input and depleted pump spectra. There are two different setups used depending on if the polarized or multimode (unpolarized) pump emission was used. Firstly, the beam conditioning optics will be described for each case. A comment on a difference in operating the MOPA system in both cases is also provided.

4.2.1 Beam conditioning of the polarized pumping of the DRL

In the case of the polarized pump, the conditioning optics system used for the DRL experiments was exactly the same as shown in Figure 3.15 with the collimated and polarized MOPA laser beam following the purple line along to the Raman cavity. The function of each element is described in Section 3.5.1. The measurement of the input power for the DRL was done by putting a power meter in the beam path of the rejected polarization from the attenuator. When the attenuator was closed, the beam was directed onto a power meter measuring the maximum rejected power as close to no power was transmitted to the DRL. When the attenuator opens, light was being transmitted towards the DRL and the rejected power was minimized. The input power for the DRL was then calculated by subtracting the rejected power meter reading from

the maximum rejected power. The degree of unpolarized light was negligible ($\approx 1\%$) compared to the overall measurement and did not contribute much to the error in assessing the power levels. This way of power measurement was found to be the most convenient and consistent. It has to be noted, that the MOPA system was operated at a constant output power which was thermally the most stable option for the conditioning optics system to operate. The largest thermal lens expected to develop in the system was the one in the optical isolator since it consists of a 2cm optical crystal. By keeping the isolator in front of the attenuator, the change of its thermal lens is minimized (not its absolute value) and therefore the instabilities in the rest of the system are minimized as well. Colleagues in Southampton measured, that changing the average output MOPA power from 30W to 50W and focusing the beam with a $f = 200\text{mm}$ lens, the focal position shifts by 2mm which is half of a 4mm diamond crystal. This could easily lead to focusing the high power beam onto diamond's surface and damaging it.

During one of the visit to Southampton, a beam profile at a focus of a $f = 75\text{mm}$ lens was measured at different MOPA output average powers and repetition rates to see how the beam size changes with a different thermal load in the optical elements like the isolator. Figure 4.5a shows a MOPA beam profile in the focus at 30kHz operation with 15W output power and Figure 4.5b shows a beam profile in the focus with 150kHz operation at 50W output power. The measured diameters were about $160\mu\text{m}$ and $180\mu\text{m}$ respectively at 4σ level. It shows that the beam size isn't changing dramatically when increasing the pump average power in this case although a measurement of the MOPA beam size at the focus was done before each time a DRL cavity was rebuilt. More on the topic of the beam divergence follows in the next paragraph since the situation is not constrained to one type of pumping. Additionally, another issue with the beam profile was found. Especially at higher powers, when pumping the diamond, sparking was observed on its surface. After closer inspection, it was found that the MOPA beam in the focus featured many hot spots. A speculation is that the light coming from the fifth stage fiber cladding was interfering with the signal light causing this. Figure 4.6b shows a beam of the MOPA at a focus of a $f = 100\text{mm}$ lens operating at 10W with 150kHz operation with visible interfering hot spots called speckles. These are usually

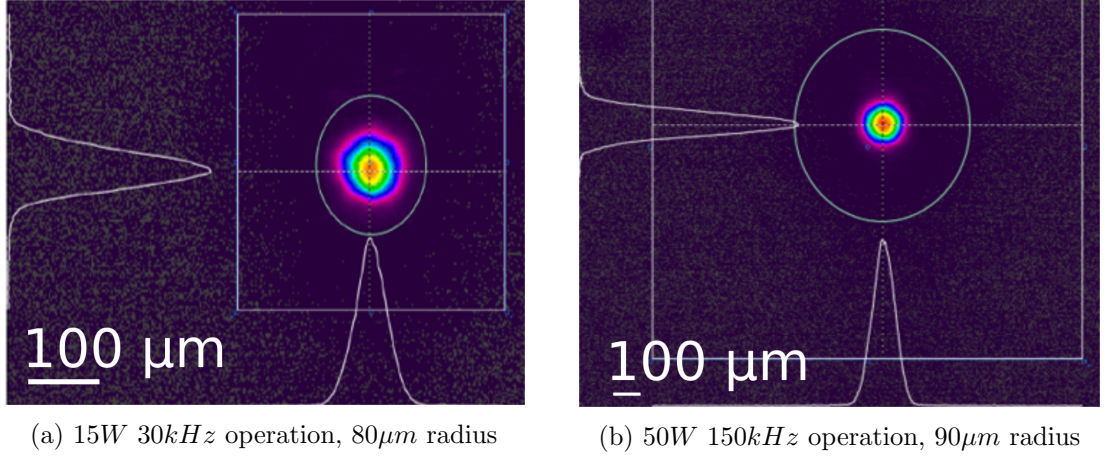


Figure 4.5: Image from a CCD camera of a focused MOPA beam at different operation conditions.

prominent for a laser with a large coherence length $L = \frac{c}{\Delta\nu}$ [40] which indicates the distance over which the laser light can interfere with itself. For MOPA system, for the measured emission bandwidth of $\Delta\nu = 33MHz$, the coherence length was about $L = 2.8m$ making it possible for the light diffracted on various optical elements to interfere at the CCD camera sensor plane. The speckles, have average radius of $r = \sqrt{\frac{4\lambda^2(f/\#)^2}{\pi^2}} \approx 2.6\mu m$ [166] for a $\lambda = 1083nm$ and a $D = 1$ inch $f = 100mm$ focusing lens and $\# = \frac{f}{D} = 4$. As the CCD camera had pixels of $4.4\mu m$ size, the speckles in Figure 4.6b appear in blotches of about $10\mu m$ radius that is reasonably close to the calculated value. After a variable aperture was placed in front of the DRL focusing lens, the beam profile was cleaned removing the interfering parts of the beam as presented in Figure 4.6a. As this aperture was not appropriate for the high power, a different aperture was manufactured by the ORC with a range of openings which was then put in front of the conditioning optics setup to minimize the amount of cladding light in the further part of the setup.

4.2.2 Beam conditioning for the unpolarized pumping of the DRL

For the unpolarized pump case, the attenuator and a half-wave plate were removed and the isolator was replaced with a polarization independent one. This time, pump power to the DRL had to be adjusted by changing the MOPA pump diodes currents.

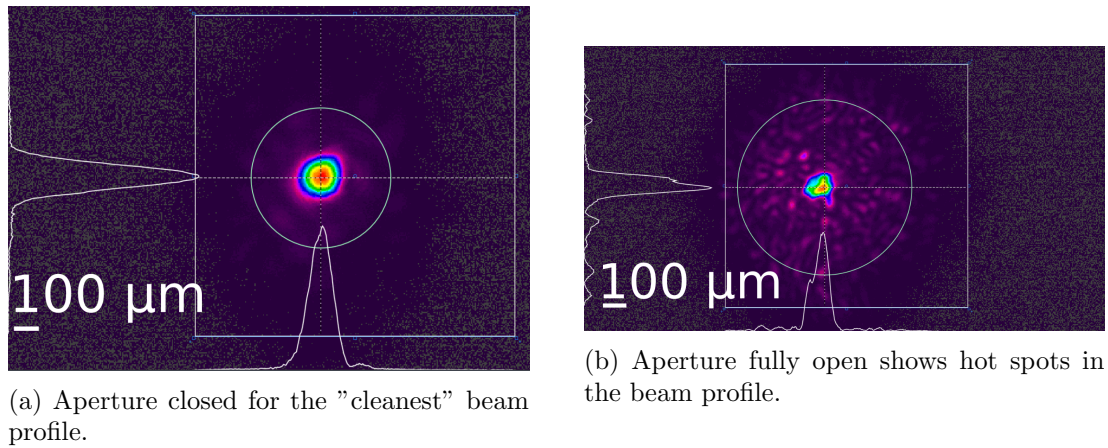


Figure 4.6: Beam profiles of the MOPA in the focus of a $f = 100mm$ lens operating at $10W$, $150kHz$.

This caused the power going through the isolator to change when changing the MOPA power. This in turn lead to forming of a different strength of thermal lens in the isolator at each MOPA operating point. Colleagues in Southampton measured, that when changing the MOPA average output power from $10W$ to $50W$ and measuring the focus position after a $f = 50mm$ lens results in a shift in the focal position by $0.5mm$ as well as increases the beam diameter from $124\mu m$ to $146\mu m$. Measuring of the beam diameter at each data point proved not to be practical so the pump spot size taken for calculations of e.g. intensities was taken at an intermediate power level (about $10W$ of average power) in the further sections with every amplification stage of the MOPA system operating. The power was not high enough to damage the CCD camera and high enough to represent a real beam size. This provided a convenient solution introducing as little error in the calculations as possible.

Figure 4.7 shows a beam profile from a CCD camera at the focus. Apart from the signal beam in the middle it can be seen that there are other transverse modes in the wings of the beam profile. It was not assessed how much power is in these; it might be possible that constructing a spatial filter in the future with an available variable high power aperture can solve this problem.

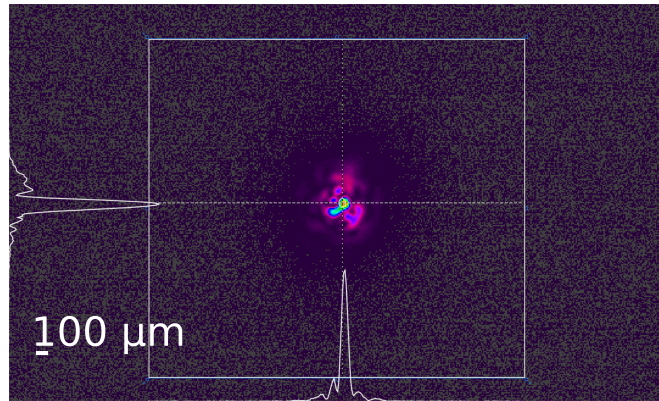


Figure 4.7: Beam profile of a multimode output of the MOPA system at $10W$, $150kHz$.

4.3 Yb fiber pumped DRL cavity and output emission analysis setup

To draw a full picture of the system, after the focusing lens in the conditioning setup, a Raman cavity and an analysis optical setup was put. The Raman cavity in Figure 3.15 was discussed in 3.5.2 and the same considerations follow in this Chapter. As a reminder - the Raman cavity consisted of a plane input coupler, highly reflective at first and second Stokes ($> 99.9\%$ at $1.2\mu m$ and $1.5\mu m$) and highly transmissive at the pump wavelength ($< 0.2\%$ at $1080nm$) and the output coupler was highly reflective at the pump wavelength ($> 99.9\%$ to allow for a double pass operation) and first shift wavelength ($> 99.9\%$ at $1.2\mu m$) and partially reflective at second Stokes $1.5\mu m$ wavelength. The diamond samples were 4 and 7mm long, coated as described in Section 3.4.

The spectra and pulse traces of the DRL emission were measured with a setup shown on Figure 4.8. The output emission from the DRL was passed through a 45 deg dichroic mirror, coated with high reflective coating (99.9%) at $1.5\mu m$. The reflected light was then directed onto a high power power meter (200W, Thorlabs) in order to measure the output power. Leakage through the 45 deg mirror was used to record pulse traces and spectra of the DRL output beam. The pulse traces of each Stokes order as well as pump (MOPA) leakage were recorded by placing a focusing lens, monochromator and a photodetector in the beam path (just as in Figure 3.20).

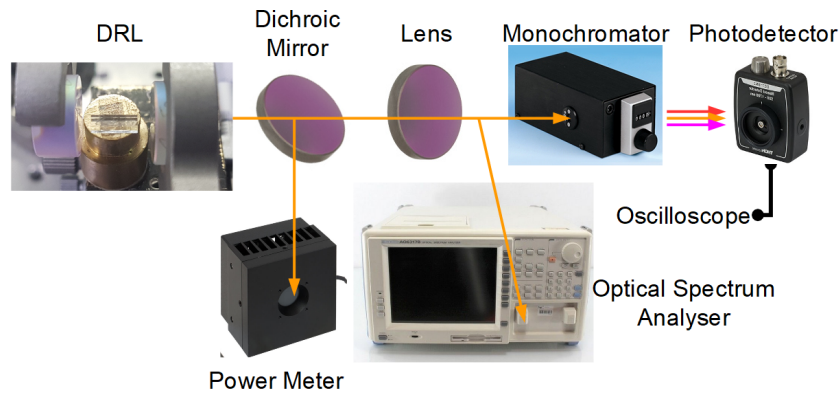


Figure 4.8: Spectrum measurement setup allowing for power, spectrum and pulse traces measurements.

To record the output spectra, an optical fiber was put into the beam path and was connected to an OSA for signal analysis. Depending on where the fiber was placed, it was possible to record spectra of the light before it entered the DRL or after double or single passing through the diamond. Comparing the double passed (depleted) and input (undepleted) pump spectra can show e.g. spectral hole burning in a case when the pump spectrum is much broader than the Raman gain bandwidth in diamond. The next Section will discuss this phenomena in a greater detail on an example of depleted and input spectra of the MOPA whilst the DRL was operating with a $1.5\mu\text{m}$ emission. The energy transfers of an operating DRL are presented later on in the Chapter.

4.4 Depleted pump spectrum analysis

As mentioned in the beginning of this Chapter - the multimode and polarized MOPA emission spectra differed in both center wavelength and the linewidth of emission. The center wavelength difference is not as important since as long as it is above $1.072\mu\text{m}$ and so the second Stokes emission would be above $1.5\mu\text{m}$. The Raman gain on the other hand, as described in detail in Section 1.3.2, depends on the pump emission linewidth. The extreme case scenario would be, that for a pump spectrum much broader than the Raman gain bandwidth ($\Delta\lambda_P \gg \Delta\lambda_R$), the Raman gain would be maximum at the

peak of the pump spectrum and deplete part of it with a linewidth of the Raman gain bandwidth.

Figure 4.9 shows the input and double passed pump (MOPA) spectra when using the polarized configuration. The MOPA system was operating at $15W$ average power with $30kHz$ repetition rate and the DRL average output power at $1.5\mu m$ was about $4W$. The input pump spectrum was measured with the maximum power in the rejected beam from the attenuator and the depleted pump was measured when maximum power was transmitted through the attenuator and after double passing through the DRL cavity. The measured linewidth was $FWHM = 0.18nm$ for both input and depleted spectra (measured with ANDO AQ6317B with a $0.01nm$ resolution). It can be seen, that both the depleted and input pump have the same shape and no spectral hole burning. The $150kHz$ data was incomplete due to the floppy drive failure and could not be recovered. It was not expected to be different than $30kHz$ data presented.

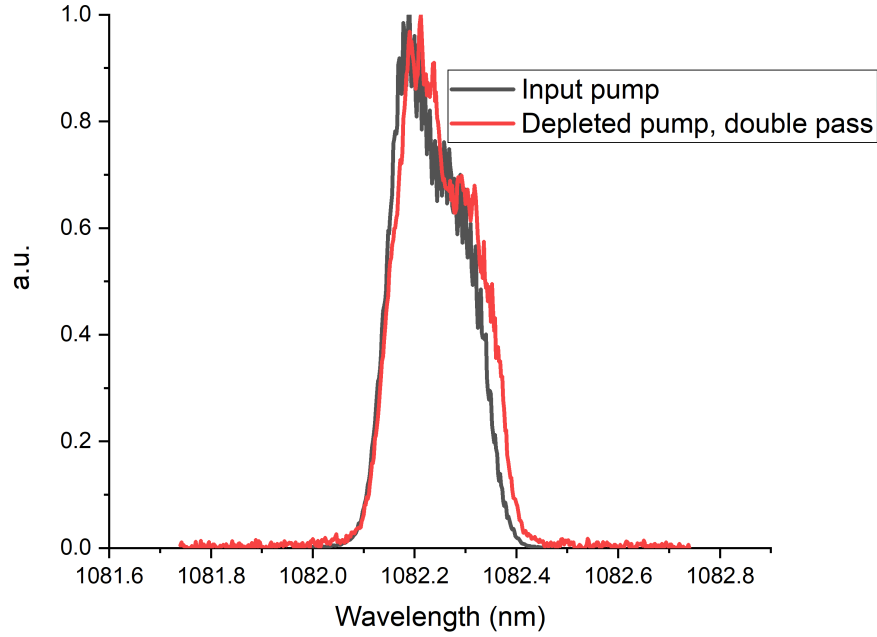


Figure 4.9: Spectra of depleted and input pump. MOPA at $30kHz$ operation, $15W$ average power, polarized emission.

After the fiber was replaced with the multimode version, the experiment was repeated. Figure 4.10 shows input and double passed depleted pump spectra at $70W$ of average power, $150kHz$ repetition rate and with the DRL emission at $1.5\mu m$ of about

9W. The depleted spectrum shows what might resemble a spectral hole that on the graph has about 0.08nm width as indicated with a blue arrow. It is not evident, but it is possible that this hole represents the bandwidth of the Raman gain. Analysis of the impact of the relatively broad spectrum of the pump to the Raman bandwidth is presented in Section 4.9.2. In the next Section a broader spectrum is presented showing spectrum peaks in the DRL emission at first and second Stokes.

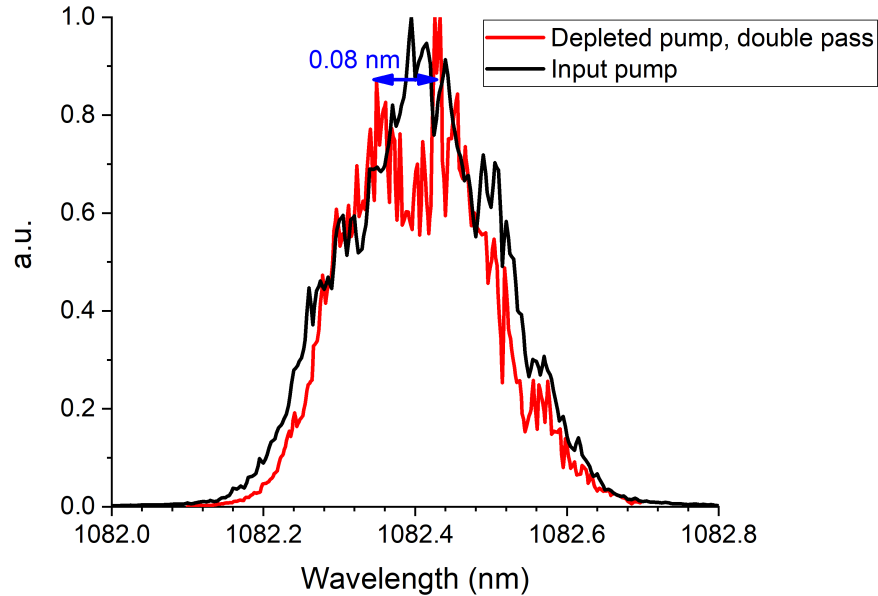


Figure 4.10: Spectra of depleted and input pump. MOPA at 150kHz operation, 70W average power, unpolarized emission.

4.5 Emission spectra of the DRL

4.5.1 Polarized pump emission

Figure 4.11 shows a wide spectrum of the DRL output measured with the setup shown in Figure 4.8. This spectrum was measured with a resolution of 2nm which allowed the scan to be stretched over the cascade of the Stokes signals - first Stokes at $1.2\mu\text{m}$ and second Stokes at $1.5\mu\text{m}$. The height of the peaks is not representative of the strength of the signals; power-wise, the second Stokes peak would be the largest, but to avoid the damage of the OSA fiber, the spectrum was measured after the highly

reflective 45 deg mirrors reflecting most of the $1.5\mu m$ emission. Now high resolution spectra are presented for the pump and second Stokes emission. Unfortunately first Stokes spectra files were corrupted and are unrecoverable.

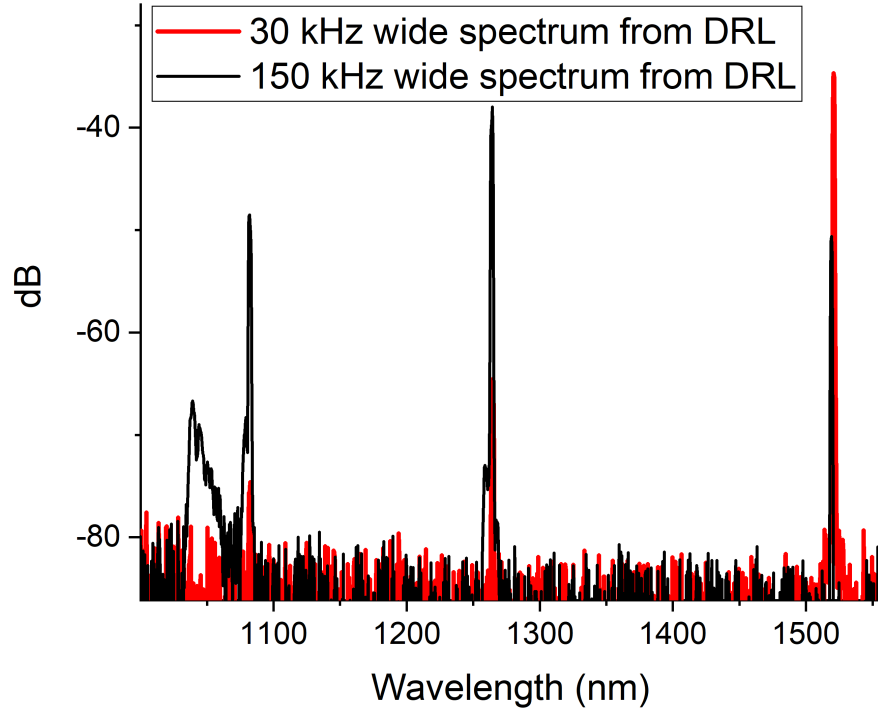


Figure 4.11: Wide spectrum of the DRL output emission.

The high resolution (taken with OSA ANDO AQ-6315E resolution $0.05nm$) of the pump emission at $150kHz$ and $30kHz$ are presented in Figure 4.12. The peak of emission at both $30kHz$ with $30W$ and $150kHz$ and $50W$ of average power is at $1081.8nm$. High resolution spectra of emission of a second Stokes signal from the DRL at different repetition rates are shown on Figure 4.13. First of all, both spectra appear at a different central wavelength; the center peak of the $150kHz$ emission is at $1518.9nm$ and the highest peak at $30kHz$ emission is at $1520.5nm$. Secondly, there are multiple peaks in each spectra. These two issues will be addressed now.

The second Stokes in $150kHz$ and $30kHz$ appears at a different wavelength (which implies a different Raman shift). This could be associated with the accuracy of the wavelength measurement of the instrument which without calibration could be $\pm 0.5nm$. As these measurements were made separated by months this is a possible explanation

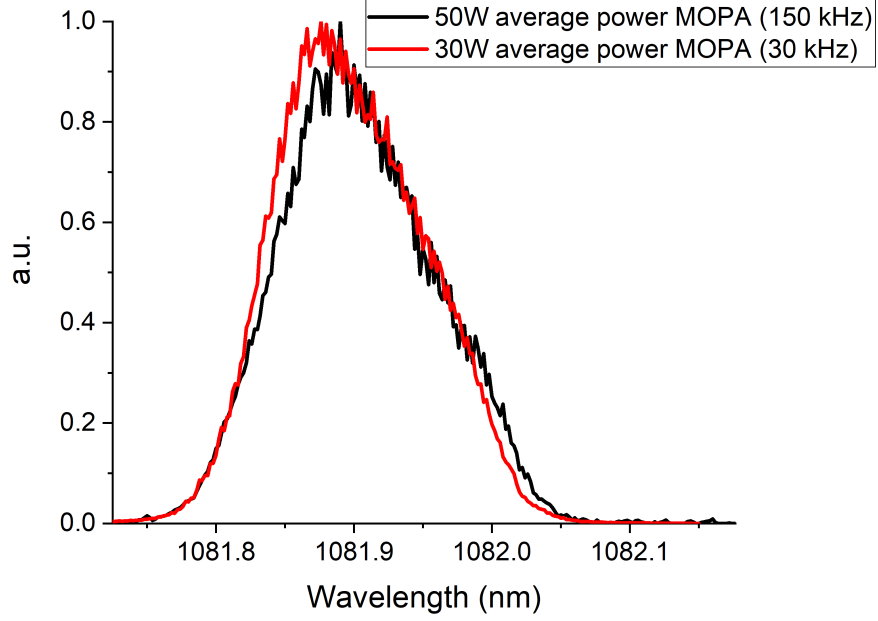


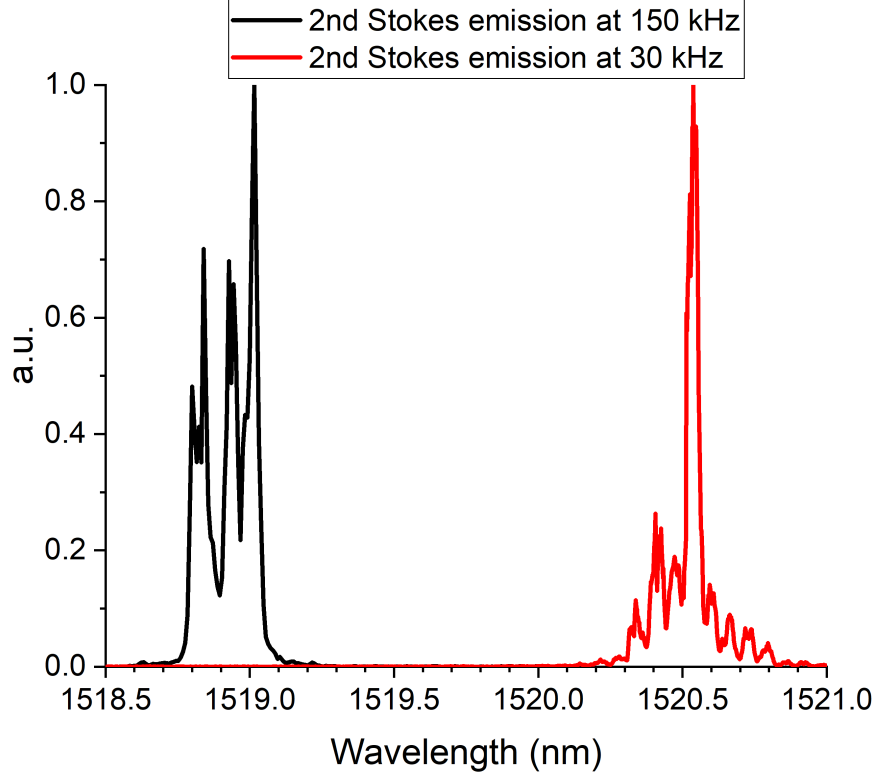
Figure 4.12: Pump spectra at different repetition rates, $0.05nm$ resolution.

of the output spectra separation. The first Stokes emission spectra were not possible to be obtained due to the corrupted data file.

The Stokes shift from pump wavelength of $1081.8nm$ to the peak emission of the second Stokes at $30kHz$ was $2 \times 1333.5 \pm 1.5cm^{-1}$ and to the middle peak in $150kHz$ spectrum was $2 \times 1330.1 \pm 1cm^{-1}$, where the error comes from the wavelength accuracy and resolution. This is reasonably close to the $1332.9cm^{-1}$ literature reported value[63].

As mentioned before, an additional point to be addressed is the multiple peaks in the second Stokes spectra. Peaks are separated from the center peak by $0.06nm$ or $7.8GHz$ in $30kHz$ case and $0.07nm$ or $9.6GHz$ in $150kHz$ case. Additionally, some features in the $150kHz$ spectrum are split by $0.02nm$ or $3GHz$.

There are two possible mechanisms that could explain these. Firstly, the peaks could be caused by a Brillouin scattering in diamond which is scattering off acoustic frequency phonons. This phenomena is very similar to the Raman scattering although instead of pump wave interacting with the crystal lattice vibrations, it interacts with the pressure (sound) waves travelling in the crystal and undergoing scattering process. Following works presented in [167, 168], at $1.5\mu m$, the Brillouin peaks should be separated by $0.5nm$ which makes this explanation unlikely.

Figure 4.13: DRL output emission at a wavelength of above $1.5\mu m$.

Secondly, the peaks in the output spectra might arise from etalon effects from optical elements in the set up. The etalon effect is a phenomena where transmission through an optical element with two surfaces (e.g. glass plate) is a periodic function of wavelength with modulation depth and period depends on the reflectivity and separation of the surfaces. The period of the transmission function follows equation for the free spectral range (FSR) $FSR = \frac{c}{2L_{opt}}$, where L_{opt} is an optical length of the optical element between the surfaces and c is a speed of light. For the DRL cavity with a $4mm$ diamond, the optical length would be about $L_{opt} = 1.7cm$ which corresponds to $\frac{c}{2L_{opt}} = 8.4GHz$. This modulation in output emission spectra is then very likely to come from the DRL cavity free spectral range. It needs reminding, that the $30kHz$ and $150kHz$ data were recorded after rebuilding the DRL setup hence the difference in the exact peak separation in the emission spectra. In the case of scanning LIDAR, multiple peaks in the spectrum are not seen as a problem, but for a Doppler based LIDAR, multiple peaks might make it very difficult to assess the frequency shift of the

back scattered light.

4.5.2 Unpolarized pump emission

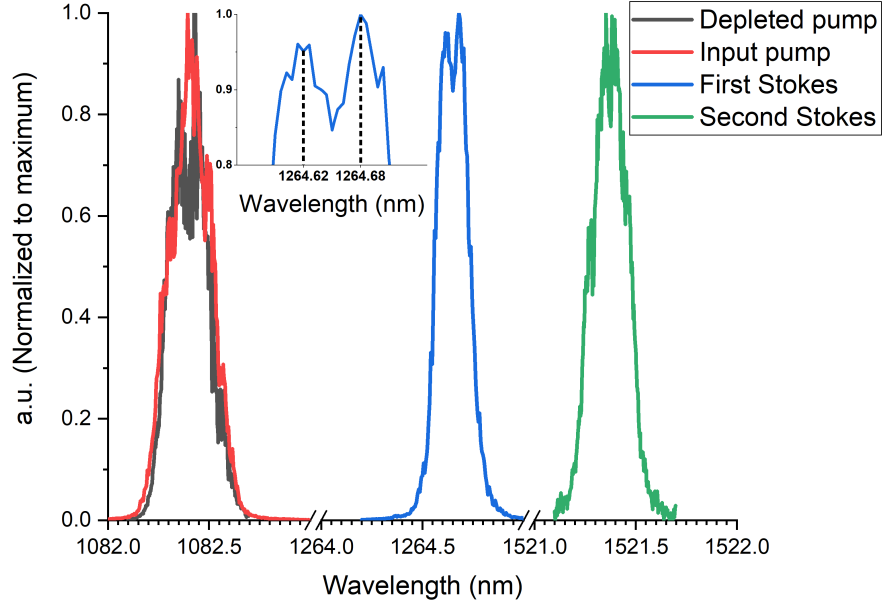


Figure 4.14: DRL emission spectrum pumped by 85W of unpolarized MOPA spectrum, first and second Stokes at 1264nm and 1521nm respectively.

Figure 4.14 shows emission spectra of the pump at 1082.4nm, first Stokes at 1264.65nm and second Stokes at 1521.4nm in case of 150kHz pumping with 85W of average power in the unpolarized MOPA output. The spectra were recorded with OSA ANDO AQ-6315E with 0.05nm resolution. The depletion of the pump spectrum was discussed in Section 4.4. The first Stokes and second Stokes peaks are separated by $1331 \pm 0.4 \text{ cm}^{-1}$. This is reasonably close to the theoretical value of the Raman shift in diamond (1332 cm^{-1} [3]).

The pump linewidth in this case was $FWHM = 0.25 \text{ nm}$, the first Stokes $FWHM = 0.17 \text{ nm}$ and the second Stokes $FWHM = 0.21 \text{ nm}$ all of which are within the resolution margin of the instrument and no broadening of the pump or first Stokes spectra are evident. It needs reminding, that the spectra were averaged over many pulses as well as the scanning time.

The inset in Figure 4.14 shows evidence of two emission peak in the vicinity of

1264.65nm separated by 0.06nm or about 11GHz which is equivalent to an etalon effect in a cavity of 1.4cm optical length and taking into account the uncertainties, it is consistent with the DRL cavity free spectral range.

4.6 DRL emission spectra summary

In the previous Sections spectra from an Yb pumped DRL were presented. In both cases – polarized and unpolarized (multimode) case, the obtained output wavelength was above 1.5 μ m which makes this system adequate for LIDAR applications based on an eye-safe laser sources. The depleted and undepleted pump spectrum in the unpolarized pumping of the DRL case showed, that it might be possible to improve the efficiency of the DRL by narrowing the MOPA linewidth since there is a sign of a spectral hole in the MOPA depleted spectrum. Narrowing of the MOPA linewidth proved not to be an easy task; there were concerns about stimulated Brillouin scattering causing damage to the fiber and a careful real-time monitoring of the MOPA output spectra needs to be developed when narrowing the linewidth.

In the next section, power transfers are presented in case of cooled and uncooled diamond mount when using the unpolarized pump. Using the DRL without cooling certainly is an attractive option for a simple setup but it has to be seen what is being sacrificed in terms of performance. In the further section, the MOPA system was pushed to the highest average power $\approx 95W$ limited only by the time constraints of the measurement. The power transfer of the DRL when pumped with the polarized configuration MOPA is presented after. It needs reminding, that the time spent with the multimode MOPA pumped DRL was only a week and its performance is expected to be improved significantly given more time for alignment and learning this configuration of the MOPA system.

4.7 Multimode Yb fibre pumped DRL performance

In this Section, rather than looking at the emission spectra, a focus is put on the power and energy transfers obtained from the DRL in both unpolarized multimode and

polarized pumping configurations.

4.7.1 Pump focusing and DRL cavity

The DRL cavity in this experiment consisted of the plane input coupler (HR at first and second Stokes, HT at pump wavelength), 7mm diamond and the $ROC = 50mm$ output coupler (HR at pump and first Stokes wavelengths) with $PR = 30\%$ partial reflectivity at $1.5\mu m$ wavelength. The focusing lens was $f = 50mm$ which resulted in a pump spot diameter of about $120\mu m$ which was centered in the middle of the diamond. The detailed description of beam focusing and a beam profile at the focus can be found in Section 4.2.2

4.7.2 Impact of cooling of the DRL diamond mount

The diamond crystal in the DRL cavity was attached to the brass piece with a thermal glue. The piece had water connectors for active cooling as seen in Figure 4.15. Further in the text, cooled diamond will refer to when the water was being pumped through the mount and uncooled when there was no water flow through the piece. Other three faces of the diamond were in the air and were not actively cooled. The measurements of the thermocouple are presented in the Section 4.7.3.

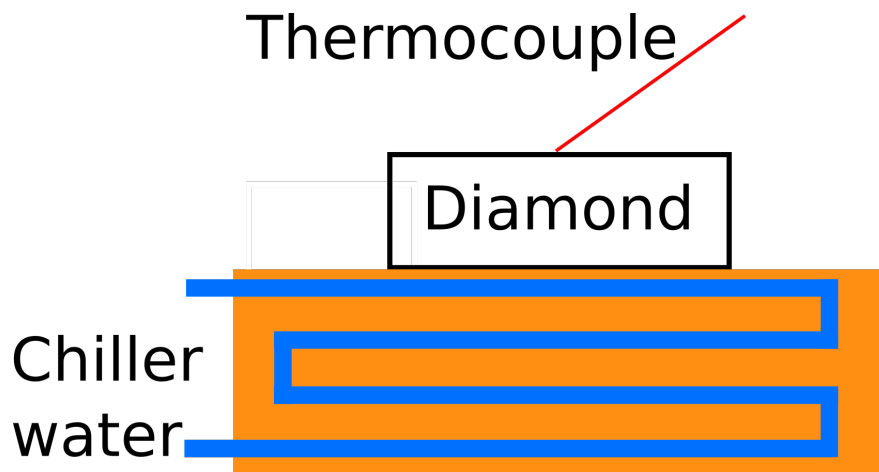


Figure 4.15: Cooling arrangement of the diamond. Diamond rests on the brass mount chilled with water. Thermocouple attached to the surface of the diamond.

Firstly, two preliminary power transfers were measured in which a cooled (The

cooling water was 15°C) and uncooled diamond was used. Figure 4.16 shows these power transfers. The maximum average power in the DRL output was about 5W in both cases although the slope efficiency was improved from 16% to 28% for the same DRL configuration after cooling was applied. The threshold was about 28W for uncooled and 26.5W for cooled case. Both improvements of the threshold and slope efficiency indicate the thermal effects being an issue in the DRL operation. These effects might include mechanical thermal expansion of the brass piece and the stages upon which it was placed impacting the alignment whilst increasing the pump power.

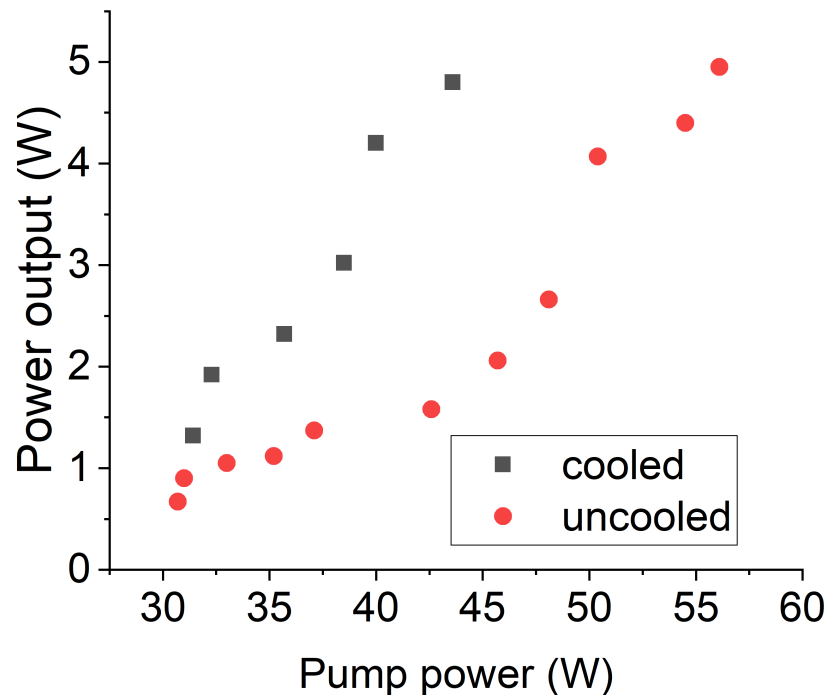


Figure 4.16: Power transfer of the DRL pumped by a multimode Yb fibre MOPA without and with cooling.

4.7.3 Power transfer

After realizing that the cooling of the mount has some important consequences, the DRL cavity was rebuilt to attach a thermocouple with a thermal glue to the diamond surface to measure its temperature.

Figure 4.17 shows the power transfer of the cooled diamond mount DRL at $1.5\mu\text{m}$ when pumped with the unpolarized multimode MOPA laser. The aim of this exper-

iment was to push for the maximum average power of the MOPA. The maximum pump power was about $95W$ at $150kHz$ and $16ns$ pulses with no sign of fiber damage. The maximum output power from the DRL was $12.6W$ corresponding to about $84\mu J$ output pulse energy with a 19% slope efficiency and maximum of 13% conversion efficiency. The threshold was $23.4W$ corresponding to a $172\frac{MW}{cm^2}$ with a pump spot of $4\sigma = 120\mu m$ diameter in the focus, $150kHz$ operation and $16ns$ pulse duration. This particular experiment was performed only once in this configuration (unpolarized multimode Yb fiber) due to the time constraints and the decrease of 9% of the slope efficiency as compared to the previous Section is expected to improve when given more time for the alignment of the laser.

Figure 4.17 also presents obtained temperature readings from the thermocouple. The temperature increases linearly with the input pump power from about $100^\circ C$ at $30W$ to about $250^\circ C$ at $90W$. It has to be added that this measurement could be skewed by scattered $1\mu m$ light interacting with the thermocouple[169]; what is also worth mentioning is that this measurement does not measure the temperature inside of the diamond where the Raman process actually takes place. The measured temperature of the diamond surface was $34.5^\circ C$ when only pump at $30W$ was present and the cavity was misaligned so that the Raman action was not present. After aligning the cavity, with the DRL output at $0.5W$, the temperature of measured by the thermocouple was $49^\circ C$. The background temperature of the diamond without any pumping was $19.2^\circ C$. The temperature increase in the pump only case is a combination of the background small amount of absorption in the diamond at the pump wavelength and scattering of the pump light onto the thermocouple. After the Raman action is initiated, the temperature increases due to the generation of the phonons in the crystal lattice.

Based on the discussion in Section 2.4 and Equation 2.11, for the average pump power of $100W$, $q = 100W \times (1 - \frac{\lambda_p}{\lambda_l}) = 100W \times (\frac{1\mu m}{1.5\mu m})$ quantum defect and focused beam down to $60\mu m$ radius, the expected thermal lens in diamond would be $f = 120mm$. This assumes a CW operation and under a pulsed regime, a question would be if there is enough time for the diamond to cool since it's thermal conductivity is superior to any other laser material as explained in Section 1.3 and 2.4. This is part

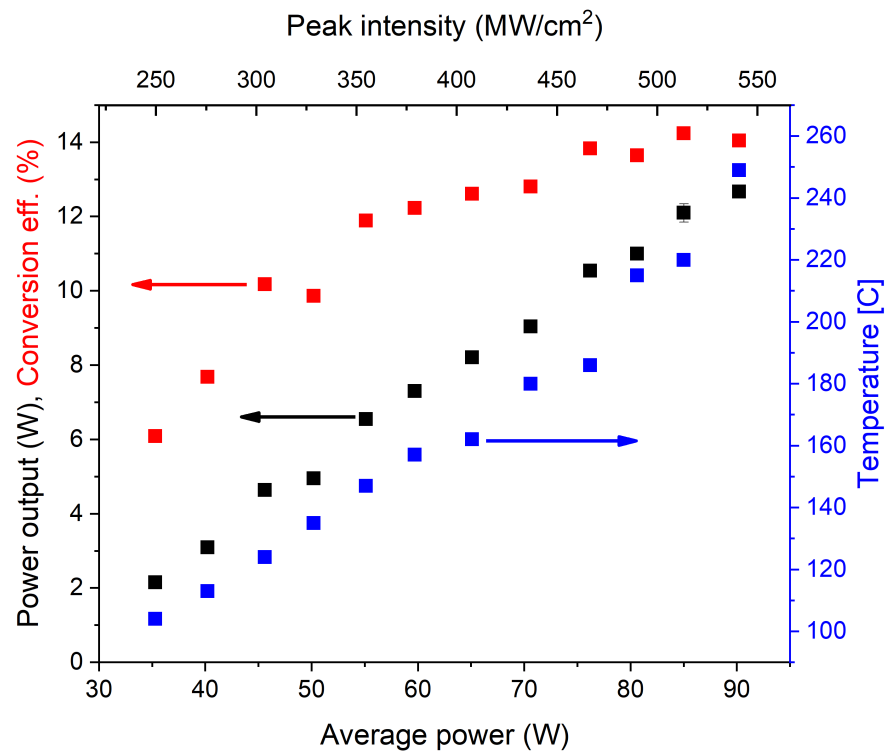


Figure 4.17: Power transfer of the DRL pumped by a multimode Yb fibre MOPA with cooling.

of the ongoing investigation using the finite element analysis simulations and is still to be answered.

4.7.4 Time traces analysis

This Section presents obtained pulse traces from the DRL when pumping with the multimode unpolarized Yb fiber MOPA system. The setup used for these measurements is presented in 4.8. Unfortunately, due to an oversight, the recorded pulses were not synchronized with each other; the pulses are recorded in a random time after the pump pulse and therefore the detailed analysis will not be performed here. The synchronized pulses and therefore a better subject for such analysis are presented in Section 4.8.3, where pulse analysis from the polarized Yb MOPA pumped DRL are presented. Here only the output pulses are shown at first and second Stokes wavelengths with calculated FWHM values.

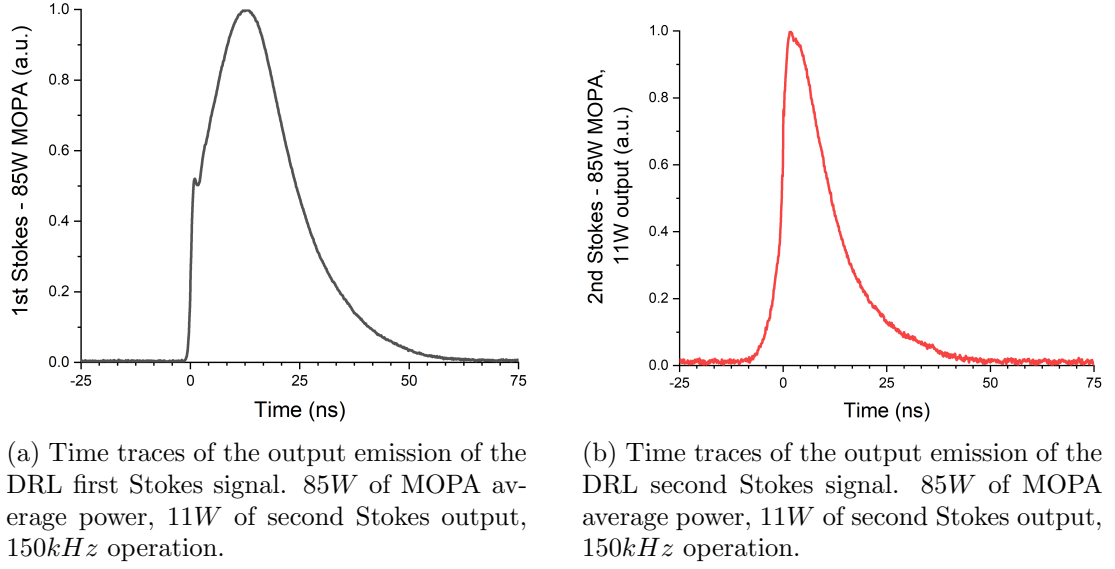


Figure 4.18: Time traces of the output of the unpolarized multimode Yb fiber MOPA pumped DRL.

Figure 4.18 shows output pulses at first and second Stokes wavelengths where the MOPA was operating at 85W average power and about 11W of average power at $1.5\mu m$ was obtained from the DRL. The first Stokes pulse was about $FWHM = 23.4ns$ and the second Stokes $FWHM = 11.9ns$. It has to also be noted that the pulses don't present the mode beating structure as in the case of the Nd:YAP pumping.

Following the discussion in Section 3.6.2, calculated cavity decay time for this DRL cavity, where the optical length (with a 7mm diamond) $L = 26mm$ for first Stokes with $R1 = 0.99$, $R2 = 0.99$ and $T = 0.01\%$ was $\tau_{1s} = 4.3ns$ which is reasonably close to the measured value of the pulse trailing edge $\tau_{1s} = 11ns$. The calculated cavity decay time at the second Stokes for $R1 = 0.99$, $R2 = 0.3$ and $T = 0.01\%$ was $\tau_{2s} = 0.14ns$ and the pulse trailing edge was $\tau_{2s} = 9.6ns$. It is again the argument that the very slowly decaying first Stokes pulse was able to pump the second Stokes field thus prolonging the decay time for this field.

4.8 Polarized Yb fibre pumped DRL performance

This Section presents obtained average powers and pulse energies from polarized Yb MOPA pumped DRL when operating at 30 and 150kHz pulse repetition. As a reminder - the experiments with the MOPA in a polarized configuration were stretched over multiple months with revisiting the setup during visits and both 30kHz and 150kHz data was taken using a DRL setup that was rebuilt multiple times, therefore the direct comparison should be taken with caution. On the other hand, as seen in Section 4.5 that the emission spectra for both repetition rates do not differ substantially and so it is a good sign that these results are somewhat comparable.

4.8.1 Pump focusing and DRL cavity

The DRL cavity consisted of a diamond, plane input coupler (HR at first and second Stokes and HT at pump wavelength) and $PR = 30\%$ at 1.5 μm output coupler (HR at first and pump wavelength). Diamond 3 was used for 30kHz measurements and diamond 5 for 150kHz, both were 4mm (ref. Section 3.4). Although the diamond samples were different, their performance when pumped with Nd:YAP laser in Chapter 3 was the same. The diamond mount was not cooled nor were any other optical elements. The focused beam 4σ width was 180 μm in 150kHz operation regime and 160 μm for 30kHz. The detailed description of the focusing of the beam and its recorded profiles is in Section 4.2.1.

4.8.2 Power transfer

Figure 4.19 shows a power transfer of the Yb MOPA pumped DRL at 30kHz and 150kHz against pump peak intensity and average pump power at a corresponding repetition rate. The peak intensity was calculated as $P_{peak} = \frac{2P_{avg}}{\pi w_r^2 \delta t f_{rep}}$, where the P_{avg} was the average pump power, w_r is Gaussian beam radius (2σ), δt is the pulse duration and f_{rep} is the repetition rate. The pulse duration of the MOPA pulse was $FWHM = 16ns$. The maximum average output power achieved was 9W out of about 41W of pump average power at 150kHz corresponding to about $140 \frac{MW}{cm^2}$ pump peak

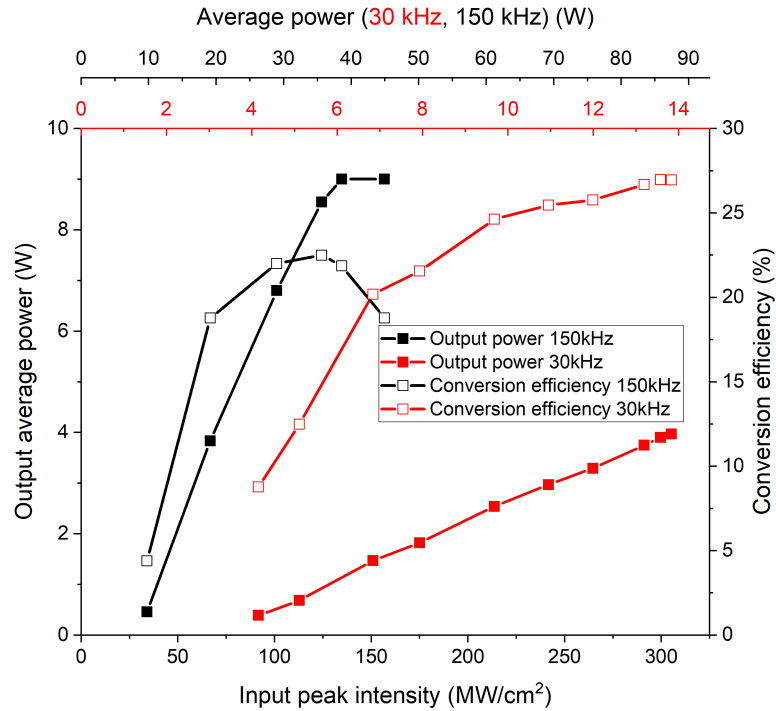


Figure 4.19: Yb fibre pumped DRL power performance at different repetition rates.

intensity with a $180\mu\text{m}$ pump spot diameter. The threshold was about $28\frac{\text{MW}}{\text{cm}^2}$. The roll-over characteristic comes from the damage to the fifth stage fiber output at about 50W average output power. The roll-off seen before this point might have been a result of the degrading of the fiber output before it failed.

In the 30kHz case, since the repetition rate was 5 times lower, the maximum output average power at $1.5\mu\text{m}$ was about 4W out of about 14.5W of pump average power corresponding to about $300\frac{\text{MW}}{\text{cm}^2}$ with $160\mu\text{m}$ pump spot diameter. The threshold was about $66.8\frac{\text{MW}}{\text{cm}^2}$.

As the pulse duration in both 30kHz and 150kHz was the same, the difference in the threshold comes mainly from the $20\mu\text{m}$ difference in the pump beam diameter, but also in about $20\mu\text{J}$ higher pump pulse energy at the threshold in 30kHz case. The safest assumption would be that the higher threshold is a combination of alignment and the beam size. It also has to be noted, that the 30kHz experiments were done in the very first visits in Southampton and the main goal was to move into the high

repetition rate territory as soon as possible. As the experiments with the polarized Yb fiber MOPA pumping yielded the highest achieved output energy, the energy transfer is presented next.

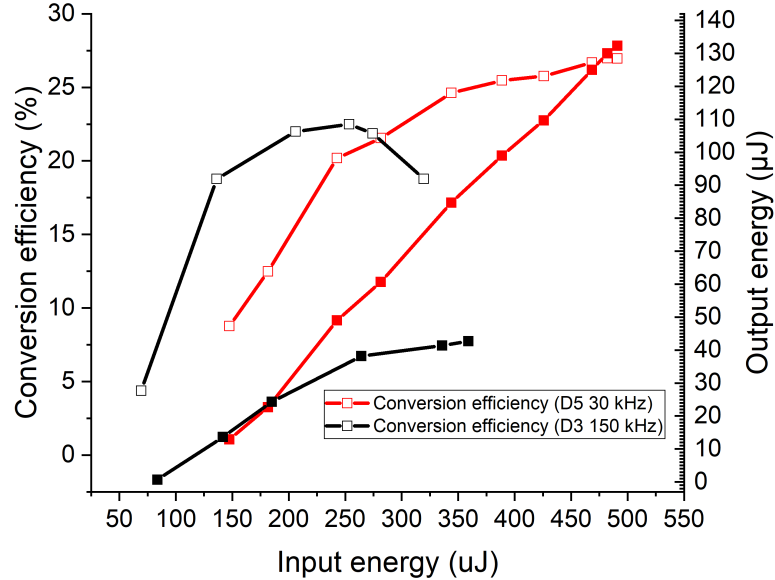


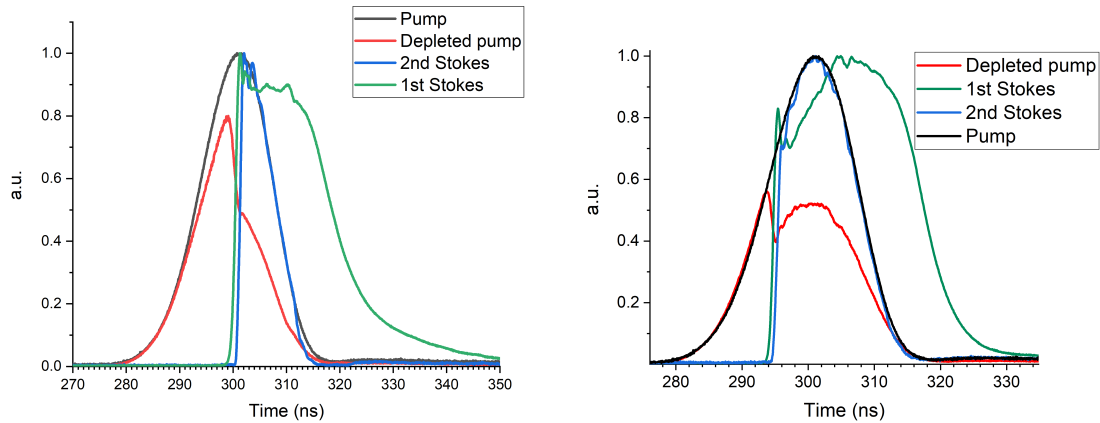
Figure 4.20: Yb fibre pumped DRL energy performance at different repetition rates. D5 - diamond sample 5, D3 - diamond sample 3.

Figure 4.20 shows an energy transfer of the DRL based on recalculating the data in Figure 4.19. The input and output energy were calculated by measuring the average power of the pump and output $1.5\mu\text{m}$ DRL beam and dividing the value by the repetition rate. The output energy in the 30kHz case follows an expected linear increase and the maximum output energy achieved was $130\mu\text{J}$ at $1.5\mu\text{m}$ with the conversion efficiency of 27% out of about $480\mu\text{J}$ of pump. The slope efficiency was about 35% and the conversion efficiency curve shows saturation at around maximum pump energy not showing signs of a roll-off. The threshold was about $108\mu\text{J}$ of pump pulse energy.

In the 150kHz case, maximum output energy was about $43\mu\text{J}$ from pump pulse energy of $375\mu\text{J}$ with the conversion efficiency of 22.5%. It can be seen that in 150kHz , the energy plateaus and rolls-off already at a $250\mu\text{J}$ pump energy which was previously explained by a damage to the fiber end. The slope efficiency of the first three measurement points had a 23% slope efficiency. The threshold was about $81\mu\text{J}$ of pump energy.

4.8.3 Time trace analysis

The time traces were recorded with the setup shown in Figure 4.8 where the trigger for the oscilloscope was the MOPA seed AOM trigger. As mentioned before, the pulses were filtered through a monochromator which provided a neat way to observe a particular pulse at a wavelength of interest. It needs reminding, that during the operation of the DRL, there are three distinct wavelengths in the DRL emitted beam; depleted pump leakage, first and second Stokes and when the DRL is not in operation (e.g. misaligned cavity) non-depleted pump leakage can be observed. The depleted and non depleted pump spectrum was described in earlier sections but here temporal signals of each are observed. The evolution of the pulses follows the same reasoning as explained in Section 3.6.2 and here only comment on the absolute pulse durations will be made and how the cavity decay time compares to the trailing edges of the pulses.



(a) Time traces of the output emission of the MOPA pumped DRL. 43.7W of MOPA average power, 6W of second Stokes output, 150kHz operation. Inset shows logarithmic decay of first Stokes signal.

(b) Time traces of the output emission of the MOPA pumped DRL. 10W of MOPA average power, 2.5W of second Stokes output, 30kHz operation.

Figure 4.21: Time traces of a MOPA pumped DRL at different operating conditions.

Figure 4.21a shows obtained pulse traces for different repetition rates of the MOPA and hence the average power. It has to be added that these results were obtained in the space of couple months and direct comparison might be difficult. Figure 4.21a shows time traces recorded at 150kHz repetition rate, 43.7W of MOPA average power and about 6W of the second Stokes output at $1.5\mu\text{m}$. The full-width half-maximum of a

pump pulse was $FWHM = 15ns$ and the second Stokes pulse was about $FWHM = 7ns$. The first Stokes was $FWHM = 17ns$. Following equation for the cavity decay time, $\tau = \frac{-2L}{c \ln(R1 * R2 * (1 - T)^2)}$ [40], the measured first Stokes pulse decay was $\tau_{1s} = 7ns$ which for $R1 = 0.99$, $R2 = 0.99$ and optical cavity length $L = 22mm$ corresponds to about $T = 0.01\%$ additional loss in the cavity which for a very high Q factor cavity is possible. For the second Stokes, measured decay time was about $\tau_{2s} = 1.45ns$. The calculated value for τ_{2s} with $R1 = 0.99$, $R2 = 0.3$ and $T = 0.01\%$ corresponds to is $0.1ns$. This order of magnitude difference can not be offset by increasing the T losses since the value for τ_{2s} would further decrease not increase. This is exactly what was observed in the Chapter 3 in a case of Nd:YAP pumping. It was assumed that since the first Stokes pulse is much longer than the second Stokes pulse, it can be, that the first Stokes field, even in its decay part of the pulse is still strong enough to pump the second Stokes field - increasing its pulse duration beyond the cavity decay time. Similarly a long decay time of a couple of ns for the second Stokes pulse was observed e.g. in [38], where the OC at the second Stokes wavelength was $PR = 16\%$.

In the case of $30kHz$ operation with $10W$ of pump average power and about $2.5W$ of second Stokes average power output, the second Stokes pulse was about $FWHM = 11ns$ with the first Stokes pulse of $FWHM = 20ns$. The cavity decay time reasoning follows the same argument as in a previous paragraph. Third Stokes signal was not observed in either case.

4.9 Yb fiber pumped DRL summary

This Section is aimed to (i) gather all the information presented in this Chapter in a form of a useful Table 4.1 (ii) follow up on the arguments made along the Chapter.

4.9.1 Summary table

| MOPA configuration | Unpolarized 150kHz | Polarized 150kHz | Polarized 30kHz |
|-------------------------------|-----------------------|----------------------|----------------------|
| Pump λ | 1082.4nm | 1081.9nm | |
| Pump $\Delta\lambda$ | 0.25nm | 0.13nm | |
| Pump pulse duration | 15.5ns | | |
| Second Stokes λ | 1521.4nm | 1518.9nm | 1520.5nm |
| Second Stokes $\Delta\lambda$ | 0.21nm | 0.02nm (1) | 0.03nm (1) |
| Second Stokes pulse duration | 11.9ns | 7ns | 11ns |
| Max energy | 86.6 μ J | 40 μ J | 132 μ J |
| Max average power | 13W | 9W | 4W |
| Max conversion efficiency | 13% | 22.5% | 27% |
| Max slope efficiency | 28% | 23% | 35% |
| Peak intensity at threshold | 176 $\frac{MW}{cm^2}$ | 28 $\frac{MW}{cm^2}$ | 71 $\frac{MW}{cm^2}$ |

Table 4.1: Summary of all the important parameters achieved in the Yb MOPA pumped DRL experiments. (1) This number represents the FWHM value of the highest peak in the emission spectrum in the Figure 4.13.

4.9.2 Summary discussion

The Yb fiber MOPA pumped DRL proved to be a viable option to reach high powers at high repetition rates at eye-safe wavelengths. The experimental results should be treated as an exploration of possible ways to evolve the system. Initial requirements put on the MOPA system of polarized emission with a close to $M^2 = 1$ beam quality seemed to be also a limitation to the MOPA system reliability. Changing the fiber to a much more reliable multimode fiber allowed the system to work over an extended period of time with no sign of damage. The unpolarized emission also simplified the DRL conditioning optics setup by removing the attenuator (PBS and half-wave plate) and a polarization controlling half-wave plate. The measurements of the DRL output beam quality are not presented in this work, however, further experiments utilizing the DRL

pumped by unpolarized MOPA system have been performed. One such experiment conducted at the time of writing by Dr Giorgos Dimitriou demonstrated that pumping the DRL with the $M^2 = 5.6$ unpolarized MOPA beam resulted in the $M^2 = 1.2$ of the DRL output beam.

The maximum energy when pumping with the polarized MOPA emission was achieved when using a lower repetition rate of $30kHz$ compared to $150kHz$ although this was most likely due to the damage to the MOPA fifth amplification stage fiber. In the unpolarized pumping case, the cooling of the diamond showed some improvement in the DRL output and in the future, a new mount is going to be produced which will allow cooling all the sides of the diamond crystal, not only the bottom side.

The maximum average output power of $13W$ at $1.5\mu m$ was achieved at $150kHz$ when pumping with unpolarized MOPA emission. As mentioned in the first paragraph, even though this value was obtained at $85W$ of MOPA average output power compared to $9W$ at $1.5\mu m$ when pumping with $56W$ of average power polarized light, the improvement in reliability of the system makes up for the much higher pump power that had to be used. The improvements are expected with further optimisation of the alignment, making the choice for unpolarized pumping much more appealing.

The disadvantage of using the unpolarized approach is that for the same DRL output power at $1.5\mu m$ of $9W$, the peak intensity required for the multimode pump source was 2.7 times higher than the polarized pump source. It is a combination of a different beam quality impacting the confocal parameter of the pump, possible spectral hole burning in the unpolarized case, dependency of the Raman gain on the polarization and of course differences in alignment which is believed will improve the unpolarized pumped DRL results.

The observed differences in the Raman laser threshold in case of unpolarized and polarized pumping could be a sum of influences of the broader emission of the multimode unpolarized MOPA, undefined polarization and worse beam quality not to mention a limited time with the system. The threshold for the DRL in case of the polarized pump of $0.13nm$ linewidth at $150kHz$ was $28\frac{MW}{cm^2}$ and $172\frac{MW}{cm^2}$ with a $0.25nm$ linewidth in case of unpolarized pumping. Assuming that the Raman gain bandwidth is equal to

the spectral hole of $0.08nm$ shown in the depleted spectrum of the unpolarized pump and the pump linewidth is $0.25nm$, the threshold following Equation 1.5 should be about $1.6\times$ higher than in the case of polarized pumping with $0.13nm$ linewidth compared to the measured $6\times$. Following work in [79] it can be seen, that the Raman laser threshold for the unpolarized pumping is about 20% higher than when the pump is polarized along the $\langle 111 \rangle$ crystallographic direction of the diamond crystal. This indicates, that indeed not only the broader spectrum of the unpolarized pump and polarization influences the higher threshold peak intensity. It has to be reminded, that tighter focusing would bring the DRL closer to the optimum of operation as described previously.

This Section concludes the Yb fiber pumped DRL and leads to a short Chapter of an alternative way of achieving the eye-safe wavelength with DRL. This Chapter presented a diamond Raman laser whereas in the next one, a diamond Raman MOPA will be presented. This means that the $1.5\mu m$ light originating from a low power seed (e.g. Er doped fiber amplifier) is transmitted through a diamond Raman based amplifier with a high intensity oscillating at the first Stokes providing gain for the second Stokes wavelength which the seed is tuned to.

Chapter 5

Diamond Raman amplifier

In this chapter a proof of concept diamond Raman amplifier operating at an eye-safe wavelength is presented. The advantage of the amplifier over the laser oscillator configuration discussed so far in this thesis is that the amplifier emission usually inherits characteristics of the seed laser. This is an attractive option for amplification of narrow linewidth sources. An example of a conventional amplifier exhibiting narrow linewidth emission is work presented in [170], where a $13kHz$ laser diode seeded a chain of fiber based amplifiers resulting in above $80W$ of CW emission at $1552nm$. Narrow linewidth sources operating at eye-safe wavelength are important for Doppler LIDAR technologies where the wind speed measurement resolution is proportional to the laser source linewidth [18]. The diamond Raman amplifier seeded by a narrow linewidth laser diode is one of the potential approaches towards developing such a source. To the knowledge of the author, no bulk solid-state Raman amplifier based on a first Stokes Raman oscillator has been reported and the literature only shows gas based Raman amplifiers e.g. in [133] and waveguide based e.g. in [171]. The amplifier presented in this chapter is a second order Stokes amplifier and other multiple order Raman based amplifiers were reported e.g. in [172] where a germanosilicate fiber pumped with a $1064\mu m$ pump provided an amplification at a third Stokes shift for a $1.3\mu m$ seed laser signal. It has to be added that amplification at the first Stokes wavelength in bulk material was reported previously e.g. in [173] for silicon, [174, 175] for diamond and [176] in glass in a pump-probe based experiments.

It needs reminding, that due to the time constraints, the work presented in this chapter should be looked at only as a proof of concept which aims to demonstrate amplification of the eye-safe wavelength light in diamond. The next section outlines the principle of operation of a diamond second Stokes Raman amplifier based on a first Stokes oscillator. The following section shows the experimental setup developed for the purpose of demonstrating Raman amplification in diamond. Next a description of challenges in spatial, spectral and temporal alignment is presented. The effect of jitter in the Nd:YAP pump laser on the amplification is described followed by measurement of the diamond Raman amplification versus the seed pulse energy.

5.1 Raman amplifier principle of operation

In this section a diagram showing a working principle of amplification of the eye-safe wavelength seed laser in a first Stokes diamond Raman oscillator is presented. The sections following this one experimentally prove this principle.

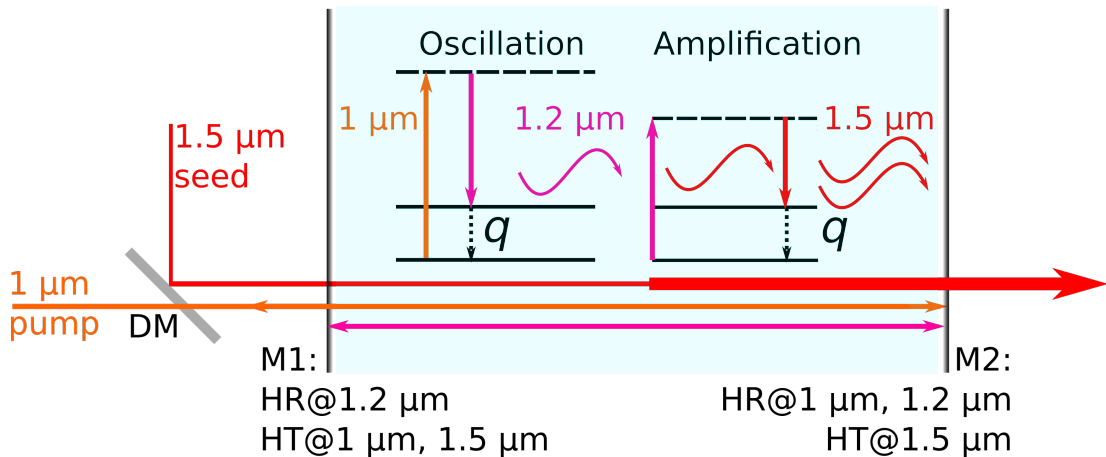


Figure 5.1: Amplification process of a $1.5\mu\text{m}$ seed laser in a diamond Raman amplifier. Blue area - diamond, M1, M2 - input and output couplers, HR - highly reflective, HT - highly transmissive, DM - dichroic mirror, q - diamond phonon energy.

Figure 5.1 shows a proof of concept diamond Raman amplifier. The diamond (blue area) is placed in between two mirrors - M1 highly reflective at the first Stokes wavelength of $1.2\mu\text{m}$ and highly transmissive at $1\mu\text{m}$ pump and $1.5\mu\text{m}$ second Stokes wavelengths and M2 - highly reflective at pump and first Stokes wavelengths and highly

transmissive at second Stokes wavelength. This configuration creates a diamond Raman oscillator in which a double passed external pump at $1\mu m$ drives the intracavity first Stokes field. This field is mainly kept inside of the cavity since the only loss of the first Stokes field would come from unwanted scattering, absorption and coatings imperfections. The cavity is not resonant at the second Stokes wavelength and, in the absence of the seed, any second Stokes signal in the laser output is expected to originate from spontaneous Raman scattering or stimulated Raman scattering occurring from the feedback of imperfect anti-reflective coatings.

The working principle of the setup in Figure 5.1 is as follows: (1) a pump beam at $1\mu m$ (orange color) goes through a dichroic mirror (DM) and M1 mirror into a diamond crystal (blue area). The pumping process of the first Stokes intracavity laser field is indicated by the energy diagram labeled "Oscillation". It can be seen that a pump photon at $1\mu m$ (orange color) interacts with a phonon q contributing to the emission of $1.2\mu m$ photons (purple color) that start the lasing action at this wavelength. As the M1 and M2 mirrors are highly reflective at first Stokes wavelength, the majority of this laser field is contained within the resonator. (2) The first Stokes intracavity field is then acting as a pump, which in turn allows for amplification of the externally injected photons at the second Stokes wavelength at $1.5\mu m$. As the resonator is non resonant at the second Stokes wavelength, the threshold for stimulated scattering at $1.5\mu m$ without supplying the external field is very high. Spontaneous scattering occurs in addition as well contributing to a loss of the available amplification. (3) The external photons are indicated in Figure 5.1 as a seed laser beam at $1.5\mu m$ (red color) which is reflected off the dichroic mirror and transmitted collinearly with the pump beam through the diamond crystal. The seed laser photon indicated by a red wave in the "Amplification" diagram then starts the stimulated Raman scattering process resulting in two photons (two red waves) at $1.5\mu m$. Therefore, the seed laser beam is amplified by an amplification factor equal to the ratio of the seed laser power at the resonator output with the pump beam turned on, to the seed laser power with the pump beam turned off.

This section described the processes taking place in the first Stokes diamond Raman

oscillator allowing for amplification of the second Stokes wavelength supplied by the external laser. The next section presents a setup used in the experiments in detail - an external seed laser, diamond Raman amplifier and analysis equipment.

5.2 Setup

Figure 5.2 shows an overview schematic of the setup used for amplification in the diamond Raman amplifier. The system can be divided into two parts indicated with a green and pink colors. The pink color shows the seed laser (master oscillator): a distributed feedback (DFB) laser diode (Eblana) pre-amplified by an erbium doped fiber amplifier (EDFA). The green area shows the diamond Raman amplifier exactly as one described in section 5.1 with the Nd:YAP laser being a $1\mu m$ pump. The blue section shows the diagnostic setup which was previously shown in Chapter 3 in Figure 3.20. To summarize, this analysis system allowed for the recording of diamond amplifier output pulses at different wavelengths set by the monochromator. It was also possible to record optical spectra using OSA205 (Thorlabs) in CW and pulsed mode due to the relatively long pulses of the DFB diode laser pulses.

In the next subsection a description of the components used in this particular diamond Raman oscillator (power amplifier) is presented. The following subsection will talk through the seed laser consisting of the Eblana DFB diode laser and an EDFA pre-amplifier.

5.2.1 Diamond Raman amplifier

The description of the diamond amplifier (green area in Figure 5.2) is now presented.

The amplifier consisted of a Raman cavity with a $4mm$ diamond crystal. The cavity had a plane input coupler and a $ROC = 50mm$ output coupler which both were highly reflective ($> 99.9\%$) at the first Stokes and non reflective ($< 0.2\%$) at the second Stokes wavelength. The output coupler was highly reflective at the pump wavelength for double passing. The cavity was pumped with the Nd:YAP laser previously described in

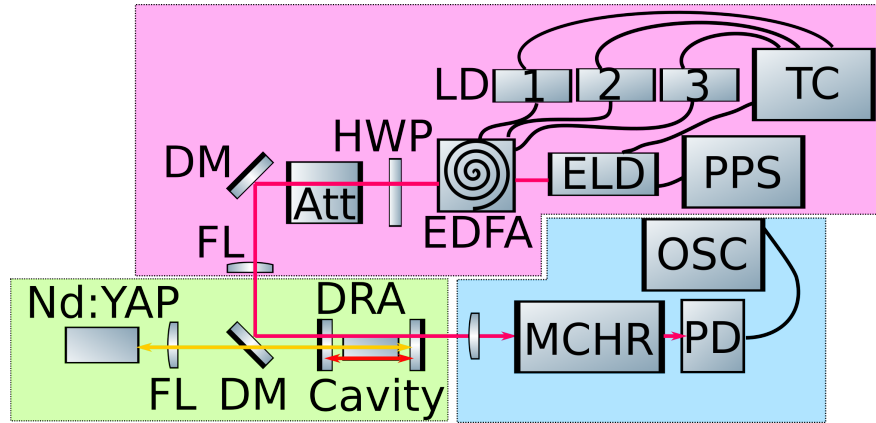


Figure 5.2: Schematic for the diamond MOPA system. Green area - diamond Raman amplifier. Pink area - Er-doped fibre amplified distributed feedback diode (DFB) seed laser. Blue area - analysis system. Nd:YAP - pump source, FL - focusing lens, HWP - halfwave plate, Att - attenuator, DM - dichroic mirror (HR at $1.5\mu\text{m}$, HT at $1\mu\text{m}$), DRA - diamond Raman amplifier, MCHR - monochromator, PD - photodiode (Thorlabs, 350MHz), OSC - oscilloscope, EDFA - erbium doped fiber amplifier, LD1,2,3 - pump diodes for EDFA, ELD - narrow linewidth Eblana DFB laser diode, PPS - pulsed power source, TC - temperature controller.

Chapter 3 with the same conditioning optics system with an additional dichroic mirror (DM) placed after the focusing lens to allow for the injection of the seed laser into the Raman cavity. It has to be mentioned here, that the amplification process described in section 5.1 requires that the seed laser and the pump laser second Stokes wavelengths are the same (as well as the seed laser linewidth to be narrower than the gain bandwidth in diamond of 2cm^{-1} or about 0.4nm at $1.5\mu\text{m}$). In the case of this experiment, the peak of the Raman gain was fixed at the second Stokes shift from the $1.079\mu\text{m}$ Nd:YAP emission which was about $1.514\mu\text{m}$.

The mode size of the first Stokes field was about $185\mu\text{m}$ (from ABCD matrix method) in diameter and the pump was focused to a measured $144\mu\text{m}$ diameter (both 4σ width). The intracavity intensity was not quantified due to a difficulty of measuring of the output light from a high Q cavity. The threshold for the first Stokes field detection in the Raman cavity output was about $120\mu\text{J}$ of Nd:YAP pulse energy. Nd:YAP had the same settings as described in Chapter 3 - 20Hz repetition, 20ns pulse duration. This means that the intracavity first Stokes field and therefore the condition for amplification at the second Stokes wavelength was also pulsed.

Despite the Raman cavity not being resonant at the second Stokes wavelength, as soon as the first Stokes intracavity pulse became stable in amplitude at about $150\mu J$ Nd:YAP pulse energy, second Stokes stimulated or spontaneous scattering reached its threshold causing the amplifier to emit at the second Stokes wavelength. It is possible that this emission was caused either by self-lasing of the amplifier (stimulated Raman scattering) or spontaneous Raman scattering and both these phenomena will be called parasitic second Stokes emission. This parasitic emission decreases the amplification factor in the diamond Raman amplifier by depleting pump signal. The next subsection presents the results of a simulation of the first Stokes intracavity field energy in a case of no parasitic emission at second Stokes compared to when it is present taking the experimental setup as an example.

5.2.2 Impact of the parasitic emission at second Stokes wavelength on the amplification factor

The first Stokes intracavity field acts as a pump for the amplification process for the seed laser. The amplification factor depends then on the first Stokes field strength. Losses to this field decrease the amplification factor and one of the mechanisms of such loss is energy transfer between the first Stokes field to the second Stokes field. In the absence of the parasitic emission at the second Stokes wavelength, the first Stokes field intracavity energy and therefore the amplification factor of the seed laser is expected to be the highest.

The simulation in this subsection aims to compare two numbers - energy of the first Stokes intracavity field in the absence of the parasitic second Stokes field (spontaneous and stimulated Raman scattering), and energy of the first Stokes intracavity field energy in the presence of the parasitic second Stokes intracavity field. The first case was simulated using the model described in Chapter 2 and setting all the parameters that contribute to the generation of the second Stokes field to zero whilst the latter case was simulated with the parameters equal to the experimental values. The parameters as well as the intracavity energy of the first Stokes field are presented in Table 5.1. The pump for the simulation was the Nd:YAP laser pulse of an energy of $400\mu J$, $\Delta t = 20ns$

duration and $20Hz$ repetition rate, which the peak power is $P_{peak} = \frac{E}{\Delta t} = 20kW$. It can be seen, that the potential intracavity first Stokes field peak power without the second Stokes field present is equal to $2.06MW$, where the simulated first Stokes pulse duration is $35ns$, compared to the $12kW$ when the second Stokes field is present. The model does not include the amplification process described in section 5.1 therefore the direct comparison of the amplification factor of the seed laser for the two cases is not possible and the conclusion is only indicating that to reach the maximum potential amplification factor, the second Stokes intracavity field should be minimized by introducing losses at the second Stokes wavelength in the diamond Raman cavity.

| Stokes order | Input coupler PR % | Output coupler PR % | Diamond input surface PR % | Diamond output surface PR % | K_{sp} quantum noise $\frac{1}{m}$ | Intracavity pulse peak power |
|--------------|--------------------|---------------------|----------------------------|-----------------------------|--------------------------------------|------------------------------|
| 1 | 99 | 99 | 0 | 0 | 10^{-9}^m | $2.06MW$ |
| 2 | 0 | 0 | 0 | 0 | 0 | 0 |
| 1 | 99 | 99 | 4 | 4 | 10^{-9} | $12kW$ |
| 2 | 2 | 2 | 3 | 2 | 10^{-9} | $4kW$ |

Table 5.1: Intracavity pulse energy for first and second Stokes depending on the coatings partial reflectivity PR. Pump pulse peak power $P_{peak} = 20kW$.

5.2.3 Seed laser

The seed laser for the diamond amplifier is shown in Figure 5.2 in the pink area. It consisted of a master oscillator indicated as ELD - DFB laser diode (Eblana, threshold about $30mA$, maximum $15mW$ CW, linewidth $< 1.5MHz$, $1.518\mu m$ center wavelength at $25^\circ C$). The center wavelength could be tuned by a temperature controller with a $0.1 \frac{nm}{^\circ C}$ coefficient. The output power was driven by a pulsed low noise power source ($7\mu A$ RMS ripple) and guided through a pigtailed fiber output. The choice of the low noise power source comes from the fact that electrically pumped laser diodes are susceptible to wavelength variation due to current changes and an unstable ELD wavelength could modulate the Raman amplifier gain.

The output from the master oscillator was then fed into an EDFA pre-amplifier developed by collaborators at Southampton University and since it is not a part of the

author's work, it will only be described briefly. The choice for using of the Er: fiber was dictated by its amplification bandwidth around $1.5\mu m$. The EDFA consisted of three amplification stages and its gain bandwidth could be tuned with the etalon filter between the first and second stage. The pump for the first amplification stage (LD1) was a DFB laser diode operating at $1468nm$ and two DFB laser diodes (LD 2,3) operating at $1473nm$ for stages two and three. The maximum operating current for all of the diodes was $800mA$ giving about $160mW$ output average power each. In the experiment described in this chapter, the LD1 and 2 were operated at $700mA$ and the LD3 at $500mA$ which was limited by the available laser diode current drivers. The measurements made by the Southampton University team show that from about $50mW$ at the EDFA input, it was possible to get above $200mW$ of $1.5\mu m$ radiation.

5.2.4 Seed laser wavelength tuning

To maximize the seed laser amplification in the process described in Section 5.1, the seed laser emission wavelength has to be tuned to the second Stokes wavelength of the diamond Raman oscillator. The tuning of the seed laser consists of two steps: (1) tuning of the ELD center wavelength using a Peltier temperature controller taking into account ELD operating regime (pulsed, CW) and driving current; and (2) adjusting the peak wavelength of the EDFA gain bandwidth with the etalon to maximize the ELD amplification and therefore the seed laser overall output power leading to a better signal to noise ratio in amplification factor measurements. These steps will be described now: firstly the impact of the operating regime and temperature of the ELD on its output spectrum followed by the adjustment of the EDFA.

Figure 5.3 shows output spectra of the EDFA when pumped with the LD 1,2 and 3 pump currents ($700mA + 700mA + 500mA$) operating in CW regime and seeded by the ELD at different currents and temperatures. Two operating regimes of the ELD are shown - CW and pulsed ($100ns$ pulse duration - limited by the current driver, $20Hz$ repetition rate). The spectra were measured with the OSA205 with the resolution of about $0.3nm$ at $1.5\mu m$ wavelength. Spectra recorded in pulsed mode at $110mA$ ELD current and $37^{\circ}C$ (red curve) and $31.7^{\circ}C$ (blue curve) show that the center wavelength

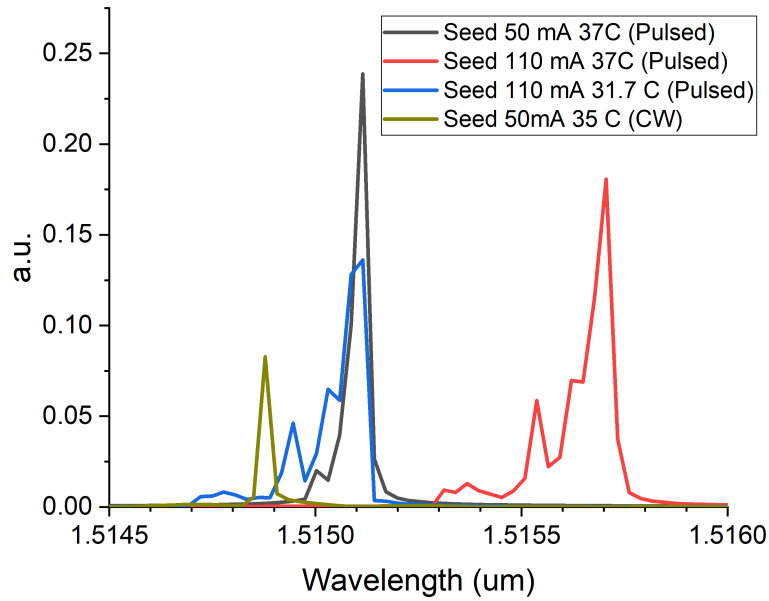


Figure 5.3: Output spectrum of the DRA seed at different ELD operating conditions.

can be tuned by changing the temperature of the ELD controller; the tuning coefficient was about $0.1 \frac{nm}{^{\circ}C}$. Increasing the current in pulsed regime (gray and red curves) from $50mA$ to $110mA$ increases the emission wavelength by about $0.6nm$.

An effect of wavelength variation is also present in the shown spectra. The golden curve shows the output emission in CW regime at $50mA$ operating current. The emission shows a single sharp peak as expected from a narrow linewidth seeded EDFA amplifier. In pulsed mode, shown with a gray curve, where ELD was operated at the same current and very similar temperature, spectrum shows a slight "side peak" at $1.515\mu m$ indicating multiple wavelength operation over the time averaged OSA measurement of about $5s$ needed to scan the spectrum. This side peak is more evident when the current of the seed is increased to $110mA$ as seen in red and blue curves indicating wavelength variation.

One conclusion that arises from this part of the section is that changing the ELD operating regime, current and temperature is going to impact its emission wavelength which will become important in the later part of the section. The second conclusion is that since the gain coefficient in the diamond Raman amplifier is wavelength dependent, the wavelength variation will affect the overall gain of the amplifier. In a later

part of the section an interaction between the EDFA preamplifier gain bandwidth and ELD emission wavelength is shown.

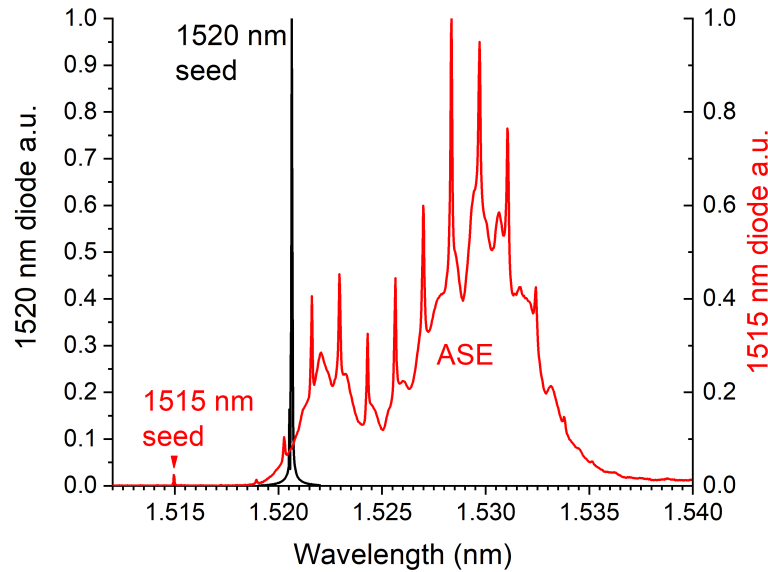


Figure 5.4: Output spectrum of the EDFA when seeding with two different seed wavelengths. EDFA pumps at the maximum available current.

It was mentioned before that the expected wavelength of the second Stokes field in the diamond Raman oscillator is $1.1514\mu\text{m}$ therefore an experiment was designed in which the ELD was operating in the CW regime and its center wavelength was tuned by the temperature controller around this value. Then, the EDFA peak wavelength of the gain bandwidth was adjusted by the etalon to maximize its output power. In case of the gain bandwidth falling outside of the ELD emission, the EDFA output is dominated by amplified spontaneous emission (ASE). To visualize the limit of the EDFA amplification, two EDFA output spectra are shown in Figure 5.4 recorded with OSA205C. ELD had about 6mW of CW output average power and the EDFA was pumped with LD1,2 set to 700mA and LD3 to 500mA . The black curve shows the ELD operating at $1.520\mu\text{m}$ at 25°C and the EDFA etalon was adjusted so that the ELD emission peak was the largest and the noise in the background caused by the ASE from the EDFA was negligible. On the other hand, the red curve spectrum of the ELD operating at a $1.515\mu\text{m}$ wavelength at 25°C and about 6mW output CW average power with the EDFA gain bandwidth not adjusted, shows only a small emission ELD

peak (attenuated by the Er: fiber) and the rest of the spectrum is overwhelmed by the ASE.

Tuning the EDFA etalon as well as ELD center wavelength by a trial and error method, it was found, that $1514.6nm$ was the lowest seed wavelength that it was possible to amplify. At this wavelength of operation, the ASE contributed 28% of the total power in the EDFA output spectrum. This value was calculated from the ratio of the integrated seed laser emission spectrum at $1.5146\mu m$ to the power in the entire EDFA output spectrum integrated over the range between $1.513\mu m$ and $1.537\mu m$.

The constraint of not being able to reach shorter wavelengths in the EDFA output comes from its limited gain bandwidth. A reasonable fix to this issue would be to use a longer wavelength pump for the diamond Raman oscillator shifting the second Stokes wavelength to longer values. The MOPA laser presented in Chapter 4 operating at $1.083\mu m$ would result in a $1.522\mu m$ second Stokes wavelength which is well within the EDFA gain bandwidth.

5.3 Amplification factor measurement method

This section presents a definition of the amplification factor of the diamond Raman amplifier which will be useful for the clarity in the later sections. The operating regimes for the Nd:YAP laser (pump for the first Stokes diamond Raman intracavity field) was pulsed, $20ns$ pulse duration and $20Hz$ repetition rate. The seed laser operated also in the pulsed regime with the pulse duration of $100ns$ limited by the current source. This meant that the seed and the Nd:YAP pulses were mismatched in duration which could be fixed by using a different current driver unavailable at the time of conducting the experiment.

The ELD was synchronized to the Q-switch trigger of the Nd:YAP laser (ref. Section 3.2). The amplification factor was defined as the ratio of the area under a seed laser temporal pulse shape detected by the photodiode in the analysis system when the Nd:YAP laser was operating (amplification condition turned on) to the seed laser area when the Nd:YAP laser was turned off. Averaged amplification factor refers to a ratio

of 64 averaged pulses of the seed laser. An example of 64 averaged seed laser pulses when the Nd:YAP laser is on and off is shown in Figure 5.5. The area ratio between these two averages was 1.08 leading to an 8% average amplification factor. It has to be added that the amplification factor was underestimated since the Nd:YAP pump was not present over 80% of the seed laser pulse duration (seed laser pulse duration - $100ns$, pump pulse duration - $20ns$). To mitigate this, another approach of presenting the instantaneous amplification factor is shown in Section 5.5, comparing only the amplitudes of the amplified and not amplified seed laser pulses. Both approaches of presenting the amplification factor were useful and will be used as appropriate.

It has to be added, that the standard deviation of the pulse areas was estimated by the oscilloscope built in tools as well as recording of the $N = 64$ time traces and calculating the error. The manual calculation of the pulse area was done using Origin software and then the standard deviation of N pulses was calculated as $\sigma = \frac{\Delta A}{\sqrt{N}}$, where ΔA is a standard deviation of the single pulse area [177]. Both methods gave similar results and the standard deviation error of the averaged pulse area was between 1% and 2%. The standard deviation of the averaged amplification ratio is then between 2% and 4%.

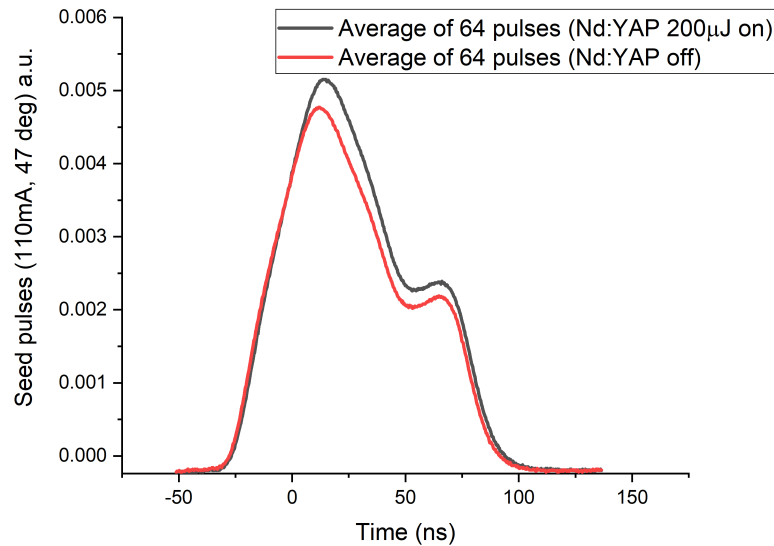


Figure 5.5: Averaged seed laser pulses (ELD at $110mA$ and $47^{\circ}C$) with Nd:YAP on and off.

The parasitic emission of the diamond Raman amplifier is the most significant contribution to the error in the amplification factor measurement. The seed laser and the parasitic emission were not possible to be separated spectrally or spatially, and the parasitic emission was evident as additional spikes at the second Stokes wavelength coming purely from the diamond Raman amplifier. These spikes contributed to the error in calculating the amplified seed laser pulse area and therefore to the amplification factor. The temporary solution was to put an neutral density filter in the analyzing system path, attenuating the parasitic emission spikes below the detection threshold, allowing only the seed laser to be detected.

5.4 Optimization the amplification process

Previous sections presented the principle of operation of the diamond Raman amplifier and the experimental setup. This section outlines the optimization process in terms of spatial, spectral and temporal alignment between seed and pump lasers to maximize the amplification factor.

5.4.1 Spatial overlap

To maximize the amplification of the seed laser in the diamond Raman amplifier, its beam was made collinear with the pump beam over the length of the diamond. This was achieved by placing two apertures - at the Nd:YAP focus point with an opening of $100\mu m$ diameter (Nd:YAP was focused to $144\mu m$ diameter) and another one close to the input of the monochromator. The seed laser beam was then aligned with the Nd:YAP laser beam and it was assumed that the Stokes intracavity field is collinear with the Nd:YAP laser beam. After this spatial alignment, the diamond Raman cavity was built with the center of the diamond in place of the first aperture at the Nd:YAP focal spot.

5.4.2 Spectral tuning

The amplification factor is maximized when the peak emission wavelength of the seed laser is aligned spectrally with the peak of the second Stokes wavelength of the diamond Raman amplifier. This section presents measurements of the averaged amplification factor (ref. section 5.3) versus wavelength of the seed laser to determine its optimal operating condition. The wavelength of the seed laser was adjusted by the temperature controller and the amplification factor was measured at each point. The seed laser emission wavelength was first measured with the OSA205C at two operating points - the 50°C and 30°C in pulsed regime at 110mA ELD current with maximum available EDFA pump currents to create a wavelength scale with a $0.1 \frac{\text{nm}}{^{\circ}\text{C}}$ temperature coefficient.

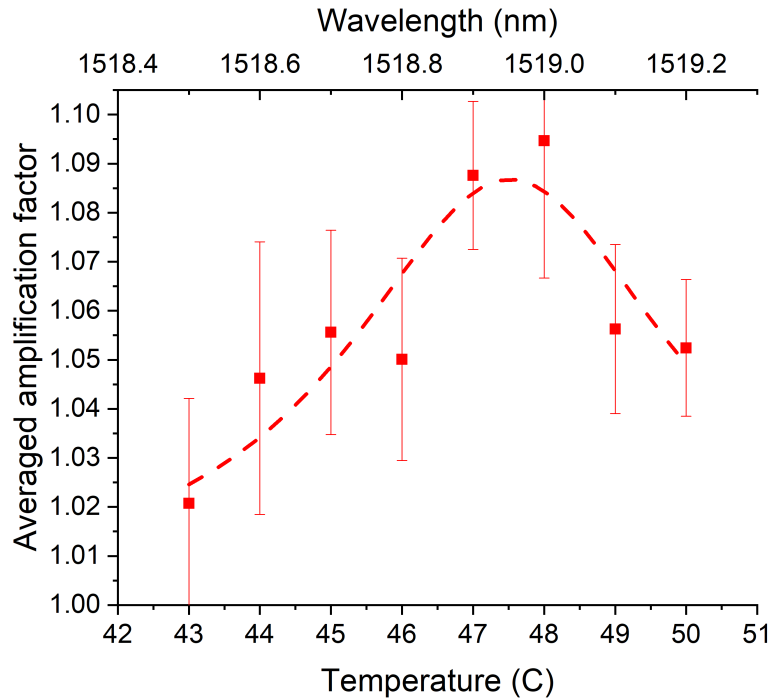


Figure 5.6: Average amplification factor of the diamond amplifier depending on the seed laser wavelength. Dashed curve is a Lorentzian fit with a $FWHM = 0.5 \pm 0.1\text{nm}$ with a quality of the fit $R - Squared = 0.8$.

Figure 5.6 shows the average amplification factor measurement versus seed laser temperature and its wavelength. Each of the red square points represents the ratio of

the area of the 64 amplified seed laser pulses to the same amount of averaged non amplified pulses. The maximum averaged gain was 10% obtained for about $48^{\circ}C$ ($1519nm$). The dashed line represents the best Lorentzian function fit of a Raman gain bandwidth of the amplifier [178] with the factor of $R = 0.8$. The reported Raman gain bandwidth in diamond of $2cm^{-1}$ [3] at $1.519\mu m$ is equal to $0.4nm$ and the dashed red curve, with a baseline fixed to the amplification factor of 1, has a $FWHM = 0.5 \pm 0.1nm$. As mentioned in [178] the lineshape of the Raman spectrum is a Voigt function which is a convolution of a Lorentzian and Gaussian functions, the first coming from the Raman spectrum and the latter from an instrumentation response. Fitting with the Voigt function in this experiment introduced a large error in estimating the FWHM of the Lorentzian fit most likely coming from the noise in the measurement - lack of baseline and instabilities of the Nd:YAP laser impacting the averaged amplification factor values therefore the Lorentzian fit only was chosen. To improve the fitting, the measurement of the average amplification factor should expand to the baseline although this might result in damaging the seed laser diode for temperatures larger than $50^{\circ}C$. Another significant error source is a timing jitter of the pump laser pulse and this will be described in more detail in the next Section.

5.5 The effect of jitter on the amplification factor

This section presents the effect that the Nd:YAP jitter has on the amplification of the seed laser. In this experiment, the seed as well as Nd:YAP pulses were recorded. The seed laser was recorded after the monochromator as seen in Figure 5.2 whilst the Nd:YAP pulse was picked off before reaching the diamond amplifier and so the exact value of the delay between the recorded signals is not meaningful. The oscilloscope was triggered by the seed laser pulse leading edge. The amplification in the Raman cavity lasts only as long as there is a first Stokes field oscillating and it was expected to last only about $20 - 30ns$ which was much shorter than the seed laser pulse duration of $100ns$ limited by the current source. Therefore, only a part of the seed laser pulse was amplified which reduced the amplification factor. Additionally, the jitter of the Nd:YAP pulses modulated the amplification window within the seed pulse in time.

As a result, the averaged amplification factor underestimates the amplification factor during the pump pulse.

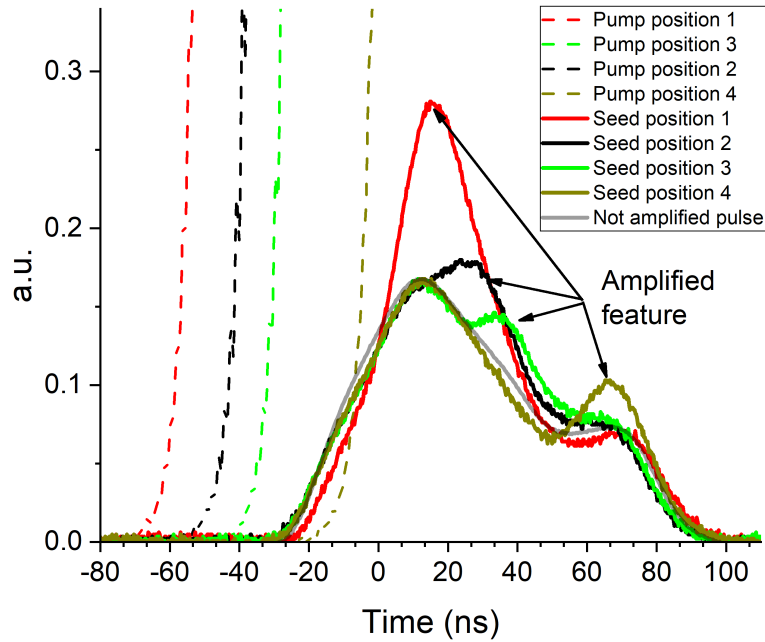


Figure 5.7: Amplification of the seed laser pulses with varying Nd:YAP pulse position.

Figure 5.7 shows seed laser pulses transmitted through the diamond amplifier. Firstly, let's consider a situation where the pump (Nd:YAP laser) is turned off and the seed is transmitted through the Raman cavity without amplification. This situation is presented with a gray curve showing the non amplified pulse coming from the seed laser, with ELD emission amplified by EDFA pre-amplifier. ELD operated at $110mA$ and $48^{\circ}C$ and $20Hz$ operation triggered by the Nd:YAP Q-switch open signal (ref. Section 3.2) and maximum operating currents for the EDFA LD1,2,3 pumps of $700mA + 700mA + 500mA$. The double peaked shape of the pulse is caused by the ELD driver.

Now the Nd:YAP laser is switched on and set to about $150\mu J$ output energy, $20Hz$ and $20ns$ pulses allowing for pumping of the first Stokes field in the diamond Raman cavity. The seed laser pulses transmitted through the diamond Raman cavity were recorded with red, black, golden and green solid curves. It can be seen, that each of these pulses have a characteristic feature which is caused by the amplification. The

amplified feature can be seen as a difference between the gray curve and the other seed laser pulses. It has to be added here, that this difference is different for each pulse because of the first Stokes intensity variations originating from the Nd:YAP instabilities and operation close to the second Stokes threshold. The first Stokes pulses were not recorded since the setup only allowed to record one output wavelength at a time. As mentioned before, the amplified feature only covers part of the seed pulse which is a result of the long seed laser pulse (or short first Stokes field in the Raman cavity). This effect could be minimized by synchronizing the pump to the seed laser. This has been tried, but the electronics available were too slow for the seed laser to turn on fast enough. The effect of the jitter can be seen as the amplified feature moving in time over the entire seed laser pulse depending on the position of the Nd:YAP laser pulse as indicated with the dashed curves. Each colour of the Nd:YAP pulse corresponds to a recorded amplified seed laser pulse e.g. the position of the red curve of the Nd:YAP laser results in the amplification of the red seed laser curve. The instantaneous amplification factor during the pump pulse for this particular pulse was the largest measured at $1.4\times$ the amplitude of the non amplified pulse.

5.6 Effect of the seed laser pulse energy on amplification

This section aims to present the influence of the seed laser energy on the amplification factor. Where the seed pulse fluence (energy over area $\frac{J}{cm^2}$) is small, the amplification factor is expected to be independent of the seed pulse fluence; for larger seed pulse fluences, by contrast, the amplification factor is expected to decrease with increasing seed pulse fluence. The transition between these two regimes is known as saturation and is characterised by the saturation fluence [40]. The aim of this section is not to quantify the saturation energy of the diamond amplifier, but to present the behaviour of the amplification factor versus seed laser fluence.

The saturation fluence of an amplifier Γ_s corresponds to the seed laser energy that is needed to decrease the amplification by $\frac{1}{e}$ [40]. The output fluence Γ of the amplifier of a length l , where the seed fluence $\Gamma_{in} \ll \Gamma_s$ can be expressed with the Equation

5.1[40]

$$\Gamma(l) = G_0\Gamma_{in} \quad (5.1)$$

where $G_0 = e^{gl}$ is the unsaturated gain of the amplifier with the gain coefficient g . The output fluence increases linearly in this regime. In the case of $\Gamma_{in} \gg \Gamma_s$, the amplification reaches saturation and the amplifier output fluence follows the Equation 5.2, where the gain is expected to drop to a $G_0 = 1$ level [40].

$$\Gamma(l) = \Gamma_{in} + gl\Gamma_s \quad (5.2)$$

Figure 5.8 presents the measured averaged amplified seed pulse area (with Nd:YAP on) versus averaged non amplified pulse area (with Nd:YAP off) both after transmission through the diamond Raman cavity and the monochromator. Pulse energy and hence fluence was not measured directly in this case due to a large amount of the spontaneous Raman scattering at second Stokes wavelength and the pulse area represents an indirect measure of the seed laser energy. The red solid curve is a linear fit to the equation 5.1 resulting in $\Gamma = 1.07 \pm 0.01\Gamma_{in}$ and there is no sign of the saturation. The length of the amplifier was fixed at $4mm$ of the diamond length and in this case the gain coefficient was $g = 0.17 \pm 0.1cm^{-1}$. This gain is in the case of seed and pump pulse duration mismatch. Assuming the amplification window lasting $50ns$ as seen on a red curve in Figure 5.7 and the amplification of $1.4\times$, by shortening the seed pulse duration from $100ns$ to $50ns$, the amplification factor should increase by 18%. To see the saturation characteristic and calculate the saturation energy of the amplifier, the spontaneous emission should be minimized and the energy of the seed laser should be increased above the saturation value.

5.7 Summary

The aim of this Chapter was to present a solid-state diamond based amplifier for the eye-safe wavelength amplification. This is to the knowledge of the author the first

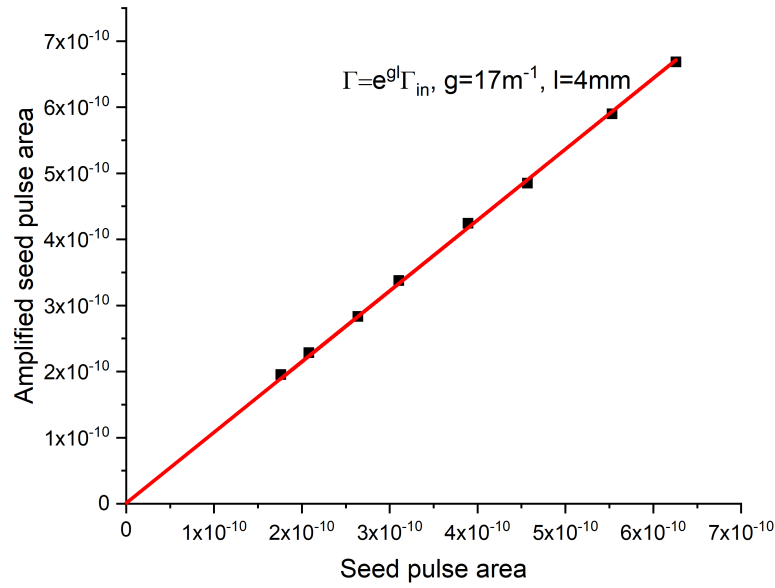


Figure 5.8: Gain estimation from an area of non amplified versus amplified seed laser pulses.

bulk solid state second Stokes Raman amplifier based on a first Stokes resonator.

The advantage of using an amplifier is that there is a greater control over the output wavelength and linewidth advantageous to Doppler LIDAR systems. Measurements included in this Chapter showed that the diamond based Raman amplifier is able to amplify wavelengths of about $1.5\mu m$ with the maximum measured instantaneous amplification factor of $1.4\times$ and 8% of averaged amplification factor (based on pulse areas) both when pumping with a Nd:YAP laser.

The challenges existing in this proof of concept system were also described: mismatch between the seed and pump lasers pulse duration and pump laser jitter; non-ideal wavelength of operation of the seed laser and significant noise in a form of parasitic second Stokes field in the Raman cavity.

5.7.1 Jitter and pulse duration

Using an adequate current source for the ELD with a possibility to decrease the pulse duration to the duration of the amplification window of $\approx 50ns$ will increase the ratio of the amplified to the not amplified seed laser pulse area from $1.4\times$ in case of half of the seed laser pulse not being amplified to $1.65\times$ when the seed laser matches the

amplification window assuming the maximum amplification factor of $1.4\times$ (ref. Section 5.5). The jitter also decreases the averaged amplification factor over many measured pulses and utilizing a source with a low jitter like a MOPA system described in Chapter 4 would solve this issue.

5.7.2 Wavelength variations

To mitigate possible Raman gain variation with the seed laser wavelength, the laser diode should be kept at a constant current and an acousto-optic modulator (AOM) would be used to curve out the pulses. This can be done by putting an in-line fiber coupled AOM in front of the EDFA pre-amplifier.

5.7.3 Parasitic second Stokes emission

As mentioned before, the spontaneous and possibly stimulated Raman scattering at a second Stokes wavelength contributed to the noise in the seed laser pulse area measurement. Temporarily this was tackled by attenuating this noise by an ND filter although this relies on a sufficiently strong seed laser signal that can still be detected despite attenuation. Possible solutions include putting a prism in order to spatially diffract the second Stokes intracavity second Stokes field and seeding the cavity at a small angle. Another option would be to introduce a quarter waveplate at a second Stokes wavelength and a polarizing beam splitter which could outcouple the second Stokes field out of the cavity. The seed laser passing through would only have its polarization changed from linear to elliptical. This could happen after passing through the diamond and the beam splitter and would not affect the amplification.

5.7.4 First Stokes wavelength

As mentioned, in order to have a sufficient signal to noise ratio, the seed laser power should be maximized. The ELD was operating at a non ideal wavelength for the EDFA amplification dictated by the second Stokes wavelength of the diamond Raman amplifier. By pushing the amplification wavelength towards the center of the EDFA amplification band at $1522 - 1523nm$, the power of the seed laser is expected to increase

Chapter 5. Diamond Raman amplifier

significantly. Pumping with a longer wavelength of about $1083nm$ would result in a second Stokes Raman wavelength of $1522nm$. The $1083nm$ wavelength can be achieved by utilizing a MOPA system presented in Chapter 4 or by using a laser with a b-cut Nd:YAP crystal [179].

Chapter 6

Discussion and conclusions

This section concludes the thesis with the main take-away points on the subject of eye-safe wavelength generation using a diamond Raman laser. The goal of this thesis was to present a high average power pulsed diamond Raman laser working at an eye-safe wavelength above $1.5\mu m$. This was done by firstly introducing a proof of concept second Stokes diamond Raman laser pumped by a custom built Q-switched Nd:YAP laser. This Raman laser was used to find optimum operating conditions for the Raman conversion, such as output coupling and laser mode sizes. The findings were then applied to a Raman laser pumped by a high average power and repetition rate fiber based MOPA system. Utilizing the fiber pump laser allowed for generation of second Stokes laser emission in the range of $13W$ of average power. Additionally, the first report is made of a diamond Raman second Stokes amplifier. The potential of this approach for the amplification of narrow linewidth eye-safe laser emission has been tested.

The following sections summarize the findings in each chapter, outline how the performance could be further enhanced, and present possible directions for future work.

6.1 External cavity Raman laser model

Chapter 2 presented a used model for predicting the output energy and conversion efficiency from the DRL using parameters such as Raman gain coefficient, laser mode

sizes, diamond crystal length and absorption. The modeling allowed one to find an optimum output coupling for the Raman laser as well as the optimum pumping spot size (sufficiently large to avoid damage to the AR coating) and the mode sizes allowing for maximum conversion efficiency. It was seen that for the maximum pumping fluence, under the AR coatings damage threshold, the optimal output coupling was between 30% and 50%.

The future development of the model should include adding an external second Stokes field simulating the seed laser in the amplifier configuration (Chapter 5). This would allow for better understanding of the saturation energy point of the amplifier. Another factor unexplored in the modelling is a transfer of the Stokes fields energy to higher order spatial modes.

As mentioned, the model allowed the Raman laser efficiency to be optimised for the diamond crystal used in the experiments. The next section explores the possibility of optimization of the diamond length and absorption. This was not possible experimentally, given the limited range of samples available, but it is a valuable information for the diamond growers.

6.2 Diamond considerations

This section is based on the model presented in Chapter 2. Using the parameters such such as the Raman gain coefficients and mode sizes obtained in experiments presented in Chapters 3 and 4, a rough boundary can be drawn of the acceptable specifications of the diamond crystals for the material growers that will allow the DRL efficiency to be maximized and at the same time keep the diamond production cost to a minimum.

Parameters used in the following simulations are the same as in Table 3.3 used to simulate the performance of the DRL in chapter 3: the diamond length was variable, the input coupler was highly reflective ($R = 0.99$) at the first and the second Stokes wavelengths and highly transmissive at the pump wavelength and the output coupler was highly reflective at the first and pump wavelengths and partially reflective ($PR = 0.3$) at the second Stokes wavelength, which was a consistent with the exper-

iments described in Chapters 3 and 4. The focused pump diameter was $d_p = 144\mu m$ and the Stokes mode diameters (taken from the ABCD matrix simulation described in more detail in Chapter 3) were $d_{first\ Stokes} = 187\mu m$, $d_{second\ Stokes} = 202\mu m$. The gain coefficients were $g_0 = 15.3\frac{cm}{GW}$ and $g_1 = 6.8\frac{cm}{GW}$. The first coefficient determines the transfer of energy between the pump and the first Stokes and the latter coefficient from the first Stokes to second Stokes field. The parameters were the same as the ones found from the experiments presented in Chapter 3. One parameter that the diamond growers might be asked to obtain is a length of the crystal.

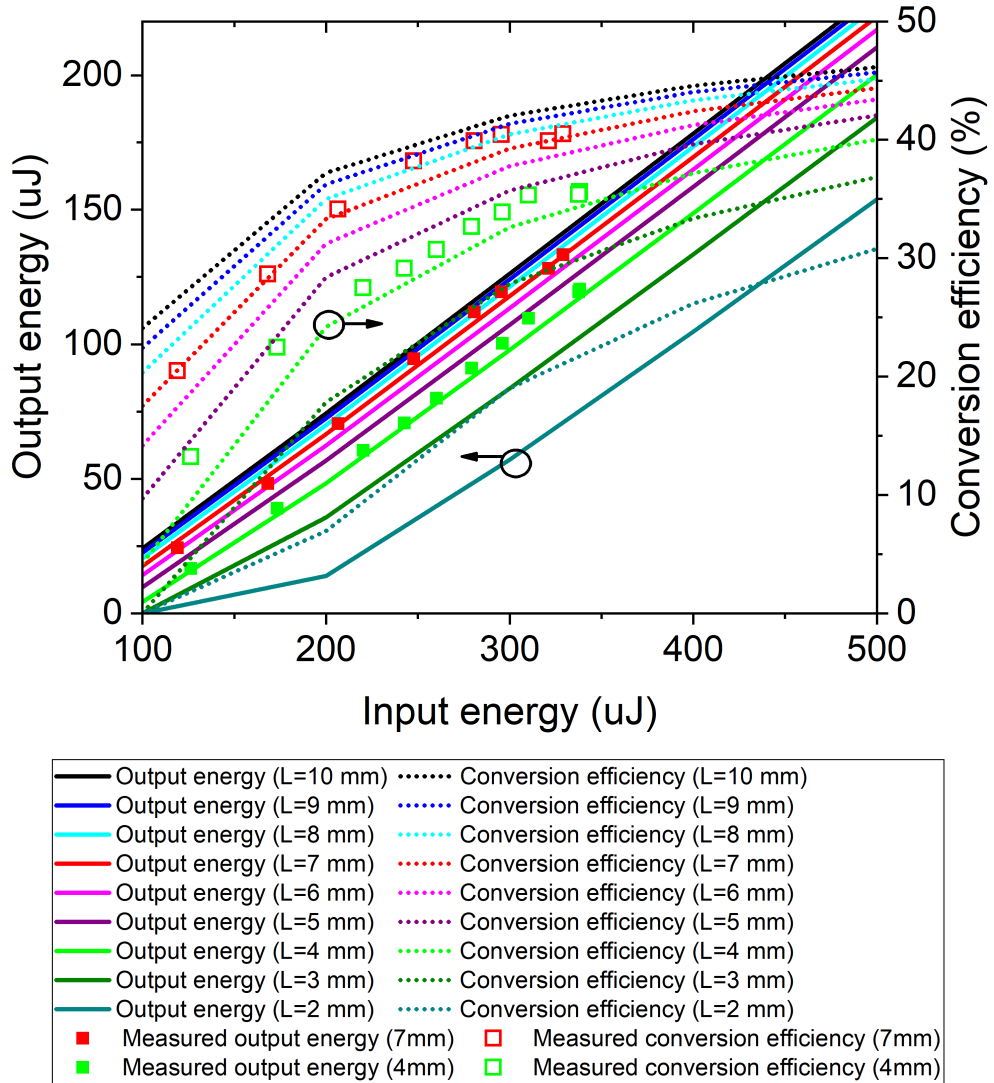


Figure 6.1: Simulation of the DRL performance versus the diamond's length L. Measured data also shown for 4mm and 7mm diamonds (squares).

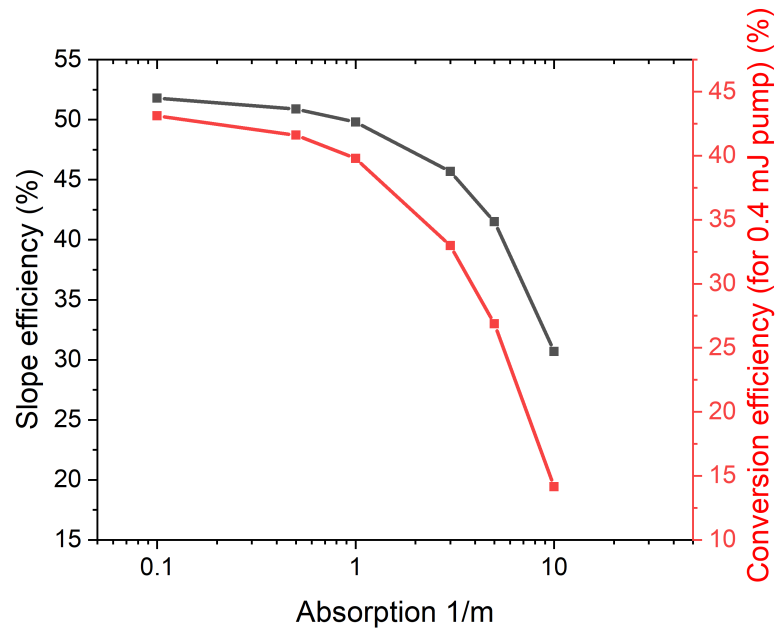


Figure 6.2: Simulation of the slope efficiency and maximum conversion efficiency of the DRL at $1.5\mu\text{m}$ at pumping energy of $400\mu\text{J}$ versus absorption coefficient.

Figure 6.1 shows the energy transfers and conversion efficiencies depending on the diamond length. Also shown are experimental measurements for available 7mm and 4mm diamonds described in detail in Chapter 3. It can be seen that the model accurately reflect the obtained experimental data. Increasing the length of the diamond from 2mm to 7mm increases the conversion efficiency by about 15% and for the lengths of $8 - 10\text{mm}$ the conversion efficiencies change by less than 2%. As shown in Equation 1.8, the Raman gain increases with diamond length and follows an arctan function. This function has an asymptote at a certain crystal length. Therefore, for the described DRL in Chapter 3, a crystal length of 8mm would be a reasonable engineering compromise on the crystal length. Further increasing the length of the crystal would not make a dramatic difference in the laser performance. At the same time, longer crystals are more expensive to grow as well as it being more difficult to control the material properties [180]. Therefore going beyond said length of 8mm would not be advised. Additionally, changing the crystal length changes its ratio to the pump confocal parameter which following work presented in [27], has an optimum value. By changing this ratio, pump focusing conditions might need to be adjusted. The $7 - 8\text{mm}$ should

be then taken as a reasonable length for a diamond length for the DRL presented in this thesis in Chapter 3.

Another parameter that can be controlled in the growth process indirectly is diamond's absorption coefficient. The latter is mainly influenced by the amount of incorporated nitrogen in the diamond growth [181, 182]. On the other hand, the growth of the single crystal diamond was shown to be 3.5 times faster when nitrogen was incorporated in the growth process [183]. Therefore it could be useful to find a middle ground between reducing the absorption coefficient by reducing the nitrogen content but at the same time maximizing the growth rate. Figure 6.2 shows simulated DRL slope efficiency and maximum conversion efficiency when pumped with $400\mu J$ of Nd:YAP laser pulses with a varying diamond's absorption from $0.1\frac{1}{m}$ to $10\frac{1}{m}$ as a parameter. The length of the diamond was chosen to be $4mm$ as this was the length of most of the samples supplied. It can be seen that the maximum conversion efficiency with a crystal with the absorption coefficient of $abs = 0.1m^{-1}$ and $abs = 1m^{-1}$ drops only about 4%. This order of magnitude increase of absorption could be important to simplify the growth process of the single crystal diamond for the applications in Raman lasers.

The supplied samples specifications indicate the absorption coefficient of about $0.5\frac{1}{m}$ at $1\mu m$ which is close to that quoted in [3]. Therefore the available material is sufficiently good for the Raman laser efficiency. This absorption coefficient is a reasonable value for the second Stokes laser at $1.5\mu m$ wavelength. The nitrogen absorption, according to the model, might be even relaxed to $1\frac{1}{m}$.

6.3 Diamond Raman laser proof of concept

Chapter 3 showed a procedure for designing the proof of concept low average power DRL together with the pump. This laser was a stepping stone in the engineering of the high average power fiber pumped diamond Raman laser presented in Chapter 4. Firstly, the requirements for the pump pulse energy were set out followed by the design and build of a Q-switched Nd:YAP solid state laser pumped with the fiber coupled laser diodes. This laser was then used to pump the diamond Raman laser for wavelength conversion from $1\mu m$ to $1.5\mu m$ wavelength.

The chapter described the design process of such a laser as well as the obtained energy transfers, pulse traces of the cascade of Stokes shifted wavelengths and basic spectral analysis. The main takeaway point from this chapter was establishing parameters of operation of the pump (energy, focus spot size, pulse duration) and DRL (mode size, output coupling). It could be seen also that the diamond was able to shift the pump wavelength of $1.08\mu m$ to an eye-safe wavelength of $1.5\mu m$. With about $330\mu J$ of pump energy at $1.079\mu m$, the maximum output energy of the DRL at this wavelength was $130\mu J$ with $20Hz$ repetition rate and about $16ns$ pulse duration for a DRL built around a $7mm$ diamond. This compares to e.g. results in [38], where $6.9mm$ diamond was used and a pump at $1.064\mu m$ and about $600\mu J$ of maximum pulse energy produced a second Stokes emission at $1.48\mu m$ of $326\mu J$. At the pump pulse energy of $330\mu J$, the output second Stokes emission was about $150\mu J$.

6.3.1 Future work

One aspect of the required future work on the Nd:YAP laser is to better optimise it for amplifier pumping work described in Chapter 5. The crystal used in this work allowed for the emission at $1079nm$ making the second Stokes emission fixed at about $1514nm$. As was discussed in Chapter 5, that the optimum working conditions of the diamond Raman amplifier is when the seed laser and the second Stokes shift of the pump laser wavelengths are the same. The output power of the seed laser in Chapter 5 at the $1514nm$ was very low, limited by the gain bandwidth of the EDFA used as a pre-amplifier. Shifting the Nd:YAP emission to a longer wavelength of $1083nm$ would result in the Raman laser second Stokes wavelength of $1522nm$. This is better matched to the gain bandwidth of the EDFA increasing the overall output power of the seed laser. Having more seed laser power would allow for a better SNR and potentially for observing the saturation behaviour of the Raman amplifier.

6.4 Diamond Raman laser pumped by a high average power fiber MOPA

The DRL developed in Chapter 3 was then pumped by a high repetition rate and average power fiber based MOPA system working at $1.083\mu m$ wavelength developed by the team at Southampton University. The ultimate goal for the high power DRL is to reach $150W$ at $1.5MHz$ repetition rate with the very good beam quality of $M^2 \approx 1$ and ns regime pulse duration. Work in this thesis presents a step towards this goal. Chapter 4 showed the best obtained result where the unpolarized emission of $1.083\mu m$ from the Yb MOPA fiber pump of $M^2 = 5.6$ operating at $150kHz$ and about $90W$ of average power with $20ns$ pulse duration was converted to the eye safe $1.52\mu m$ with an average power of $13W$ and a pulse duration of about $8ns$.

In the experiment, two pump schemes were used - polarized single mode and unpolarized multimode pumping. The first used a research-grade single-mode fibre in the final amplification stage of the pump laser system. This fibre had a strong polarisation extinction ratio, leading to a strongly linearly polarised output; however it also limited the average power to about $50W$ due to its comparatively low damage threshold. Changing the fiber to a multimode and non polarization maintaining fiber increased the damage threshold and allowed pumping with about $90W$ of maximum average power. The threshold was shown to be higher by $3\times$ in the unpolarized pumping case, but the maximum output power of the second Stokes emission increased from $9W$ (polarized pump) to $13W$ (unpolarized pump). This is despite a five fold reduction in pump beam quality in moving to the multimode fibre. This relative insensitivity to pump beam quality may prove to be an important advantage of the diamond Raman laser approach. The M^2 of the DRL output when pumped by the $M^2 = 5.6$ beam and $63W$ of average power was measured by Dr G. Demetriou to be about $M^2 = 1.2$ for $3.8W$ of average output power.

6.4.1 Future work

Increasing the repetition rate of the pump will increase the average output power and this is the route that is recommended for the future work of this project. The $150kHz$ is a high repetition rate in comparison to the sources at above $1.5\mu m$ sources presented in section 1.4 where $\approx 10W$ lasers were in $\approx 10kHz$ range - pushing the repetition rate further would increase the competitiveness of the diamond based Raman sources for scanning LIDAR applications. Assuming that increasing the repetition rate up to $1.5MHz$ would result in a linear increase of the DRL output power, up to $130W$ with a close to $M^2 = 1$ beam quality could be obtained. In addition, the conversion efficiency could potentially be further improved by the pump focused even tighter down to $\approx 50\mu m$ radius although care should be taken not to damage the bulk of the crystal or the AR coatings. Focusing tighter, especially for longer crystals also relaxes the possibility of damage to the diamond coatings as the beam size on the optical surfaces of the crystal increases. Especially for the $M^2 = 5.6$ pump this is most relevant, since its Rayleigh range is about $3mm$ and the surfaces of the $7mm$ crystal are outside of it. This advantage of reducing the possibility of damaging the AR coatings would depend on a specific laser design and is worth paying attention to.

The limitations to the Raman laser itself, that would emerge from using a higher power pump include damage to the diamond (especially graphitisation at the pump beam focus spot), damage to the AR coatings and thermal lensing. The latter depends on the open question if the diamond is able to dissipate the heat due to its high thermal conductivity faster than the time in between pump laser pulses.

6.5 Diamond Raman amplifier

Chapter 5 presented the first diamond second Stokes Raman based amplifier operating at eye-safe wavelengths above $1.5\mu m$. The amplifier configuration gives an advantage of being able to use a narrow linewidth seed to achieve narrow linewidth amplifier emission, useful for e.g. Doppler based LIDAR. The maximum achievable output energy depends on the amplifier saturation energy and the area of the laser

mode. In this case, the area is limited by the pumping spot diameter and increasing it would also increase the threshold of the Stokes field generation. Increasing of the mode size on the other hand which would increase the saturation would require a higher pump power which could become a limiting factor. The amplifier therefore does not directly present an alternative to a high power eye-safe wavelength generation but is attractive for obtaining higher power narrow linewidth output. The work presented in Chapter 5 presents only a proof of concept of a diamond Raman amplifier which confirmed that the diamond Raman amplifier does amplify the seed laser tuned to its wavelength of operation. At the Nd:YAP laser emission with $150\mu J$ energy, $20ns$ pulse duration, focused to a $72\mu m$ radius spot in a $4mm$ diamond, the instantaneous amplification of the seed laser at $1.5\mu m$ was $1.4\times$.

6.5.1 Future work

The biggest challenge that limited the amplification factor was parasitic second Stokes emission either caused by self lasing or spontaneous scattering in the Raman amplifier oscillator. The future work, already in progress, aims to increase the threshold for the parasitic emission. This could be achieved by inserting a prism inside the Raman cavity to spatially separate the first and second Stokes intracavity fields. By doing so, the threshold for the second Stokes self-lasing is expected to increase and potentially the parasitic second Stokes emission should decrease. Another option, not explored so far, is a use of polarization components inside of the Raman cavity which could introduce polarization dependent losses at a second Stokes wavelength and no losses at first Stokes. This could be done by inserting a dual wavelength waveplate and a polarizer (or a Brewster cut diamond) in the DRL cavity. The waveplate turns the polarization of the first Stokes by 180 deg per roundtrip (since the photons would pass through the waveplate twice) and maintaining its polarization throughout the cavity. In this case, the polarizer would transmit this field with minimum losses. On the other hand, the second Stokes polarization would be turned by 90 deg per roundtrip which would make this field to be reflected by the polarizer out of the cavity. Similar method was presented in a cavity dumping scheme in [184, 185] to produce pulsed laser oper-

tion. For reference, Figure 6.3 shows a schematic of such a cavity. The WP indicates a half waveplate at first Stokes wavelength and quarter waveplate at second Stokes. Then the vertical polarization of the second Stokes wavelength would be outcoupled of the cavity by a polarization beam splitter (PBS).

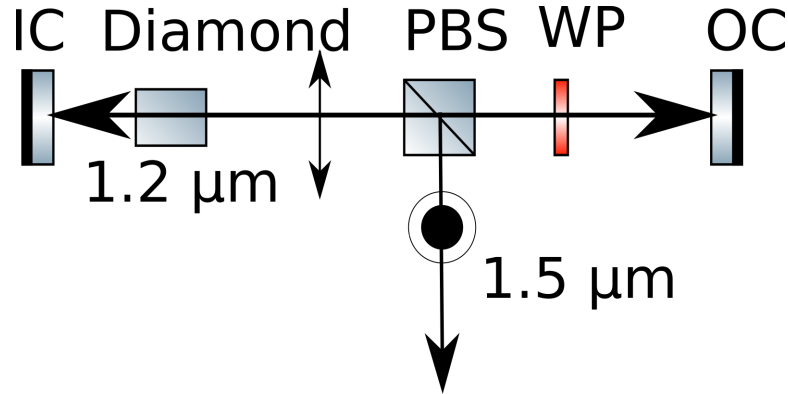


Figure 6.3: Scheme of the diamond Raman amplifier with a waveplate (WP) and a polarization beam splitter (PBS) outcoupling $1.5\mu m$ second Stokes noise out of the amplifier cavity.

Chapter 5 described also challenges imposed by the jitter of the pump and wavelength mismatch between the Raman amplifier peak of the gain bandwidth and EDFA peak wavelength of emission. The jitter comes from the Q-switching nature of the generation of the pump pulses and the most reasonable fix would be to use a fiber MOPA system (ref. Chapter 4) as a pump. The jitter in the MOPA pump source is in the order of couple ns , compared to $\approx 100ns$ in the Q-switching case, since the pulses are triggered electronically. The wavelength mismatch can be solved by shifting the pump wavelength by a couple nm . This can be achieved by using the MOPA fiber source as a pump as well as building an another Nd:YAP laser with the peak wavelength emission at $1.083nm$.

Another priority is a linewidth measurement of the seed laser (amplified narrow linewidth laser diode) to compare it to the gain bandwidth of the Raman amplifier. The linewidth of the diode by itself, operating in CW mode was measured (not presented in this thesis) to be in the range of $70MHz$ which is three orders of magnitude smaller than the diamond Raman gain bandwidth of $60GHz$ at $1.5\mu m$ which means that the wavelength stabilization of the ELD other than temperature and low noise

current source might not be needed. The ELD linewidth has to be then compared to the one after amplification in the diamond to indicate if there is any broadening effect which would in turn decrease the resolution of the speed measurement in Doppler LIDAR system.

6.6 Context of the eye-safe high power DRL

This work presented a laser operating at $1.52\mu m$, $M^2 = 1.2$ and $13W$ of average power and $86\mu J$ pulse energy with a repetition rate of $150kHz$. This is a novel demonstration of the first solid state second Stokes Raman amplifier in diamond. Compared to the pulsed eye-safe sources presented in Chapter 1 most of which are Er based fiber lasers with a kHz regime, W level average powers and $M^2 > 5$, this work is competitive in terms of the mentioned qualities. The high repetition rate source [89] reviewed in Chapter 1 had a pulse energy of $\approx pJ$ and therefore is not directly comparable. Other Er Yb:glass lasers achieve high output energy of $3mJ$ and $12W$ of average power but are limited in repetition rate to single kHz . The OPO sources also reach high mJ level output pulse energies and a very good $M^2 \approx 1$ beam quality but also are limited to a W level average powers at very low Hz repetition rate levels.

The limitations of the DRL are a combination of the pumping technology and availability of the high quality optical grade diamond material. The limitations of the pump laser can be somewhat avoided by relaxing its requirements in terms of polarization and beam quality. By using multimode, polarization non-maintaining fibers, laser operates further away from the damage threshold allowing for scaling of the output average power. The availability of the diamond is another issue since the DRL technology is not a popular one and the assessment of the market for such is another field to be explored.

The presented amplification of the eye-safe wavelengths in the second Stokes diamond Raman amplifier is a very young technology and comparing it to mature EDFA amplifiers should be done with care. Measurements of linewidth broadening of the seed laser in the diamond Raman amplifier and its saturation energy will give more information on the context of this work and how it compares with its competitors.

Bibliography

- [1] C. J. Wort and R. S. Balmer, “Diamond as an electronic material,” *Materials today*, vol. 11, no. 1-2, pp. 22–28, 2008.
- [2] S. Coe and R. Sussmann, “Optical, thermal and mechanical properties of cvd diamond,” *Diamond and Related Materials*, vol. 9, no. 9-10, pp. 1726–1729, 2000.
- [3] R. P. Mildren, *Intrinsic Optical Properties of Diamond*, ch. 1, pp. 1–34. John Wiley & Sons, Ltd, 2013.
- [4] I. Friel, S. L. Geoghegan, D. J. Twitchen, and G. A. Scarsbrook, “Development of high quality single crystal diamond for novel laser applications,” in *Optics and Photonics for Counterterrorism and Crime Fighting VI and Optical Materials in Defence Systems Technology VII*, vol. 7838, p. 783819, International Society for Optics and Photonics, 2010.
- [5] I. Friel, S. L. Geoghegan, D. J. Twitchen, and J. M. Dodson, “Cvd single crystal diamond material,” Apr. 28 2015. US Patent 9,017,633.
- [6] K. E. Spear and J. P. Dismukes, *Synthetic diamond: emerging CVD science and technology*, vol. 25. John Wiley & Sons, 1994.
- [7] S.-T. Lee, Z. Lin, and X. Jiang, “Cvd diamond films: nucleation and growth,” *Materials Science and Engineering: R: Reports*, vol. 25, no. 4, pp. 123–154, 1999.
- [8] V. Savitsky. Institute of Photonics, Strathclyde, personal communication.
- [9] D. Schlipf, D. J. Schlipf, and M. Kühn, “Nonlinear model predictive control of wind turbines using lidar,” *Wind energy*, vol. 16, no. 7, pp. 1107–1129, 2013.

Bibliography

- [10] D. A. Smith and M. Harris, “Wind turbine control having a lidar wind speed measurement apparatus,” Oct. 16 2007. US Patent 7,281,891.
- [11] D. A. Smith, M. Harris, A. S. Coffey, T. Mikkelsen, H. E. Jørgensen, J. Mann, and R. Danielian, “Wind lidar evaluation at the danish wind test site in høvsøre,” *Wind Energy: An International Journal for Progress and Applications in Wind Power Conversion Technology*, vol. 9, no. 1-2, pp. 87–93, 2006.
- [12] J. Lovell, D. L. Jupp, D. Culvenor, and N. Coops, “Using airborne and ground-based ranging lidar to measure canopy structure in australian forests,” *Canadian Journal of Remote Sensing*, vol. 29, no. 5, pp. 607–622, 2003.
- [13] J. Larson and M. Trivedi, “Lidar based off-road negative obstacle detection and analysis,” in *2011 14th International IEEE Conference on Intelligent Transportation Systems (ITSC)*, pp. 192–197, IEEE, 2011.
- [14] H. M. Tulldahl and H. Larsson, “Lidar on small uav for 3d mapping,” in *Electro-Optical Remote Sensing, Photonic Technologies, and Applications VIII; and Military Applications in Hyperspectral Imaging and High Spatial Resolution Sensing II*, vol. 9250, p. 925009, International Society for Optics and Photonics, 2014.
- [15] P. Chazette, J. Totems, L. Hespel, and J.-S. Bailly, “5 - principle and physics of the lidar measurement,” in *Optical Remote Sensing of Land Surface* (N. Baghdadi and M. Zribi, eds.), pp. 201 – 247, Elsevier, 2016.
- [16] “Safety of laser products - part 1: Equipment classification, requirements and user’s guide,” *International Electrotechnical Commission*, vol. 6000, Aug. 2001.
- [17] “American national standard for safe use of lasers,” *American National Standard*, Mar. 2007.
- [18] S. Karp and L. B. Stotts, *Light detection and ranging*. Cambridge University Press, 2012.
- [19] C. Weitkamp and H. Walther, *Lidar: Range-Resolved Optical Remote Sensing of the Atmosphere*. Springer Series in Optical Sciences, Springer, 2005.

Bibliography

- [20] E. P. Baltsavias, “Airborne laser scanning: basic relations and formulas,” *ISPRS Journal of photogrammetry and remote sensing*, vol. 54, no. 2-3, pp. 199–214, 1999.
- [21] X. Li, B. Yang, X. Xie, D. Li, and L. Xu, “Influence of waveform characteristics on lidar ranging accuracy and precision,” *Sensors*, vol. 18, no. 4, p. 1156, 2018.
- [22] M. Chanin, A. Garnier, A. Hauchecorne, and J. Porteneuve, “A doppler lidar for measuring winds in the middle atmosphere,” *Geophysical research letters*, vol. 16, no. 11, pp. 1273–1276, 1989.
- [23] C. J. Grund, R. M. Banta, J. L. George, J. N. Howell, M. J. Post, R. A. Richter, and A. M. Weickmann, “High-resolution doppler lidar for boundary layer and cloud research,” *Journal of Atmospheric and Oceanic Technology*, vol. 18, no. 3, pp. 376–393, 2001.
- [24] L. D. Liebman, S. W. Flockencier, E. M. Flowers, and D. A. Larson, “Single detector receiver for multi-beam lidar systems,” May 20 2008. US Patent 7,375,804.
- [25] H. V. Duong, M. A. Lefsky, T. Ramond, and C. Weimer, “The electronically steerable flash lidar: A full waveform scanning system for topographic and ecosystem structure applications,” *IEEE Transactions on Geoscience and Remote Sensing*, vol. 50, no. 11, pp. 4809–4820, 2012.
- [26] J. Dakin and R. Brown, *Handbook of Optoelectronics (Two-Volume Set)*. Handbook of Optoelectronics, Taylor & Francis, 2010.
- [27] G. Boyd, W. Johnston, and I. Kaminow, “Optimization of the stimulated Raman scattering threshold,” *IEEE Journal of Quantum Electronics*, vol. 5, no. 4, pp. 203–206, 1969.
- [28] Z. Bai, R. J. Williams, H. Jasbeer, S. Sarang, O. Kitzler, A. McKay, and R. P. Mildren, “Large brightness enhancement for quasi-continuous beams by diamond Raman laser conversion,” *Opt. Lett.*, vol. 43, pp. 563–566, Feb 2018.

Bibliography

- [29] Z. Bai, R. J. Williams, O. Kitzler, S. Sarang, D. J. Spence, and R. P. Mildren, “302 w quasi-continuous cascaded diamond Raman laser at 1.5 microns with large brightness enhancement,” *Opt. Express*, vol. 26, pp. 19797–19803, Aug 2018.
- [30] N. Hodgson and H. Weber, *Laser Resonators and Beam Propagation: Fundamentals, Advanced Concepts, Applications*, vol. 108. Springer, 2005.
- [31] A. E. Siegman, “How to (maybe) measure laser beam quality,” in *Diode Pumped Solid State Lasers: Applications and Issues*, p. MQ1, Optical Society of America, 1998.
- [32] A. E. Siegman, “Defining, measuring, and optimizing laser beam quality,” in *Laser Resonators and Coherent Optics: Modeling, Technology, and Applications*, vol. 1868, pp. 2–12, International Society for Optics and Photonics, 1993.
- [33] T. J. Van Den Berg and H. Spekreijse, “Near infrared light absorption in the human eye media,” *Vision research*, vol. 37, no. 2, pp. 249–253, 1997.
- [34] Seminar, “Photonic frontiers: Eye-safe lasers - retina-safe wavelengths benefit open-air applications,” *Laser Focus World*, 2008.
- [35] D. Y. Shen, J. K. Sahu, and W. A. Clarkson, “Highly efficient er,yb-doped fiber laser with 188w free-running and >100w tunable output power,” *Opt. Express*, vol. 13, pp. 4916–4921, Jun 2005.
- [36] H. Lin, Y. Feng, Y. Feng, P. Barua, J. K. Sahu, and J. Nilsson, “656w er-doped, yb-free large-core fiber laser,” *Opt. Lett.*, vol. 43, pp. 3080–3083, Jul 2018.
- [37] H. Huang, J. He, X. Dong, C. Zuo, B. Zhang, G. Qiu, and Z. Liu, “High-repetition-rate eye-safe intracavity kta opo driven by a diode-end-pumped q-switched nd: Yvo 4 laser,” *Applied Physics B*, vol. 90, no. 1, p. 43, 2008.
- [38] A. Sabella, J. A. Piper, and R. P., “Efficient conversion of a 1.064 μm nd:yag laser to the eye-safe region using a diamond Raman laser,” *Opt. Express*, vol. 19, pp. 23554–23560, Nov 2011.

Bibliography

- [39] R. W. Boyd, *Nonlinear optics*. Elsevier, 2003.
- [40] O. Svelto, *Principles of Lasers*. Springer US, 2010.
- [41] T. Fan, “Heat generation in Nd: YAG and Yb: YAG,” *IEEE Journal of Quantum Electronics*, vol. 29, no. 6, pp. 1457–1459, 1993.
- [42] A. Dement’Ev, A. Jovaiša, E. Stupak, and R. Kačianauskas, “Thermal stresses and end-bulging in cylindrical laser rods under longitudinal diode laser pumping,” *Journal of Thermal Stresses*, vol. 37, no. 1, pp. 73–92, 2014.
- [43] B. Bendow and P. D. Gianino, “Thermal lensing of laser beams in optically transmitting materials,” *Applied physics*, vol. 2, no. 1, pp. 1–10, 1973.
- [44] W. Koechner, “Thermal lensing in a nd: Yag laser rod,” *Applied optics*, vol. 9, no. 11, pp. 2548–2553, 1970.
- [45] R. J. Williams, J. Nold, M. Strecker, O. Kitzler, A. McKay, T. Schreiber, and R. P. Mildren, “Efficient Raman frequency conversion of high-power fiber lasers in diamond,” *Laser & Photonics Reviews*, vol. 9, no. 4, pp. 405–411, 2015.
- [46] S. C. Tidwell, J. F. Seamans, M. S. Bowers, and A. K. Cousins, “Scaling cw diode-end-pumped nd: Yag lasers to high average powers,” *IEEE Journal of Quantum Electronics*, vol. 28, no. 4, pp. 997–1009, 1992.
- [47] S. Chénais, F. Druon, S. Forget, F. Balembois, and P. Georges, “On thermal effects in solid-state lasers: The case of ytterbium-doped materials,” *Progress in quantum electronics*, vol. 30, no. 4, pp. 89–153, 2006.
- [48] S. Li, Y. Li, S. Zhao, G. Li, X. Wang, K. Yang, D. Li, and T. Li, “Thermal effect investigation and passively q-switched laser performance of composite nd: Yvo4 crystals,” *Optics & Laser Technology*, vol. 68, pp. 146–150, 2015.
- [49] A. Inyushkin, A. Taldenkov, V. Ralchenko, A. Bolshakov, A. Koliadin, and A. Katrusha, “Thermal conductivity of high purity synthetic single crystal diamonds,” *Physical Review B*, vol. 97, no. 14, p. 144305, 2018.

Bibliography

- [50] J. W. Dawson, M. J. Messerly, R. J. Beach, M. Y. Shverdin, E. A. Stappaerts, A. K. Sridharan, P. H. Pax, J. E. Heebner, C. W. Siders, and C. Barty, “Analysis of the scalability of diffraction-limited fiber lasers and amplifiers to high average power,” *Optics express*, vol. 16, no. 17, pp. 13240–13266, 2008.
- [51] B. Denker and E. Shklovsky, *Handbook of solid-state lasers: materials, systems and applications*. Elsevier, 2013.
- [52] A. Scott and K. Ridley, “A review of brillouin-enhanced four-wave mixing,” *IEEE Journal of Quantum Electronics*, vol. 25, no. 3, pp. 438–459, 1989.
- [53] X. Feng, H.-y. Tam, and P. Wai, “Stable and uniform multiwavelength erbium-doped fiber laser using nonlinear polarization rotation,” *Optics express*, vol. 14, no. 18, pp. 8205–8210, 2006.
- [54] S. Mauger, L. Bergé, and S. Skupin, “Self-focusing versus stimulated brillouin scattering of laser pulses in fused silica,” *New Journal of Physics*, vol. 12, no. 10, p. 103049, 2010.
- [55] J. Goss, P. Briddon, M. Rayson, S. Sque, and R. Jones, “Vacancy-impurity complexes and limitations for implantation doping of diamond,” *Physical Review B*, vol. 72, no. 3, p. 035214, 2005.
- [56] R. Kalish, “Doping of diamond,” *Carbon*, vol. 37, no. 5, pp. 781–785, 1999.
- [57] R. J. Williams, O. Kitzler, Z. Bai, S. Sarang, H. Jasbeer, A. McKay, S. Antipov, A. Sabella, O. Lux, D. J. Spence, and R. P. Mildren, “High power diamond Raman lasers,” *IEEE Journal of Selected Topics in Quantum Electronics*, vol. 24, pp. 1–14, Sep. 2018.
- [58] C. V. Raman and K. S. Krishnan, “A new type of secondary radiation,” *Nature*, vol. 121, no. 3048, p. 501, 1928.
- [59] Y.-R. Shen, “The principles of nonlinear optics,” *New York, Wiley-Interscience, 1984, 575 p.*, 1984.

Bibliography

- [60] G. Landsberg and L. Mandelzhtam, “A new phenomenon of light scattering, zh,” *Rus. Fiz. Khim. Obshch*, vol. 60, p. 335, 1928.
- [61] A. McKay, O. Kitzler, and R. P. Mildren, “Simultaneous brightness enhancement and wavelength conversion to the eye-safe region in a high-power diamond Raman laser,” *Laser & Photonics Reviews*, vol. 8, no. 3, pp. L37–L41, 2014.
- [62] R. Chang, R. Lehmberg, M. Duignan, and N. Djeu, “Raman beam cleanup of a severely aberrated pump laser,” *IEEE journal of quantum electronics*, vol. 21, no. 5, pp. 477–487, 1985.
- [63] T. Basiev, A. Sobol, P. Zverev, L. Ivleva, V. Osiko, and R. Powell, “Raman spectroscopy of crystals for stimulated Raman scattering,” *Optical materials*, vol. 11, no. 4, pp. 307–314, 1999.
- [64] T. Basiev, A. Sobol, Y. K. Voronko, and P. Zverev, “Spontaneous Raman spectroscopy of tungstate and molybdate crystals for Raman lasers,” *Optical Materials*, vol. 15, no. 3, pp. 205–216, 2000.
- [65] S. Ding, X. Zhang, Q. Wang, F. Su, S. Li, S. Fan, S. Zhang, J. Chang, S. Wang, and Y. Liu, “Theoretical models for the extracavity Raman laser with crystalline Raman medium,” *Applied Physics B*, vol. 85, no. 1, pp. 89–95, 2006.
- [66] R. Paschotta, J. Nilsson, A. C. Tropper, and D. C. Hanna, “Ytterbium-doped fiber amplifiers,” *IEEE Journal of Quantum Electronics*, vol. 33, pp. 1049–1056, July 1997.
- [67] A. Penzkofer, A. Laubereau, and W. Kaiser, “High intensity Raman interactions,” *Progress in Quantum Electronics*, vol. 6, no. 2, pp. 55–140, 1979.
- [68] H. M. Pask, “The design and operation of solid-state Raman lasers,” *Progress in Quantum Electronics*, vol. 27, no. 1, pp. 3–56, 2003.
- [69] D. J. Spence, “Spectral effects of stimulated Raman scattering in crystals,” *Progress in Quantum Electronics*, vol. 51, pp. 1–45, 2017.

Bibliography

- [70] R. Mildren, *Intrinsic Optical Properties of Diamond*, pp. 1–34. Germany: Wiley-VCH, Wiley, 3 2013.
- [71] K. Lee, B. J. Sussman, J. Nunn, V. Lorenz, K. Reim, D. Jaksch, I. Walmsley, P. Spizzirri, and S. Praver, “Comparing phonon dephasing lifetimes in diamond using transient coherent ultrafast phonon spectroscopy,” *Diamond and Related Materials*, vol. 19, no. 10, pp. 1289–1295, 2010.
- [72] M. S. Liu, L. A. Bursill, S. Praver, and R. Beserman, “Temperature dependence of the first-order Raman phonon line of diamond,” *Physical Review B*, vol. 61, no. 5, p. 3391, 2000.
- [73] A. McQuillan, W. Clements, and B. Stoicheff, “Stimulated Raman emission in diamond: Spectrum, gain, and angular distribution of intensity,” *Physical Review A*, vol. 1, no. 3, p. 628, 1970.
- [74] A. Z. Grasiuk and I. G. Zubarev, “High-power tunable ir Raman lasers,” *Applied physics*, vol. 17, pp. 211–232, Nov 1978.
- [75] V. Savitski, S. Reilly, and A. Kemp, “Steady-state Raman gain in diamond as a function of pump wavelength,” *IEEE Journal of Quantum Electronics*, vol. 49, pp. 218–223, 2 2013.
- [76] H. A. Szymanski, *Raman spectroscopy: theory and practice*. Springer Science & Business Media, 2012.
- [77] G. M. Bonner, J. Lin, A. J. Kemp, J. Wang, H. Zhang, D. J. Spence, and H. M. Pask, “Spectral broadening in continuous-wave intracavity Raman lasers,” *Optics express*, vol. 22, no. 7, pp. 7492–7502, 2014.
- [78] G. Bonner. Fraunhofer CAP, personal communication.
- [79] A. McKay, A. Sabella, and R. P. Mildren, “Polarization conversion in cubic Raman crystals,” *Scientific reports*, vol. 7, p. 41702, 2017.

Bibliography

- [80] C. Kranert, C. Sturm, R. Schmidt-Grund, and M. Grundmann, “Raman tensor formalism for optically anisotropic crystals,” *Physical review letters*, vol. 116, no. 12, p. 127401, 2016.
- [81] V. G. Savitski, I. Friel, J. E. Hastie, M. D. Dawson, D. Burns, and A. J. Kemp, “Characterization of single-crystal synthetic diamond for multi-watt continuous-wave Raman lasers,” *IEEE Journal of Quantum Electronics*, vol. 48, pp. 328–337, March 2012.
- [82] O. Kitzler, A. McKay, D. J. Spence, and R. P. Mildren, “Modelling and optimization of continuous-wave external cavity Raman lasers,” *Optics express*, vol. 23, no. 7, pp. 8590–8602, 2015.
- [83] A. Sabella, J. A. Piper, and R. P. Mildren, “1240 nm diamond Raman laser operating near the quantum limit,” *Opt. Lett.*, vol. 35, pp. 3874–3876, Dec 2010.
- [84] A. M. Zaitsev, *Optical properties of diamond: a data handbook*. Springer Science & Business Media, 2013.
- [85] E. Fujita, Y. Mashiko, S. Asaya, M. Musha, and M. Tokurakawa, “High power narrow-linewidth linearly-polarized 1610 nm er: Yb all-fiber mopa,” *Optics express*, vol. 24, no. 23, pp. 26255–26260, 2016.
- [86] C. Codemard, C. Farrell, P. Dupriez, V. Filippov, J. Sahu, and J. Nilsson, “Millijoule high-peak power narrow-linewidth sub-hundred nanosecond pulsed fibre mopa at 1.55 microns,” *Comptes Rendus Physique*, vol. 7, 01 2005.
- [87] S. Desmoulins and F. Di Teodoro, “High-gain er-doped fiber amplifier generating eye-safe mw peak-power, mj-energy pulses,” *Optics Express*, vol. 16, no. 4, pp. 2431–2437, 2008.
- [88] B. Zhang, X. Dong, J. He, H. Huang, K. Yang, C. Zuo, J. Xu, and S. Zhao, “High-power eye-safe intracavity kta opo driven by a diode-pumped q-switched nd: Yag laser,” *Laser Physics Letters*, vol. 5, no. 12, p. 869, 2008.

Bibliography

- [89] I. Pavlov, E. Ilbey, E. Dülgergil, A. Bayri, and F. Ö. Ilday, “High-power high-repetition-rate single-mode er-yb-doped fiber laser system,” *Optics express*, vol. 20, no. 9, pp. 9471–9475, 2012.
- [90] G. Anzueto-Sánchez, R. E. Nuñez-Gomez, A. Martínez-Rios, J. Camas-Anzueto, J. Castellon-Urbe, and M. Basurto-Pensado, “Highly stable, tapered fiber filter-assisted, multiwavelength q-switched er-doped fiber laser based on tm-ho fiber as a saturable absorber,” *IEEE Photonics Journal*, vol. 9, no. 6, pp. 1–8, 2017.
- [91] J. Swiderski, M. Maciejewska, W. Pichola, J. Kwiatkowski, A. Zajac, and M. Skorzakowski, “1550 nm,(1-5) ns,(0.2-2) mhz, kw-peak power, pulsed all-fiber mopa source,” in *2012 Symposium on Photonics and Optoelectronics*, pp. 1–3, IEEE, 2012.
- [92] T. Sakimura, K. Hirosawa, Y. Watanabe, T. Ando, S. Kameyama, K. Asaka, H. Tanaka, M. Furuta, M. Hagio, Y. Hirano, *et al.*, “1.55- μ m high-peak, high-average-power laser amplifier using an er, yb: glass planar waveguide for wind sensing coherent doppler lidar,” *Optics Express*, vol. 27, no. 17, pp. 24175–24187, 2019.
- [93] P. Blixt, J. Nilsson, T. Carlnas, and B. Jaskorzynska, “Concentration-dependent upconversion in er/sup 3+/-doped fiber amplifiers: Experiments and modeling,” *IEEE photonics technology letters*, vol. 3, no. 11, pp. 996–998, 1991.
- [94] E. Delevaque, T. Georges, M. Monerie, P. Lamouler, and J.-F. Bayon, “Modeling of pair-induced quenching in erbium-doped silicate fibers,” *IEEE Photonics Technology Letters*, vol. 5, no. 1, pp. 73–75, 1993.
- [95] G. Roy and P. Mathieu, “Comparison of Raman and degenerated optical parametric oscillators for a high-energy and high-repetition-rate eye-safe laser,” *Optical Engineering*, vol. 35, 1996.
- [96] W. Gong, T. H. Chyba, and D. A. Temple, “Eye-safe compact scanning lidar technology,” *Optics and lasers in engineering*, vol. 45, no. 8, pp. 898–906, 2007.

Bibliography

- [97] R. Dabu, C. Fenic, and A. Stratan, "Intracavity pumped nanosecond optical parametric oscillator emitting in the eye-safe range," *Applied optics*, vol. 40, no. 24, pp. 4334–4340, 2001.
- [98] W. Żendzian, J. Jabczyński, P. Wachulak, and J. Kwiatkowski, "High-repetition-rate, intracavity-pumped ktp opo at 1572 nm," *Applied Physics B*, vol. 80, no. 3, pp. 329–332, 2005.
- [99] X.-L. Dong, B.-T. Zhang, J.-L. He, H.-T. Huang, K.-J. Yang, J.-L. Xu, C.-H. Zuo, S. Zhao, G. Qiu, and Z.-K. Liu, "High-power 1.5 and 3.4 μm intracavity kta opo driven by a diode-pumped q-switched nd: Yag laser," *Optics communications*, vol. 282, no. 8, pp. 1668–1670, 2009.
- [100] Y. Chen, Y. Chen, S. Chen, and Y. Lan, "High-power efficient diode-pumped passively q-switched nd: Yvo4/ktp/cr4+: Yag eye-safe laser," *Optics communications*, vol. 234, no. 1-6, pp. 337–342, 2004.
- [101] Z.-Y. Li, H.-T. Huang, J.-L. He, B.-T. Zhang, and J.-L. Xu, "High peak power eye-safe intracavity optical parametric oscillator pumped by a diode-pumped passively q-switched nd: Ggg laser," *Laser Physics*, vol. 20, no. 6, pp. 1302–1306, 2010.
- [102] H. Zhu, G. Zhang, H. Chen, C. Huang, Y. Wei, Y. Duan, Y. Huang, H. Wang, and G. Qiu, "High-efficiency intracavity nd: Yvo 4\kta optical parametric oscillator with 3.6 w output power at 1.53 μm ," *Optics express*, vol. 17, no. 23, pp. 20669–20674, 2009.
- [103] Y. Duan, H. Zhu, G. Zhang, H. Wang, and Y. Zhang, "High-power eye-safe kta-opo driven by yvo4/nd: Yvo4 composite laser," *Optics Communications*, vol. 285, no. 16, pp. 3507–3509, 2012.
- [104] Y. e. Jeong, J. Sahu, D. Payne, and J. Nilsson, "Ytterbium-doped large-core fiber laser with 1.36 kw continuous-wave output power," *Optics express*, vol. 12, no. 25, pp. 6088–6092, 2004.

Bibliography

- [105] J. A. Alvarez-Chavez, H. L. Offerhaus, J. Nilsson, P. W. Turner, W. A. Clarkson, and D. J. Richardson, “High-energy, high-power ytterbium-doped q-switched fiber laser,” *Opt. Lett.*, vol. 25, pp. 37–39, Jan 2000.
- [106] Z. Huang, S. Pidishety, T. W. Hawkins, Y. Feng, Y. Feng, S. Zhu, L. Dong, and J. Nilsson, “Low-birefringence 120 w yb fiber amplifier producing linearly polarized pulses with 69-ghz linewidth at 1083 nm,” in *Laser Congress 2018 (ASSL)*, p. ATu1A.1, Optical Society of America, 2018.
- [107] K. K. Chen, J. H. Price, S.-u. Alam, J. R. Hayes, D. Lin, A. Malinowski, and D. J. Richardson, “Polarisation maintaining 100w yb-fiber mopa producing μ j pulses tunable in duration from 1 to 21 ps,” *Optics express*, vol. 18, no. 14, pp. 14385–14394, 2010.
- [108] S.-P. Chen, H.-W. Chen, J. Hou, and Z.-J. Liu, “100 w all fiber picosecond mopa laser,” *Optics Express*, vol. 17, no. 26, pp. 24008–24012, 2009.
- [109] “Spi lasers.” <https://www.spilasers.com/industrial-fiber-lasers/redenergy-g4/> [Accessed: 06.2019].
- [110] P. Cerný, H. Jelínková, P. G. Zverev, and T. T. Basiev, “Solid state lasers with Raman frequency conversion,” *Progress in Quantum Electronics*, vol. 28, no. 2, pp. 113–143, 2004.
- [111] J. A. Piper and H. M. Pask, “Crystalline Raman lasers,” *IEEE Journal of Selected Topics in Quantum Electronics*, vol. 13, no. 3, pp. 692–704, 2007.
- [112] J. Nishizawa and K. Suto, “Semiconductor raman laser,” *Journal of Applied Physics*, vol. 51, no. 5, pp. 2429–2431, 1980.
- [113] E. Granados, D. J. Spence, and R. P. Mildren, “Deep ultraviolet diamond Raman laser,” *Optics express*, vol. 19, no. 11, pp. 10857–10863, 2011.
- [114] A. Grabtchikov, A. Kuzmin, V. Lisinetskii, V. Orlovich, G. Ryabtsev, and A. Demidovich, “All solid-state diode-pumped Raman laser with self-frequency conversion,” *Applied Physics Letters*, vol. 75, no. 24, pp. 3742–3744, 1999.

Bibliography

- [115] R. P. Mildren, J. E. Butler, and J. R. Rabeau, “Cvd-diamond external cavity Raman laser at 573 nm,” *Optics express*, vol. 16, no. 23, pp. 18950–18955, 2008.
- [116] R. P. Mildren and A. Sabella, “Highly efficient diamond Raman laser,” *Optics letters*, vol. 34, no. 18, pp. 2811–2813, 2009.
- [117] S. Reilly, V. G. Savitski, H. Liu, E. Gu, M. D. Dawson, and A. J. Kemp, “Monolithic diamond Raman laser,” *Optics letters*, vol. 40, no. 6, pp. 930–933, 2015.
- [118] W. Lubeigt, G. M. Bonner, J. E. Hastie, M. D. Dawson, D. Burns, and A. J. Kemp, “An intra-cavity Raman laser using synthetic single-crystal diamond,” *Opt. Express*, vol. 18, pp. 16765–16770, Aug 2010.
- [119] J.-P. M. Feve, K. E. Shortoff, M. J. Bohn, and J. K. Brasseur, “High average power diamond Raman laser,” *Opt. Express*, vol. 19, pp. 913–922, Jan 2011.
- [120] M. Li, P. Li, X. Zhang, and X. Chen, “21.8 w cw second-stokes cvd-diamond Raman laser at 1516 nm,” *Applied Physics B*, vol. 124, no. 8, p. 165, 2018.
- [121] M. Heinzig, G. Palma-Vega, B. Yildiz, T. Walbaum, T. Schreiber, R. Eberhardt, and A. Tünnermann, “High power 2nd stokes diamond Raman optical frequency conversion,” in *Nonlinear Optics*, pp. NTu3A–2, Optical Society of America, 2019.
- [122] J. T. Murray, R. C. Powell, N. Peyghambarian, D. Smith, W. Austin, and R. Stolzenberger, “Generation of 1.5- μ m radiation through intracavity solid-state Raman shifting in ba (no 3) 2 nonlinear crystals,” *Optics Letters*, vol. 20, no. 9, pp. 1017–1019, 1995.
- [123] Y. Chen, “Compact efficient all-solid-state eye-safe laser with self-frequency Raman conversion in a nd: Yvo 4 crystal,” *Optics letters*, vol. 29, no. 18, pp. 2172–2174, 2004.
- [124] Y. Chang, K. Su, H. Chang, and Y. Chen, “Compact efficient q-switched eye-safe laser at 1525 nm with a double-end diffusion-bonded nd: Yvo 4 crystal as a self-Raman medium,” *Optics express*, vol. 17, no. 6, pp. 4330–4335, 2009.

Bibliography

- [125] H. Jianhong, L. Jipeng, S. Rongbing, L. Jinghui, Z. Hui, X. Canhua, S. Fei, L. Zongzhi, Z. Jian, Z. Wenrong, *et al.*, “Short pulse eye-safe laser with a stimulated Raman scattering self-conversion based on a nd: Kgw crystal,” *Optics letters*, vol. 32, no. 9, pp. 1096–1098, 2007.
- [126] V. Dashkevich and V. Orlovich, “Ring solid-state Raman laser at 1538 nm,” *Laser Physics Letters*, vol. 8, no. 9, p. 661, 2011.
- [127] V. Supradeepa and J. W. Nicholson, “Power scaling of high-efficiency 1.5 μm cascaded Raman fiber lasers,” *Optics letters*, vol. 38, no. 14, pp. 2538–2541, 2013.
- [128] Z. Bai, R. J. Williams, O. Kitzler, S. Sarang, D. J. Spence, and R. P. Mildren, “302 w quasi-continuous cascaded diamond Raman laser at 1.5 microns with large brightness enhancement,” *Optics express*, vol. 26, no. 16, pp. 19797–19803, 2018.
- [129] S. Antipov, A. Sabella, R. J. Williams, O. Kitzler, D. J. Spence, and R. P. Mildren, “1.2 kw quasi-steady-state diamond Raman laser pumped by an m²=15 beam,” *Optics letters*, vol. 44, no. 10, pp. 2506–2509, 2019.
- [130] W. Lubeigt, G. M. Bonner, J. E. Hastie, M. D. Dawson, D. Burns, and A. J. Kemp, “An intra-cavity Raman laser using synthetic single-crystal diamond,” *Optics express*, vol. 18, no. 16, pp. 16765–16770, 2010.
- [131] D. C. Parrotta, A. J. Kemp, M. D. Dawson, and J. E. Hastie, “Multiwatt, continuous-wave, tunable diamond Raman laser with intracavity frequency-doubling to the visible region,” *IEEE Journal of Selected Topics in Quantum Electronics*, vol. 19, no. 4, pp. 1400108–1400108, 2013.
- [132] R. Casula, D. Parrotta, A. Kemp, J.-P. Penttinen, T. Leinonen, M. Guina, and J. Hastie, “~ 1400-nm continuous-wave diamond Raman laser intracavity-pumped by an ingaas semiconductor disk laser,” in *7th EPS-QEOD Europhoton Conference*, 2016.
- [133] F. De Rougemont, V. Michau, R. Frey, and F. Pradère, “Pulse compression by

Bibliography

- Raman induced cavity dumping of a homogeneously pumped oscillator and amplifier,” *Optics communications*, vol. 54, no. 5, pp. 301–304, 1985.
- [134] V. G. Savitski, “Experimental analysis of emission linewidth narrowing in a pulsed kgd (wo 4) 2 Raman laser,” *Optics express*, vol. 22, no. 18, pp. 21767–21774, 2014.
- [135] R. Paschotta, J. Nilsson, A. C. Tropper, and D. C. Hanna, “Ytterbium-doped fiber amplifiers,” *IEEE Journal of quantum electronics*, vol. 33, no. 7, pp. 1049–1056, 1997.
- [136] M. Rini, I. Cristiani, and V. Degiorgio, “Numerical modeling and optimization of cascaded cw Raman fiber lasers,” *IEEE Journal of Quantum Electronics*, vol. 36, no. 10, pp. 1117–1122, 2000.
- [137] Y. Tsutsumi and M. Ohashi, “Simple technique for measuring Raman gain efficiency spectrum distribution in single-mode fiber,” in *2009 Asia Communications and Photonics conference and Exhibition (ACP)*, vol. 2009, pp. 1–6, IEEE, 2009.
- [138] T. Cohen, E. Lebiush, I. Auslender, B. D. Barmashenko, and S. Rosenwaks, “Influence of the pump-to-laser beam overlap on the performance of optically pumped cesium vapor laser,” *Opt. Express*, vol. 24, pp. 14374–14382, Jun 2016.
- [139] “ReZontator project.” <http://www.rezonator.orion-project.org/> [Accessed: 05.2019].
- [140] R. P. Mildren, A. Sabella, O. Kitzler, D. J. Spence, and A. M. McKay, “Diamond Raman laser design and performance,” *Optical Engineering of Diamond*, pp. 239–276, 2013.
- [141] P. Loiko, V. Savitski, A. Kemp, A. Pavlyuk, N. Kuleshov, and K. Yumashev, “Anisotropy of the photo-elastic effect in nd: Kgd (wo4) 2 laser crystals,” *Laser Physics Letters*, vol. 11, no. 5, p. 055002, 2014.
- [142] H. Yoshida, N. Takeuchi, H. Okada, H. Fujita, and M. Nakatsuka, “Thermal-lens-effect compensation of nd: Yag rod laser using a solid element of negative

Bibliography

- temperature coefficient of refractive index,” *Japanese journal of applied physics*, vol. 46, no. 3R, p. 1012, 2007.
- [143] V. G. Savitski, G. Demetriou, S. Reilly, H. Liu, E. Gu, M. D. Dawson, and A. J. Kemp, “Energy scaling, second stokes oscillation, and Raman gain-guiding in monolithic diamond Raman lasers,” *IEEE Journal of Quantum Electronics*, vol. 54, no. 6, pp. 1–8, 2018.
- [144] M. Weber, *Handbook of Laser Wavelengths*. Laser & Optical Science & Technology, CRC Press, 2018.
- [145] J. Sulc, H. Jelinkova, J. K. Jabczynski, W. Zendzian, J. Kwiatkowski, K. Nejezchleb, and V. Skoda, “Comparison of diode-side-pumped triangular nd: Yag and nd: Yap laser,” vol. 5707, pp. 325–335, 2005.
- [146] M. Boucher, O. Musset, J. Boquillon, and E. Georgiou, “Multiwatt cw diode end-pumped nd: Yap laser at 1.08 and 1.34 μm : influence of nd doping level,” *Optics communications*, vol. 212, no. 1-3, pp. 139–148, 2002.
- [147] S. Kück, L. Fornasiero, E. Mix, and G. Huber, “Excited state absorption and stimulated emission of nd³⁺ in crystals. part i: Y₃Al₅O₁₂, YAlO₃, and Y₂O₃,” *Applied Physics B*, vol. 67, pp. 151–156, Aug 1998.
- [148] D. C. Parrotta, A. J. Kemp, M. D. Dawson, and J. E. Hastie, “Multiwatt, continuous-wave, tunable diamond Raman laser with intracavity frequency-doubling to the visible region,” *IEEE Journal of Selected Topics in Quantum Electronics*, vol. 19, pp. 1400108–1400108, July 2013.
- [149] B. Xu, Y. Wang, Y. Cheng, Z. Lin, H. Xu, Z. Cai, and R. Moncorge, “Diode-pumped cw laser operation of a c-cut nd: Yalo 3 crystal on low-gain emission lines around 1.1 μm ,” *IEEE Photonics Journal*, vol. 7, no. 5, pp. 1–7, 2015.
- [150] “Maximizing ao diffraction efficiency application note.” <http://www.isomet.com> [Accessed: 07.2020].

Bibliography

- [151] D. B. Nathan D. Zamoski, Michael Wanke, “Cavity length dependence of mode beating in passively Q-switched Nd-solid state lasers,” vol. 8599, 2013.
- [152] W. Yu-Ye, X. De-Gang, X. Jing-Ping, W. Zhuo, W. Peng, and Y. Jian-Quan, “Numerical modelling of QCW-pumped passively Q-switched nd:YAG lasers with cr4+:YAG as saturable absorber,” *Chinese Physics Letters*, vol. 25, pp. 2880–2883, jul 2008.
- [153] “Thorlabs, pulsed sources osa measurements.” <https://www.thorlabs.com> [Accessed: 02.2019].
- [154] 2005. ISO Standard 11146: Lasers and laser-related equipment–Test methods for laser beam widths, divergence angles and beam propagation ratios.
- [155] S.-T. Wu, U. Efron, and L. D. Hess, “Birefringence measurements of liquid crystals,” *Applied optics*, vol. 23, no. 21, pp. 3911–3915, 1984.
- [156] B. Burgoyne, N. Godbout, and S. Lacroix, “Theoretical analysis of nth-order cascaded continuous-wave Raman fiber lasers. ii. optimization and design rules,” *JOSA B*, vol. 22, no. 4, pp. 772–776, 2005.
- [157] S. Reilly, V. G. Savitski, H. Liu, S. Reid, D. Gibson, H. Dhillon, S. O. Robbie, E. Gu, M. D. Dawson, A. Bennett, *et al.*, “Laser induced damage threshold of cvd-grown single crystal diamond surfaces with various surface finishes,” pp. ATu2A–6, 2015.
- [158] H. Rong, S. Xu, O. Cohen, O. Raday, M. Lee, V. Sih, and M. Paniccia, “A cascaded silicon Raman laser,” *Nature photonics*, vol. 2, no. 3, p. 170, 2008.
- [159] B. Min, T. J. Kippenberg, and K. J. Vahala, “Compact, fiber-compatible, cascaded Raman laser,” *Optics letters*, vol. 28, no. 17, pp. 1507–1509, 2003.
- [160] A. V. Harish and J. Nilsson, “Optimization of phase modulation with arbitrary waveform generators for optical spectral control and suppression of stimulated brillouin scattering,” *Optics Express*, vol. 23, no. 6, pp. 6988–6999, 2015.

Bibliography

- [161] G. P. Agrawal and N. A. Olsson, “Self-phase modulation and spectral broadening of optical pulses in semiconductor laser amplifiers,” *IEEE Journal of quantum electronics*, vol. 25, no. 11, pp. 2297–2306, 1989.
- [162] J. B. Coles, B. P.-P. Kuo, N. Alic, S. Moro, C.-S. Bres, J. M. C. Boggio, P. Andrekson, M. Karlsson, and S. Radic, “Bandwidth-efficient phase modulation techniques for stimulated brillouin scattering suppression in fiber optic parametric amplifiers,” *Opt. Express*, vol. 18, pp. 18138–18150, Aug 2010.
- [163] Y. O. Aydin, F. Maes, V. Fortin, S. T. Bah, R. Vallée, and M. Bernier, “Endcapping of high-power 3 μm fiber lasers,” *Optics express*, vol. 27, no. 15, pp. 20659–20669, 2019.
- [164] Y. Jeong, J. Sahu, R. Williams, D. Richardson, K. Furusawa, and J. Nilsson, “Ytterbium-doped large-core fibre laser with 272 w output power,” *Electronics Letters*, vol. 39, no. 13, pp. 977–978, 2003.
- [165] Q. Sun, Q. H. Mao, X. D. Chen, S. J. Feng, W. Q. Liu, and J. W. Y. Lit, “Influences of ase on the performances of q-switched ytterbium-doped fiber lasers,” *Laser Physics*, vol. 20, pp. 1438–1448, Jun 2010.
- [166] S. Roelandt, Y. Meuret, G. Craggs, G. Verschaffelt, P. Janssens, and H. Thienpont, “Standardized speckle measurement method matched to human speckle perception in laser projection systems,” *Optics express*, vol. 20, no. 8, pp. 8770–8783, 2012.
- [167] R. J. Williams, Z. Bai, S. Sarang, O. Kitzler, D. J. Spence, and R. P. Mildren, “Diamond brillouin lasers,” *arXiv preprint arXiv:1807.00240*, 2018.
- [168] R. Chiao, C. H. Townes, and B. P. Stoicheff, “Stimulated brillouin scattering and coherent generation of intense hypersonic waves,” *Physical Review Letters - PHYS REV LETT*, vol. 12, pp. 592–595, 05 1964.
- [169] C. Codemard. SPI lasers, private communication.

Bibliography

- [170] C. Alegria, Y. Jeong, C. Codemard, J. Sahu, J. A. Alvarez-Chavez, L. Fu, M. Ibsen, and J. Nilsson, “83-w single-frequency narrow-linewidth mopa using large-core erbium-ytterbium co-doped fiber,” *IEEE Photonics Technology Letters*, vol. 16, no. 8, pp. 1825–1827, 2004.
- [171] Y. Feng, L. R. Taylor, and D. B. Calia, “25 w Raman-fiber-amplifier-based 589 nm laser for laser guide star,” *Optics Express*, vol. 17, no. 21, pp. 19021–19026, 2009.
- [172] S. Grubb, T. Erdogan, V. Mizrahi, T. Strasser, W. Cheung, W. Reed, P. Lemaire, A. Miller, S. Kosinski, G. Nykolak, *et al.*, “1.3 μm cascaded Raman amplifier in germanosilicate fibers,” in *Optical Amplifiers and Their Applications*, p. PD3, Optical Society of America, 1994.
- [173] V. Raghunathan, D. Borlaug, R. R. Rice, and B. Jalali, “Demonstration of a mid-infrared silicon Raman amplifier,” *Optics Express*, vol. 15, no. 22, pp. 14355–14362, 2007.
- [174] V. G. Savitski, S. Reilly, and A. J. Kemp, “Steady-state Raman gain in diamond as a function of pump wavelength,” *IEEE Journal of Quantum Electronics*, vol. 49, no. 2, pp. 218–223, 2013.
- [175] A. Sabella, D. J. Spence, and R. P. Mildren, “Pump–probe measurements of the Raman gain coefficient in crystals using multi-longitudinal-mode beams,” *IEEE Journal of Quantum Electronics*, vol. 51, no. 12, pp. 1–8, 2015.
- [176] R. Stegeman, C. Rivero, G. Stegeman, P. Delfyett Jr, K. Richardson, L. Jankovic, and H. Kim, “Raman gain measurements in bulk glass samples,” *JOSA B*, vol. 22, no. 9, pp. 1861–1867, 2005.
- [177] J. R. Taylor, “Error analysis,” *Univ. Science Books, Sausalito, California*, 1997.
- [178] N. Surovtsev and I. Kupriyanov, “Temperature dependence of the Raman line width in diamond: Revisited,” *Journal of Raman Spectroscopy*, vol. 46, no. 1, pp. 171–176, 2015.

Bibliography

- [179] Y. Tzeng, Y. Huang, C. Tang, K. Su, W. Chen, G. Zhang, and Y. Chen, “High-power tunable single-and multi-wavelength diode-pumped nd: Yap laser in the $4f\ 3/2\ 4i\ 11/2$ transition,” *Optics express*, vol. 21, no. 22, pp. 26261–26268, 2013.
- [180] P. Hess, “The mechanical properties of various chemical vapor deposition diamond structures compared to the ideal single crystal,” *Journal of Applied Physics*, vol. 111, no. 5, p. 3, 2012.
- [181] I. Kiflawi, A. Mayer, P. Spear, J. Van Wyk, and G. Woods, “Infrared absorption by the single nitrogen and a defect centres in diamond,” *Philosophical Magazine B*, vol. 69, no. 6, pp. 1141–1147, 1994.
- [182] R. Farrer, “On the substitutional nitrogen donor in diamond,” *Solid State Communications*, vol. 7, no. 9, pp. 685–688, 1969.
- [183] Z. Yiming, F. Larsson, and K. Larsson, “Effect of cvd diamond growth by doping with nitrogen,” *Theoretical Chemistry Accounts*, vol. 133, no. 2, p. 1432, 2014.
- [184] R. J. Wayne, P. P. Chenausky, and C. J. Buczek, “Method for cavity dumping a q-switched laser,” Nov. 27 1979. US Patent 4,176,327.
- [185] G. Palmer, M. Siegel, A. Steinmann, and U. Morgner, “Microjoule pulses from a passively mode-locked yb: Ky (wo 4) 2 thin-disk oscillator with cavity dumping,” *Optics letters*, vol. 32, no. 11, pp. 1593–1595, 2007.